Physics and Simulations in response to the DOE review for a Nosecone Calorimeter (NCC) for the PHENIX Experiment

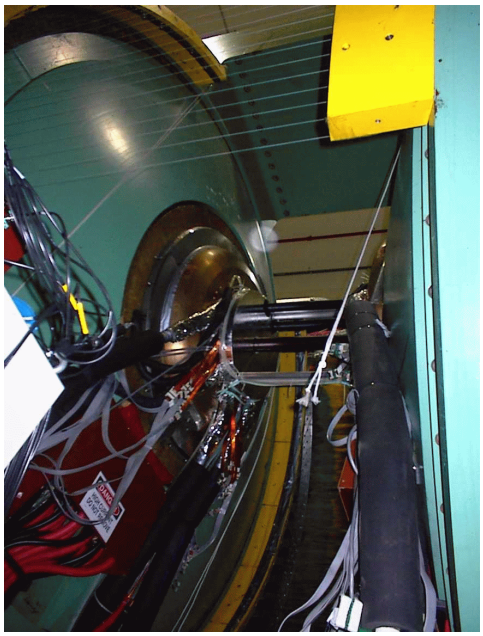

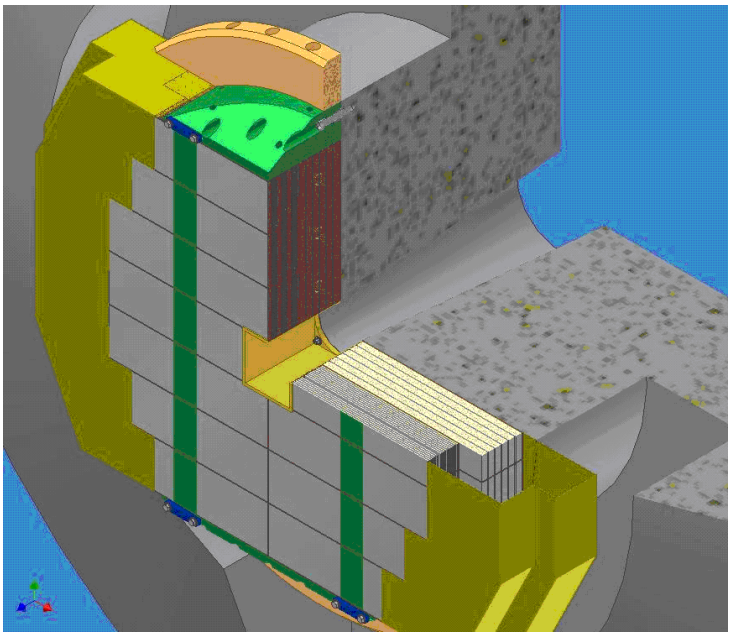

Relativistic Heavy Ion Collider
Brookhaven National Laboratory
January 26, 2008 version 1.0

PHENIX

PHENIX Nosecone Calorimeter

Participants

May, 2007

University of California, *Riverside, CA 92521, USA*
K. Barish, S. Bathe, P.S. Bourgeois, O. Chvala, T. Hester, M. Mendoza, A. Moreale, S. Rolnick, K. Sedgewick, R. Seto

Physics Dept, BARC, *, India*
Chaudrey

Instrumentation Dept., Brookhaven National Laboratory, *Upton, NY 11973-5000, USA*
Z. Li, V. Radeka, S. Rescia

Physics Dept., Brookhaven National Laboratory, *Upton, NY 11973-5000, USA*
S. Boose, M. Chiu, G. David, B. Johnson, E.P. Kistenev, D. Lynch, D. Morrison, R. Nouicer, R. Pak, R. Pisani, T. Sakaguchi, S.P. Stoll, A. Sukhanov, C. Vale, C.L. Woody

Charles University, *Ovocny trh 5, Praha 1, 116 36, Prague, Czech Republic*
Michael Finger, Miroslav Finger, M. Slunecka

Chonbuk University, *Chonju Chonbuk, 664-14, Korea*
J.B. Choi, E.J. Kim

University of Colorado, *Boulder, CO 80309, USA*
E. Kinney, J. Nagle

Columbia University and Nevis Laboratories, *Irvington, NY 10 533, USA*
C.Y. Chi

Czech Technical University, *Zikova 4, 166 36 Prague 6, Czech Republic*
M. Virius, T. Liska

Ewha Womans University, *Seoul 120-750, Korea*
I.S. Hahn, A. Kim, J. Lee, N.H. Lee, S.W. Nam, I.H. Park, J.S. Yoo

Florida State University, *Tallahassee, FL 32306, USA*
S. J. Edwards, A.D. Frawley

University of Illinois Urbana-Champaign, *Urbana, IL 61801, USA*
M. Grosse-Perdekamp, J. Koster, J.C. Peng

Institute of Physics, Academy of Sciences of Czech Republic, *Na Slovance 2, 182 21 Prague 8, Czech Republic*
P. Mikes, J. Popule, P. Ruzicka, L. Tomasek, M. Tomasek, V. Vrba

Iowa State University, *Ames, IA 50011, USA*
J.C. Hill, T. Kempel, J.L. Lajoie, F. Wei

Joint Institute for Nuclear Research- Dubna *Moscow Region, Russia*
S. Afanasiev, S. Bazylev, A. Baskakov, A. Bychkov, A. Cheremukhin, V. Elsha, N. Gorbunov, A. Isupov, N. Kotsev, A. Litvinenko, A. Malakhov, V. Peresedov, P. Rukoyatkin, V. Slepnev, I. Slepnev, N. Zamyatin, L. Zolin, E. Zubarev

University of Jyvaskyla/Helsinki Institute of Physics, *P.O.Box 35, FIN-40014, Jvyaskyla, Finland / P.O.Box 64 FIN-00014, Helsinki, Finland*
A. Kaskela, D.J. Kim, M. Oinonen, J. Rak, H. Steppänen

Korea University, *Seoul, 136-701, Korea*
B. Hong, H.H. Shim, K.S. Sim

Myongji University, *Yongin Kyonggido, 449-728, Korea*
K.S. Joo D.W. Kim, H.J. Moon

RIKEN, The Institute of Physical and Chemical Research, *Wako, Saitama 351-0198, Japan*
I. Nakagawa, A. Taketani

Skobeltsyn Institute of Nuclear Physics, Lomonosov Moscow State University, *Voro b'evy Gory, Moscow 119992, Russia*
G.A. Bogdanova, D. Karmanov, M. Merkin, V. Volkov, A. Voronin

Dept. of Physics and Astronomy, Stony Brook University, *SUNY, Stony Brook, NY 11794, USA*
A. Deshpande

Institute of Physics, University of Tsukuba, *Tsukuba, Ibaraki 305, Japan*
S. Esumi

Yonsei University, *Seoul 120-749, Korea*
J.H. Kang, Y. Kwon, S. Kim

Contents

Chapter 1

Executive Summary

This write-up is in response to the DOE scientific review of the NCC on July 9-10, 2007. In this document we address the following recommendations from the review report:

1. Each detector group should demonstrate and document scientific feasibility for two or more topics of high importance and submit to DOE for evaluation. PHENIX should submit to DOE a report documenting these studies for evaluation, prior to a technical review.

2. The NCC group should demonstrate by simulations that the non-projective geometry and shower digitization does not preclude the ability to eliminate background at the level necessary to accomplish the proposed physics goals. PHENIX should submit to DOE a report documenting these studies for evaluation, prior to a technical review.

The Nose Cone Calorimeter (NCC) is a compact tungsten silicon calorimeter covering 2π in azimuth and a pseudo-rapidity interval of $1 < |\eta| < 3$. The NCC, whose front face is located 41 cm from the nominal PHENIX interaction point, is approximately disk-shaped, 19 cm thick with a radius of 50 cm. It is composed of tungsten absorbers interleaved with silicon sensor pads and configured in three longitudinal sections, EM1, EM2 and HAD. The tungsten plates in EM1 and EM2 are 4 mm thick while the absorber in the HAD section is 12 mm think. The silicon is segmented into 15 x 15 mm^2 pads in order to match the Moliere radius of the device. In addition EM1 contains two layers of finely segmented 2-D readout silicon strip layers for shower separation located at depths of 2 X_0(radiation lengths) and 3 X_0 in the tower. We call these Photon Identifier 1 and 2 (PI1 and PI2). The thickness of EM1, EM2, HAD, as well as the position of PI1 and PI2 have been optimized since the TDR. The thicknesses of the EM1, EM2 and HAD towers are 7.5 X_0, 7.5 X_0, and 20 X_0, respectively. The NCC parameters can be found in Table 1.1.

The Nose Cone Calorimeter is designed to work as a tracking calorimeter and as such is non-projective in the same sense that a coarsely pixelated tracking chamber is non-projective: hits on each plane of the detector are associated with hits in other planes to form tracks. This is illustrated in Figure 1.1. EM1, EM2, and HAD serve as the three tracking planes of the NCC. Tracks deposit energy in multiple towers of each longitudinal plane to form clusters or "hits". Hits in each of the three planes are then associated with one another

Table 1.1: Nose Cone Calorimeter design parameters

Parameter	**Value**	
Distance from collision vertex	41 cm	
Radial coverage	50 cm	
Absorber	W (35 X_0 or 1.3 L_{abs})	
Readout	Si pads (15x15 mm^2) in calorimeter and strips (0.5x60 mm^2 in photon detector)	
Calorimeter Sampling Layers	EM1 and EM2: 7 sampling layers (4mm W + 0.5 mm Si) each HAD: 6 sampling layers (11 mm W + 0.5 mm Si)	
Photon detector (PD) Layers	2 X/Y strip layers (0.3 mm Si) downstream of second and third EM sampling layers	
Si Sensors	Pad structured	3320 (14 x 160 + 6 x 180)
	Strip structured	640 (4 x 160)
Channel count	Calorimeter	8000
	Photon detector	81920 (672 SVX4 chips)
Estimated EM energy resolution	$23\%/\sqrt{E}$ + 1% at a normal impact	
Two showers resolved at	3 cm	in calorimeter
	2 mm	in photon detector

to form tracks. The effectiveness of this design can be seen by looking at the efficiency of finding electromagnetic showers, which is rather uniform over all angles for all centralities (Figure 1.2), for shower energies between 1 and 40 GeV. After the "tracks" are found, further assembly is an iterative process of incorporating hits into the tracks to form a shower (which we continue to call "track"). Longitudinal and transverse χ^2s are associated with each track and used for identifying whether the track was an electromagnetic shower, a MIP track or a hadronic shower. In addition the two layers of strip detectors PI1 and PI2, with 50 μm pitch, are used to identify whether a track results from a single photon or two photons. If it is found to contain two photons, the ADC values in the strips are used to find their energy asymmetry. Using the total energy, energy asymmetry and opening angle (again taken from the strips) one can reconstruct the invariant mass of the two overlapping showers.

We have chosen to illustrate the capabilities of the NCC by fully simulating: 1) π^0 R_{AA} in heavy ion collisions and its implications for the measurement of direct photons and photon+jet events and 2) χ_C R_{AA} as measured by its decay into J/ψ+γ in heavy ion collisions These physics signatures are among the most critical to make and will give insight into the properties of the sQGP, in particular on the mechanisms of energy loss and deconfinement.

The simulations start from the generation of signal events and background (HIJING for Au+Au and d+Au, PYTHIA for p+p) and are run through a full GEANT Monte-Carlo

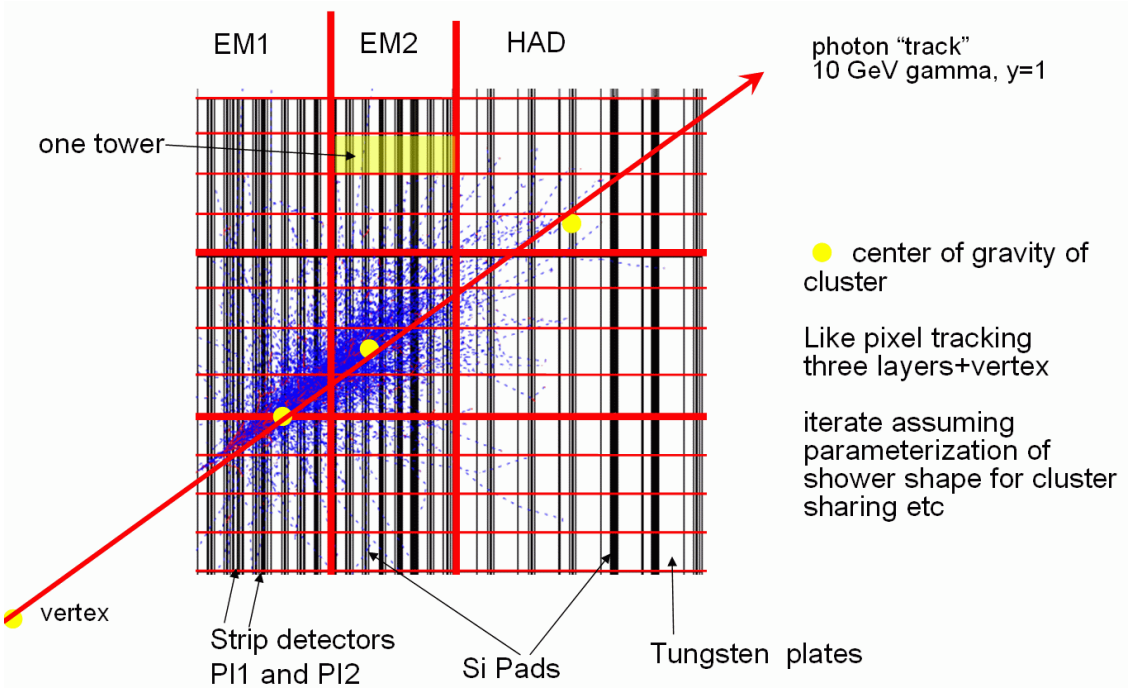

Figure 1.1: Schematic of 6 modules of the NCC. Shaded in yellow is one tower which is 1 pad in area on the face. The ADC's from the pads composing each tower are grouped together and digitized as a single unit. Illustrated is the technique used to reconstruct showers in a tracking calorimeter, thereby circumventing the necessity for a projective geometry.

(PISA) for which we have included the NCC as a new subsystem. The events are then simulated through the electronics chain, using a detector response model (consistent with the 14 bit digitization which we will be using and for which we have a working prototype) and full reconstruction taking only the data as it is simulated. Figure 1.3 shows a schematic flowchart of the steps taken. After reconstruction the data is then analyzed to yield the appropriate signals we wish to explore. We briefly outline the analysis steps to reconstruct π^0s which form the core of our R_{AA} π^0 analysis, as well as the steps for χ_C simulation and analysis.

1.1 π^0 analysis

Two techniques are used to reconstruct π^0s. For energies below about 5 GeV, the standard method of forming the invariant mass of all pairs of photons with energy greater than 0.5 GeV is used. We call these "two-track" π^0s. Cuts on the longitudinal and lateral χ^2 were imposed on each photon, as well as an energy asymmetry and an opening angle cut. The background was obtained using mixed events. In the case of Au+Au events, we limited the rapidity to $\eta < 1.5$ GeV, in order to reduce the effect of occupancy. (Fig. 1.4 shows the regions of rapidity in which various physics signatures will be accessible in the NCC.) For higher energy $\pi^0 s$ the two photons overlap, and the technique described previously using

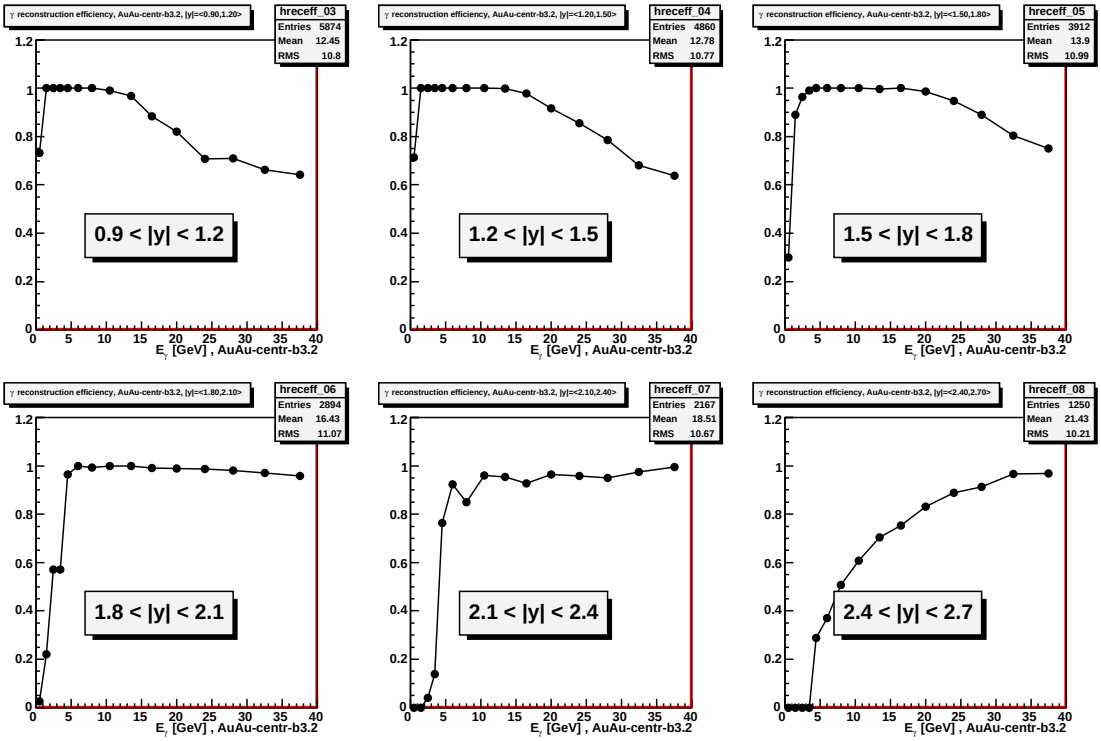

Figure 1.2: Reconstruction efficiency for showers at various energies and rapidities in central 10% Au+Au collisions. These efficiencies were found by embedding photons in background events beginning with HIJING, running though a GEANT based simulation package and reconstructing. Particles which hit the NCC at rapidites higher than 2.5 enter the detector through the beampipe hole, and are rejected by the current reconstruction software.

the strip detectors is used to form the invariant mass. An invariant mass cut was made to preferably select which came from π^0's. These were called "single-track" π^0s. There is background from photons where the invariant mass is consistent with a π^0 mass. A weight is assigned to each "single-track" π^0 which is essentially the probability that the track was a π^0. For both "single-track" and "two-track" π^0s spectra were formed and a yield calculated assuming the RHIC II luminosities and a 10 week run. R_{AA} plots then can be made in which we assume some value of R_{AA} and use the present simulation to place error bars on the plots.

1.2 χ_C analysis

The χ_C is reconstructed via is $J/\psi + \gamma$ decay mode where the J/ψ is detected through its dimuon decay mode in the muon spectrometer located just behind the NCC. For the simulation, a mixture of J/ψs and χ_Cs were thrown, where the relative composition is consistent with the known feedown of J/ψ from χ_C in p+p collisions. Background under the J/ψ peak in the dimuon invariant mass distribution was taken from the measurements in the present PHENIX data. We assumed a factor of 2.5 improvement in S/B for the J/ψ from the

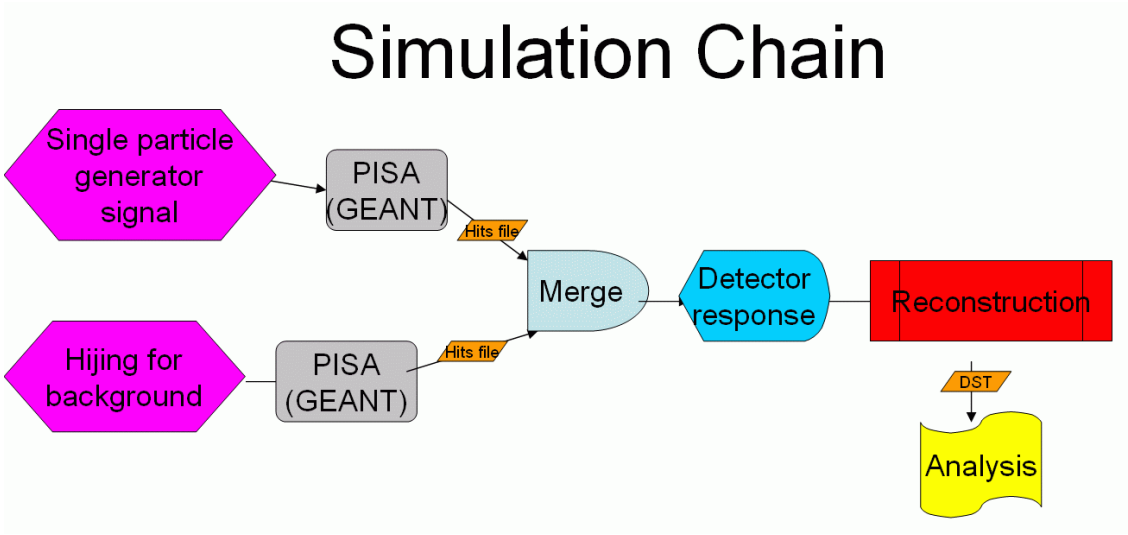

Figure 1.3: Flowchart of the steps used in these simulations.

FVTX. This arises from an improvement in mass resolution, and in the rejection of muons from hadron decay. (!!refer FVTX!!). These events were then embedded into background events, and the reconstruction packages for the muon spectrometer, the FVTX, and the NCC were run. The $J/\psi + \gamma$ invariant mass was then formed where the γ was required to have $E_\gamma > 0.5$ GeV and χ^2 longitudinal consistent with being a electromagnetic shower. As in the case of the "two-track" π^0's a mixed event technique was used to obtain the background shape. An opening angle cut was made between each of the muon tracks and the photon. Again, for central Au+Au collisions we limited the analysis to η <1.5, see fig. 1.4.

A short summary of the results follows:

- The reconstruction efficiency as a function of angle, momentum, and multiplicity is reasonably uniform - this tells us that the the design of a non-projective tracking calorimeter and shower digitization capabilities of the NCC is sufficient to detect relevant signals, and the capability to eliminate background is appropriate to accomplish the proposed physics goals.

NCC physics signatures			
	π^0 2-track	π^0 Single track	χ_C
pp	E<6 GeV 1<Y<2.5	E>6GeV 1<Y<2.5	1<Y<2.5
dAu	E<6 GeV 1<Y<2	E>6GeV 1<Y<2.5	1<Y<2.5
AuAu mid-central	E<6 GeV 1<Y<2	E>6GeV 1<Y<2.5	1<Y<2
AuAu central	E<6 GeV 1<Y<1.5	E>6GeV 1<Y<2.5	1<Y<1.5

Figure 1.4: Summary of rapidity coverage for each physics signal studied.

- The π^0 cross section and R_{AA} will be measured between transverse momenta of 1 and 20 GeV, with a precision which should allow us to discriminate between models of energy loss (fig. 3.7). In addition, direct photons can be measured with enough accuracy such that photon-jet measurements will be attainable via the use of correlations between the direct photon measured in the NCC and high momentum particles measured in other detectors such as the barrel VTX detector (figs. 3.9 and 3.10.

- The R_{AA} of the χ_C in heavy ion collisions can be sufficiently well measured so that together with the J/ψ and ψ' data one can significantly constrain models of charmonium suppression and distinguish between various models of deconfinement (or other means of dissociation) and regeneration(fig. **??**).

Chapter 2

The NCC: principles of design and operation

A remarkable result has emerged from the first several years of data taking at RHIC - the high temperature and density phase of QCD matter created in heavy ion collisions at RHIC is best described as a near perfect fluid - the strongly interacting Quark-Gluon-Plasma (sQGP). This state is characterized by a small viscosity to entropy ratio, and a high density of color charges which induce huge energy losses in partons traversing the medium. The task for the future is to understand the characteristics of the sQGP, and perhaps more importantly - to gain some insight into how and why such a medium is created. Many of the important scientific discoveries and associated publications at RHIC benefited enourmously from the contribution of the PHENIX Central Arm calorimeters, see (ADD REFERENCES), to name a few references. The coverage of the present PHENIX electromagnetic calorimeter is rather limited, covering half the azimuth and -0.35< η <0.35. Advances in the understanding of this fundamental state of matter would be facilitated by a larger coverage with electromagnetic calorimetry, both to increase the rate for low cross section phenomena, and to cover a broader range of pseudorapidity, in order to study the rapidity dependence of the medium's properties. For this reason we are proposing to construct and add the NCC to the PHENIX suite of detectors.

Our prime motivation is to provide precision measurements of direct photons, π^0s and jets over an extended range of rapidity in A+A, (p)d+A, and polarized p+p collisions. This upgrade will provide access to physics observables that are not currently accessible to PHENIX or that are now available only indirectly and with very limited accuracy.

2.1 The NCC design: a tracking calorimeter

The second of the recommendations of the review report stated:

- The NCC group should demonstrate by simulations that the non-projective geometry and shower digitization does not preclude the ability to eliminate background at the level necessary to accomplish the proposed physics goals. PHENIX should submit to DOE a report documenting these studies for evaluation, prior to a technical review.

We will answer this question in the next few sections of this document.

The NCC is a highly segmented tracking calorimeter designed to reconstruct and identify electromagnetic signals at intermediate rapidities in close proximity to production vertex. The design takes full advantage of the large body of existing data on particle showering in matter to design a total absorption detector that is able to measure the energy and direction of impinging particles and to discriminate between electromagnetic and hadronic showers. The NCC is composed of two identically structured high density fine sampling electromagnetic segments (EM1 and EM2) and one coarse hadronic (HAD) segment. EM1 also houses two layers of high resolution two-dimensional position sensitive detectors, at optimal depths of $\sim 2X_0$ (L1) and $\sim 3X_0$ (L2). The role of the position sensitive detectors PI1 and PI2 is to count photon hits, measure hit-to-hit separation and estimate the energy sharing between possible contributors to high energy tracks built of showers seen in calorimeter segments. The longitudinal structure of the calorimeter tower is sketched in Fig. 2.1.

The NCC is located 41 cm from the nominal collision point, on the poles of the PHENIX central magnet, and limited to a depth of 19 cm. It is built of tungsten plates (4 mm thick in EM and 11 mm thick in HAD segments) interleaved with silicon readout layers. The readout layers are structured into pads of $15 \times 15\,\mathrm{mm}^2$ in the calorimeter and strips of $0.5 \times\ 60\,\mathrm{mm}^2$ in the position sensitive layers. Two EM segments together are 14 L_{rad} deep; the hadronic segment adds an additional 18 L_{rad} to the total depth of the NCC.

The recently published NCC TDR presents an extensive set of performance measures based upon a standalone simulation chain implementing a free standing NCC in GEANT3. The NCC implementation has since then been integrated into the complete PHENIX GEANT simulation, which includes all material located in PHENIX, allowing for the study of all aspects of running the NCC as part of the PHENIX experiment. Extensive modifications were also made to the pattern recognition algorithms to improve energy and position resolution, efficiency and sensitivity to shower shape measurements. The new and largely improved suite of software has been used to provide answers to the questions generated as a result of the NCC Science review in July 2007.

By design, the NCC segments are structured into mechanically nonprojective towers (see Fig. 2.2).

The design of the NCC with mechanically nonprojective towers was prompted by the existing experience with the PHENIX central calorimeters. There, we have particles hitting at angles up to 20° without any noticeable effect on the calorimeter's performance. Segmenting the NCC longitudinally allows us to separate electromagnetic showers from hadronic showers. The towers in EM segments have an aspect ratio of ~ 2 (ratio of the tower depth to its lateral size measured in the diagonal direction). The mechanical aspect ratio increases by a factor of 2 in the hadronic segment. The NCC is optimized for EM showers being totally extinct by the third readout layer of the hadronic segment so that the increased aspect ratio has no effect on tracking EM particles. Constructing every segment of the decoupled towers with an aspect ratio $\times 4$ smaller than that of the central arm calorimeter maintains the detector occupancy at a level comparable to that seen in the central arm calorimeter, with much higher impact angles (to 45°). To illustrate this, Fig. 2.3 shows, for each of the three calorimeter segments, how the number of towers that contribute to a cluster depends on

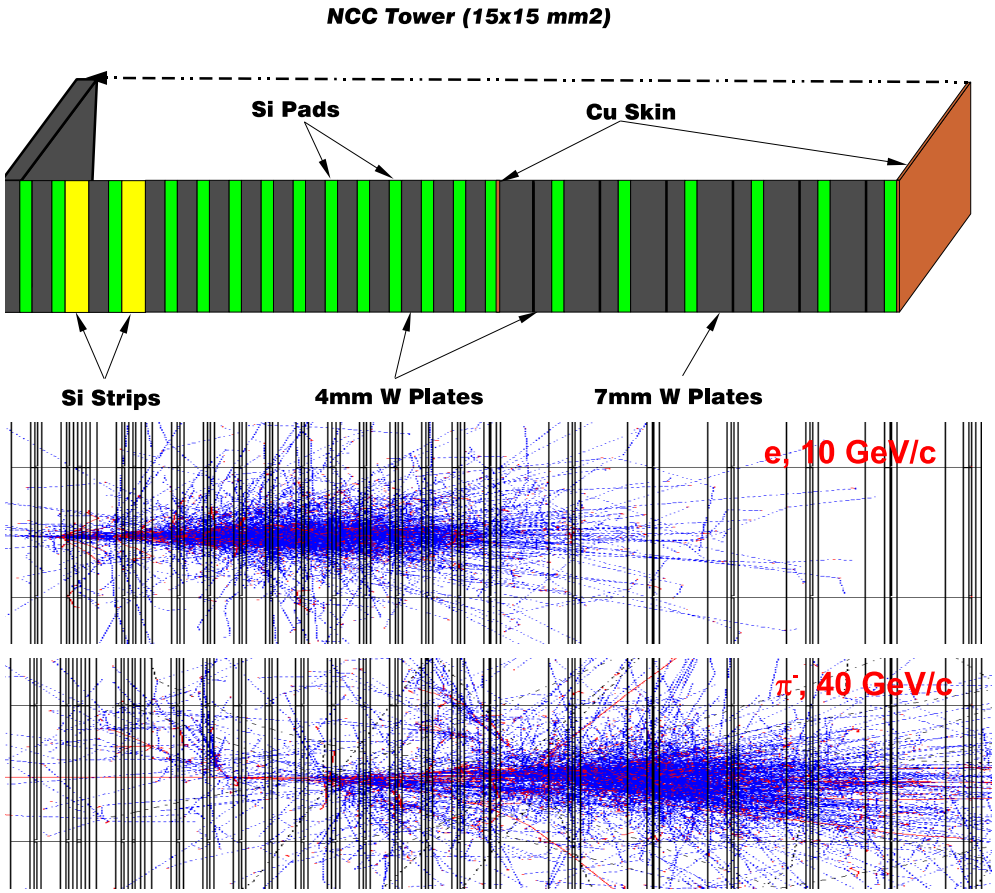

Figure 2.1: Longitudinal structure of a single calorimeter tower showing the locations of the three calorimetric segments, EM1, EM2, and HAD, and the high-resolution position sensitive layers. Shown in the bottom panel are electromagnetic and hadronic showers due to a 10 GeV/c electron and 40 GeV/c charged pion.

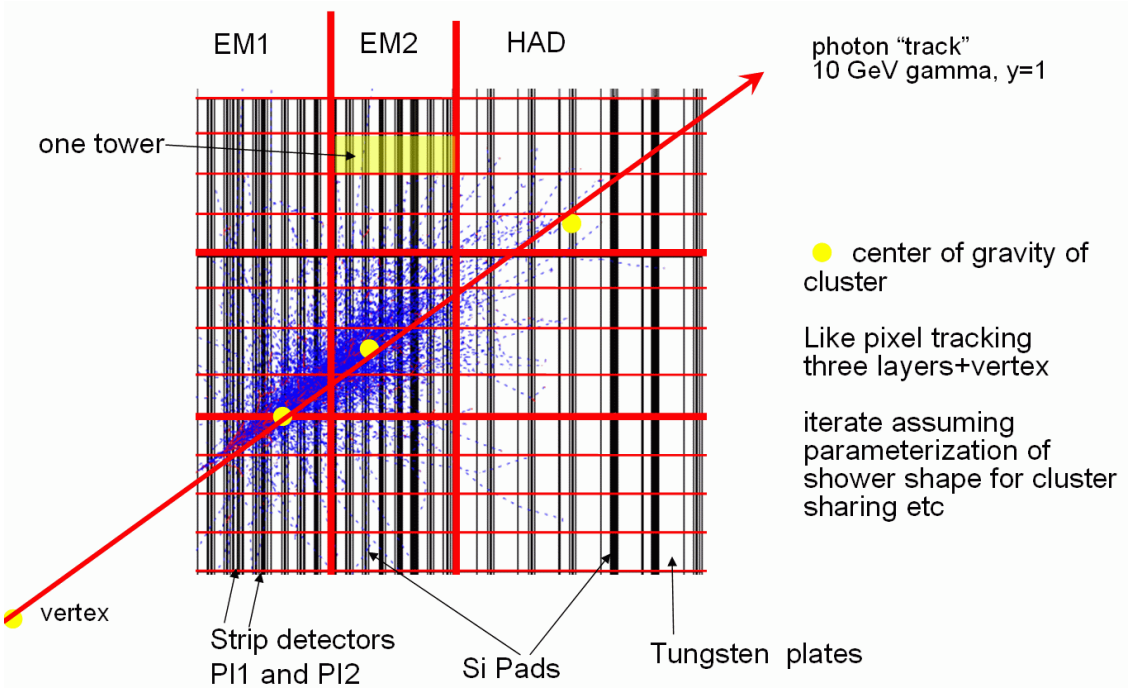

Figure 2.2: Principles of tracking measurements in the NCC.

impact angle. The tower cluster multiplicity per track rises by less than 50% between mimimum and maximum impact angles (compared to $\times 2$ increase in the central arm calorimeter). The density of particles hitting the detector decreases towards larger impact angles (smaller rapidities), which minimizes the effect of increased cluster multiplicities on the calorimeter occupancy.

2.2 Simulation

The detector has been modeled in the GEANT-3 based PISA simulation framework ("PHENIX Integrated Simulation Application") which ensured a realistic description of the rest of the PHENIX detector, including all background and albedo sources. A new beampipe and the forward vertex detector - planned to be in front of the NCC - have also been fully implemented (see Fig. 2.4). As for the NCC, all enclosures, electronics, outer and interleaved support structures were included in order to make the simulations as realistic as possible. In our χ_C studies we used the standard muon tracking software for muon reconstruction. As for reliability, it should be noted that when the central arm of PHENIX became operational, it turned out that background levels, performance of algorithms, *etc.*, which were predicted based upon PISA simulations were remarkably accurate (within 30%). Therefore, we believe the simulation results in this Chapter are also quite realistic.

Simulated single particles were used to establish energy deposit patterns as a function of momentum, rapidity and particle type; the results were used to calibrate the detector and to establish the primary particle identification cuts, which were then revisited when those single

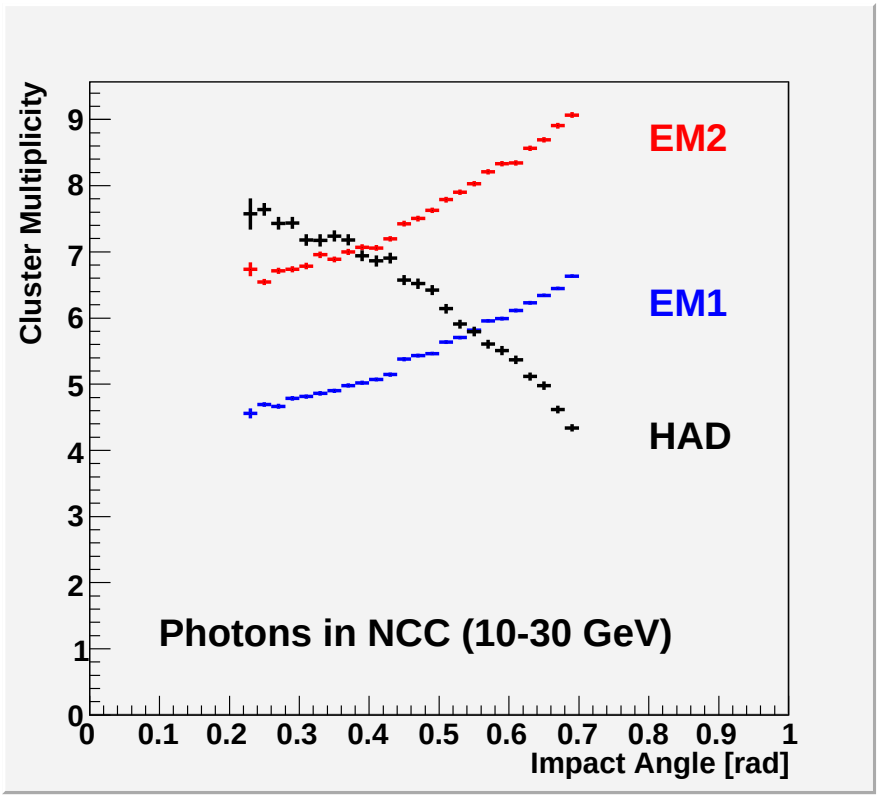

Figure 2.3: Angular dependence of the tower cluster multiplicity in three NCC segments.

particles (optimum case) were embedded into the underlying "real" events (background). The underlying events were generated with HIJING 1.37 which serves as a standard for PHENIX. Samples of 50K events were produced for the following systems and collision centralities at $\sqrt{s_{NN}}$=200GeV: p+p minimum bias, d+Au minimum bias, d+Au 0-20% (most central), Au+Au 0-10% (most central), 10-20%, 20-30%, 30-40%, 40-50%, 50-60%, 60-80%, 80-92% (most peripheral). For spin studies, 500 GeV center of mass p+p events were produced (PYTHIA) which included both the signal and the background.

After processing signal and background files though PISA, events were then subjected to the detector response chain to make a simulated raw data file. These events were then calibrated and reconstructed as mentioned above. Since the CPU time needed to directly simulate the full luminosity of a RHIC II run is prohibitive, we have simulated small data sets and then scaled up the signals to a full run, using the signal to background and efficiency factors found in the simulation chain.

Because the code being used was essentially written during the course of the preparation of this document, it is not yet fully optimized neither for speed nor for performance. We expect that with some work, we can gain large factors to better utilize CPU time and improved performance. The processing time for 250 central events is about 14 hrs. The CPU time required is proportional to the square of the multiplicity at the moment.

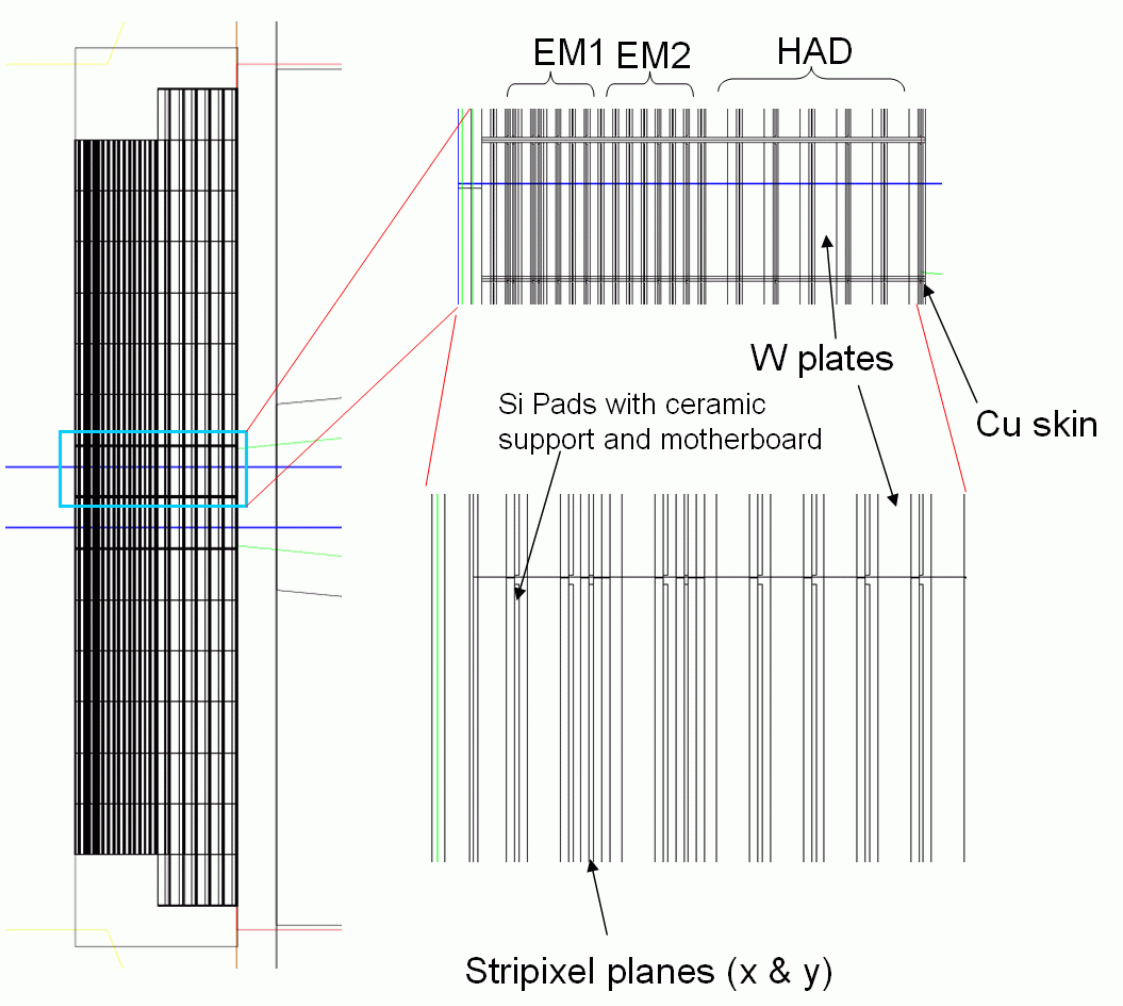

Figure 2.4: GEANT picture showing the implementation of some of the details of the NCC in the simulation.

2.3 Energy calibration

The basic readout units of the NCC are the (sub)towers (energy and time information) and the strips (energy). The energy deposited by showering particles inside individual Si sensitive elements was digitized into ADC counts, assuming 13 bits equivalent noise free ADC with 50 GeV dynamic range in every subtower. The reverse conversion (ADC counts into measured track energy) was implemented following recommendations for calibration of longitudinally segmented systems in [**?**]. Minimum ionization particle losses in individual segments were used to compute relative weights of the segments which we further corrected for the ratio of the total visible energy to the true energy of the impinging photon. This energy calibration procedure was applied directly to the energies seen in the towers and strips. Clusterization and track reconstruction were done with energies measured in units of GeV and subject to the precision loss due to digitization.

2.4 NCC occupancy

Fig. 2.3 shows that the number of hit towers per cluster (corresponding to a single photon of energy between 10 and 30 GeV) as a function of the impact angle for EM1, EM2, and HAD is less than 10. Since each NCC layer (e.g. EM1) has about 2500 channels, the majority of which at rapidities between 1 and 2, the NCC will have reasonable occupancies of (<50%) for mid-central Au+Au events.

The occupancy of the NCC in central Au+Au collisions is very high (see Fig. B.4). However, much of it is due to low energy showers and minimum ionizing particles (MIPs). After a cut of 300 MeV on the sub-tower energy, the occupancy in the $1 < \eta < 1.5$ region is less than 40%. At higher rapidities the average energy deposited is higher but a 500 MeV threshold will still allow measurements for two-track π^0s and χ_Cs up to η=2. High p_T single-track π^0s and direct photons are much less affected. Since these deposit larger energies, they will appear clearly above the background of overlapping low energy showers. We will show in this document that we can measure single track π^0s and photons to at least η =2.5. At higher pseudorapidities a special energy calibration is necessary as the showers are not fully contained in the NCC. While we believe that ultimately we will be able to make measurements up to η=3, proving it is beyond the scope of the study described in this document.

2.5 Cluster and track reconstruction

Clusters are defined as contiguous sets of towers (in a particular layer of the NCC) that *presumably* are part of a shower resulting from the same particle, and having an energy and a position assigned to them. Each calorimeter segment is treated independently, thus allowing for a nearly-independent measurement of a weighted center-of-gravity of a shower, in a segment with a typical resolution of $\sim$ 0.8 mm. A similar treatment applied to the data collected in the PI layers results in two additional space points associated with the same shower (and a resolution of $\sim$ 0.2 mm).

Regression lines through the primary vertex and five points measured inside the NCC (three pad-structured segments and two photon identifier layers) are designated as tracks. Due to the high occupancy we introduced a flexible algorithm in which lower level objects can ultimately contribute to more than one higher level object (a tower to more than one cluster, a cluster to more than one track). The final energy of the cluster is the sum of the contributions from its individual towers (shared between all clusters which each tower is a part of). Similarly, the energy of the track is equal to the sum of the calibrated energies of contributing clusters. Figure 2.6 illustrates the global track finding efficiency in the NCC (all particles impinging on the NCC are counted), which is near-perfect in p+p and peripheral Au+Au events. As for mid-central and central Au+Au events, the slope of the correlation is significantly less than one, but one should keep in mind that no energy threshold is applied here and that overwhelming part of the hits are low energy. While those low energy hits will not form individual tracks, high energy particles will still form distinct tracks. These might be contaminated by low energy particles, shifting their energy scale, but such shifts will be

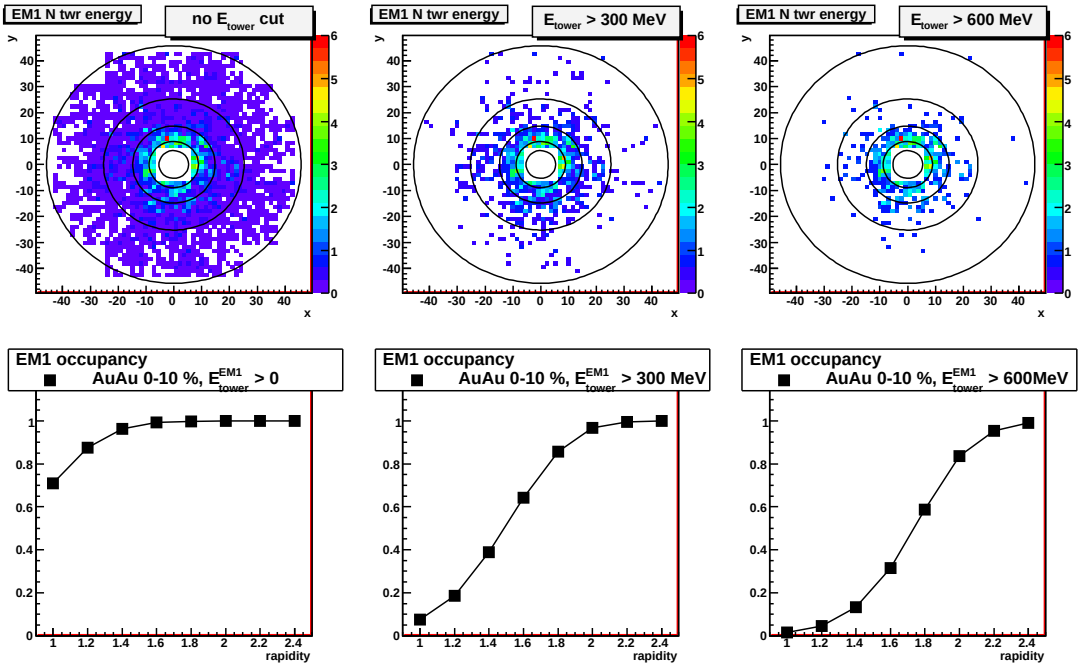

Figure 2.5: Upper row: energy [GeV] deposited in the sub-towers of the NCC EM1 section for a central (0–10 %) Au+Au event, with no threshold (left), 300 and 600 MeV thresholds (middle and right). Colors indicate the total energy deposited in each sub-tower. The energy for a MIP is about 200 MeV. The circles on the plot indicate pseudorapidity in steps of 0.5 with the outermost solid circle showing $\eta = 1$, the next dotted line indicating $\eta = 1.5$, etc. up to $\eta = 3$ for the smallest circle. The bottom plots show the occupancy as a function of pseudorapidity for no cut on tower energy (left), a 300 MeV cut on the tower energy (middle) and a 600 MeV cut (right). For $\eta < 1.5$ and a cut of 300 MeV, the occupancy is below 50.

smaller and smaller as we move up in energy.

In what follows, reconstructed tracks are used for comparing to the particles simulated by event generators and later processed through the whole PHENIX simulation chain (PISA).

2.6 Tracking performance

The details of the NCC tracking efficiency were studied using GEANT simulation data only and will be further improved when test beam data is available. Electromagnetic particles (photons, electrons and π^0s) with transverse momenta between 1 to 20 GeV were embedded into background events produced by HIJING. Each event was reconstructed and the original embedded track was found.

Fig. 2.7 a) shows the efficiency for finding and identifying electromagnetic showers in p+p collisions. The drop off at high rapidity corresponds to tracks which enter through the side of the calorimeter and are rejected by present cuts. Figs. 2.7 b) and c) show the efficiency for

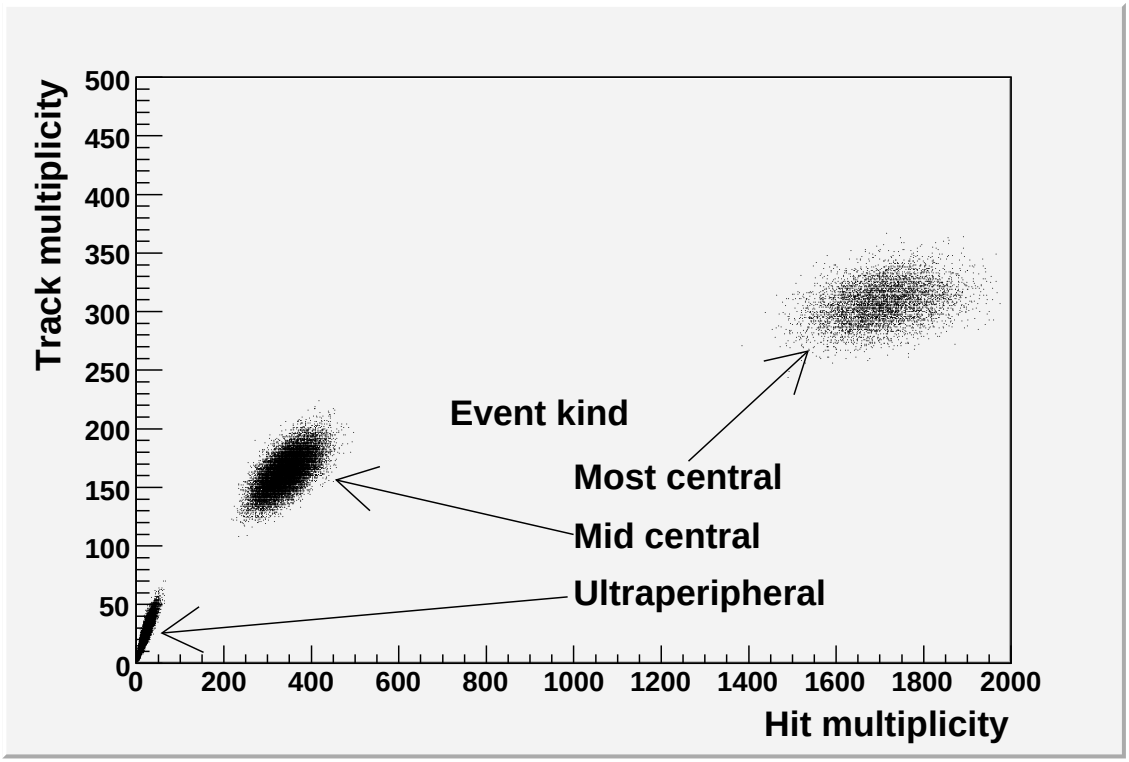

Figure 2.6: Multiplicity of tracks reconstructed in the NCC vs number of particles in the NCC acceptance.

finding and identifying electromagnetic showers in mid-central and central Au+Au collisions. There is an additional drop off in efficiency at higher rapidities where the occupancy is high, resulting from a χ^2 cut intended to remove hadrons, but that will also remove any photons that have an overlapping hadron shower. This cut reduces the reconstruction efficiency at high multiplicity.

Each track reconstructed in the NCC combines points in the calorimeter segments (corresponding to the clusters' centers of gravity) and in the PI layers, and primary vertex. The angular dependence of the position resolution for the calorimeter segments is shown in Fig. 2.8. Clusters in the EM segments are typically spread around the hit vector with $rms \sim 0.6$ cm, nearly independent of the initial particle energy. Tracks with large impact angles have a slightly degraded position resolution in the pad-structured segments of NCC, while measurements in the strip detectors PI1 and PI2 will be affected only slightly by the impact angles. A straight line fit (orthogonal regression) through **the points in the calorimeter segments, photon identifier layers and primary vertex** results in an estimate of ~ 2.5 mm for the impact position resolution on the front face of calorimeter (see TDR) and of ~ 6 mrad for the angular resolution.

Tracking also allows for the calorimeter to point towards the source of the hit particle and thus reduce the background of particles not originating from the collision vertex. The energy dependence of the pointing error, defined as the angle between the hit particle and

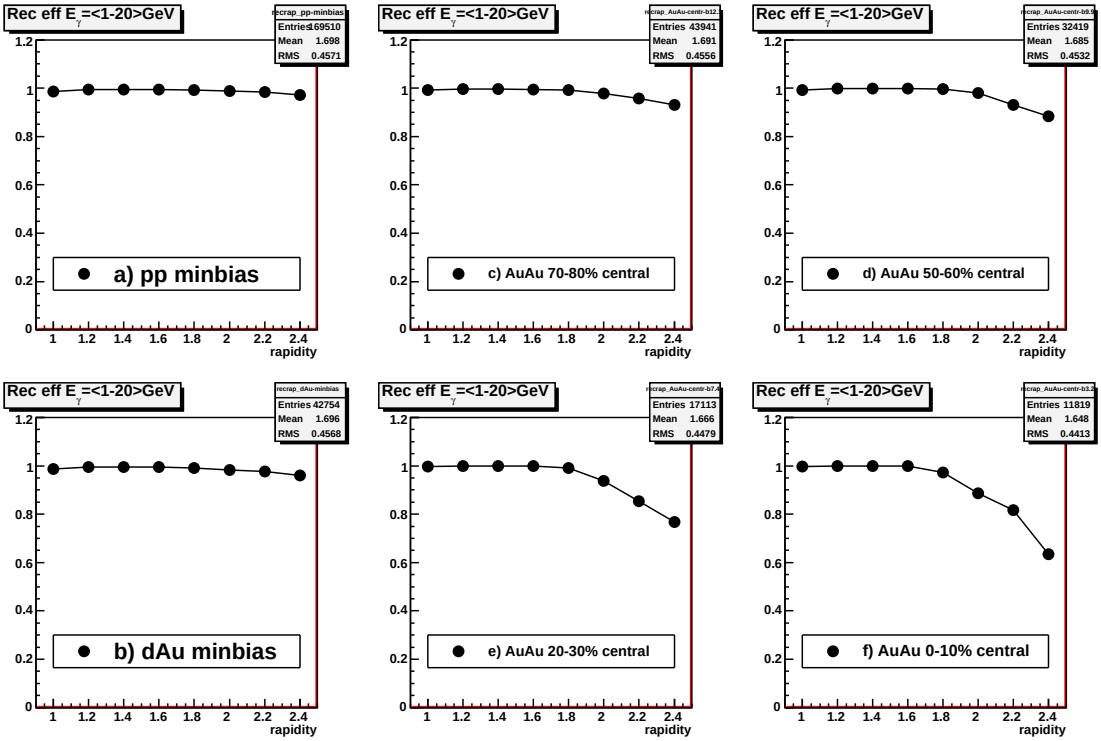

Figure 2.7: Track finding efficiency for γs between 1 and 20 GeV vs rapidity in several types of collisions

the straight line fit through all energy weighted points **excluding the primary vertex** is shown in Fig. 2.9. The pointing resolution is driven by the EM2 position resolution ($\sim$ 6 mm) and the effective track length in the EM section of the calorimeter ($\sim$ 5 cm). It is close to 0.1 rad for orthogonal impacts and drops to $\sim$ 0.18 rad at impact angles close to 45°.

2.7 Identification of Electromagnetic Tracks

There are differences between classical projective calorimeters (an example is the central EMCal of STAR) and longitudinally segmented tracking calorimeters, and each has distinct advantages in difficult high multiplicity environments. Projective geometry helps when handling high occupancies by reducing cluster multiplicities. Tracking showers in a longitudinally segmented calorimeter allows to effectively avoid this problem. But it also allows to solve the problem of identification for electromagnetic particles by measuring finer details of the shower development in the absorbing medium, which usually would require one additional measurement of particle momentum or velocity, implicit in standard ToF or E/P matching algorithms. Longitudinal segmentation allows differentiation between electromagnetic (shallow) and hadronic (deep) showers. In general the algorithms based upon shower development only allow classification of showers up to a certain probability as being of electromagnetic or hadronic origin (the latter subdivided into showering and punch-through particles including

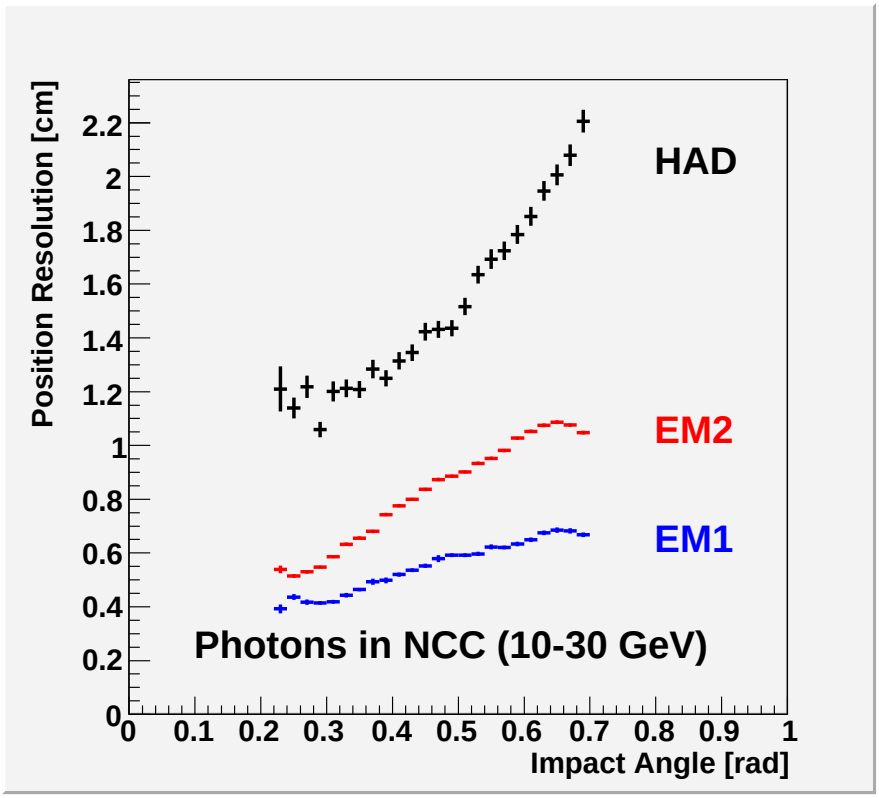

Figure 2.8: Angular dependence of the position resolution in the three NCC segments.

muons). The decision normally requires forming an estimator based upon a parametrization of the average energy and its variance in calorimeter segments (longitudinal shape analysis) and calorimeter towers (lateral shape analysis) as function of particle energy, impact angle and orientation (if the calorimeter is not axially symmetric). It also requires a good knowledge of correlations so that the proper covariance matrix can be formed. In the absence of test beam data to produce a detailed shower description, we settled on a simple polynomial parametrization of deposited energies and variances as deduced from simulations. A χ^2 estimator based upon this parametrization was used to reject non-electromagnetic tracks.

2.8 High energy photons

A comparison between simulated (blue) and reconstructed photons (passing identification tests, red) is presented in Fig. 2.10. Both real electromagnetic showers and misidentified showers of hadronic nature contribute to the spectrum of reconstructed photons. In all cases the reconstructed event had one photon embedded into it. The photon energies were uniformly distributed between 0 and 60 GeV, and the population was uniformly distributed in $cos(\theta)$ so that the large impact angles were enhanced. The simulated and reconstructed photon spectra agree well in the peripheral events. As the multiplicity of the underlying event grows, the probability of overlaps increases, distorting the energy resolution and push-

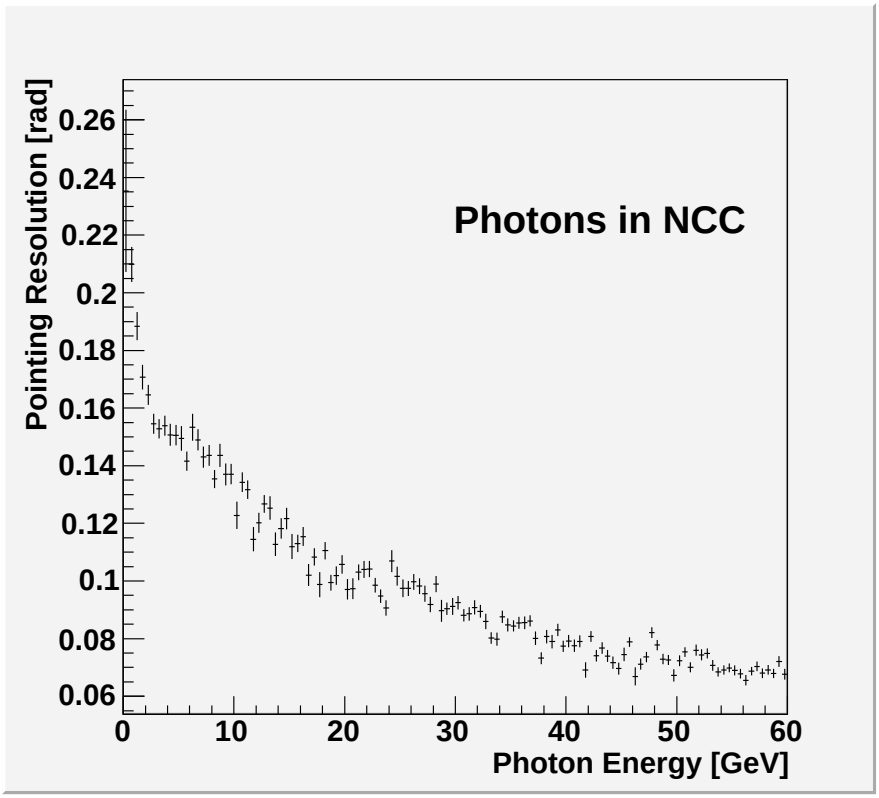

Figure 2.9: Energy dependence of the NCC pointing resolution.

ing reconstructed spectra towards larger transverse momenta (a well known effect of finite detector resolution leading to the hardening of fast falling spectra). In peripheral events the "efficiency" stays close to 1 at all but the lowest p_T; in mid-central and most central Au+Au events it is reasonable above p_T >5GeV/c and p_T >10GeV/c, respectively.

2.9 Two-track π^0s

The ability of NCC to resolve two close tracks in the pad-structured segments is intrinsically limited by a single tower size to $\sim$ 40 mr which is close to the minimum opening angle of the two photons resulting from a 5 GeV/c π^0 decay. Below this momentum the decay photons will form two distinct tracks, and π^0s can be reconstructed the traditional way, calculating an invariant mass from each pair of photon candidates within an event and estimating the combinatorial background using event mixing. Low p_T two-track π^0s were generated using the HIJING event generator. For higher p_T we embedded simulated single π^0s into HIJING events. In each centrality bin 1,000 events were generated and reconstructed.

Single photons were selected by requiring tracks with a longitudinal χ^2 <2 and a transverse χ^2 <2 as defined for the calorimetric segments. Fig. 2.11 shows the two photon invariant mass for a variety of centralities from p+p to central Au+Au, and in different p_T and rapidity ranges. Note that the p_T where the two-track method is no longer applicable depends

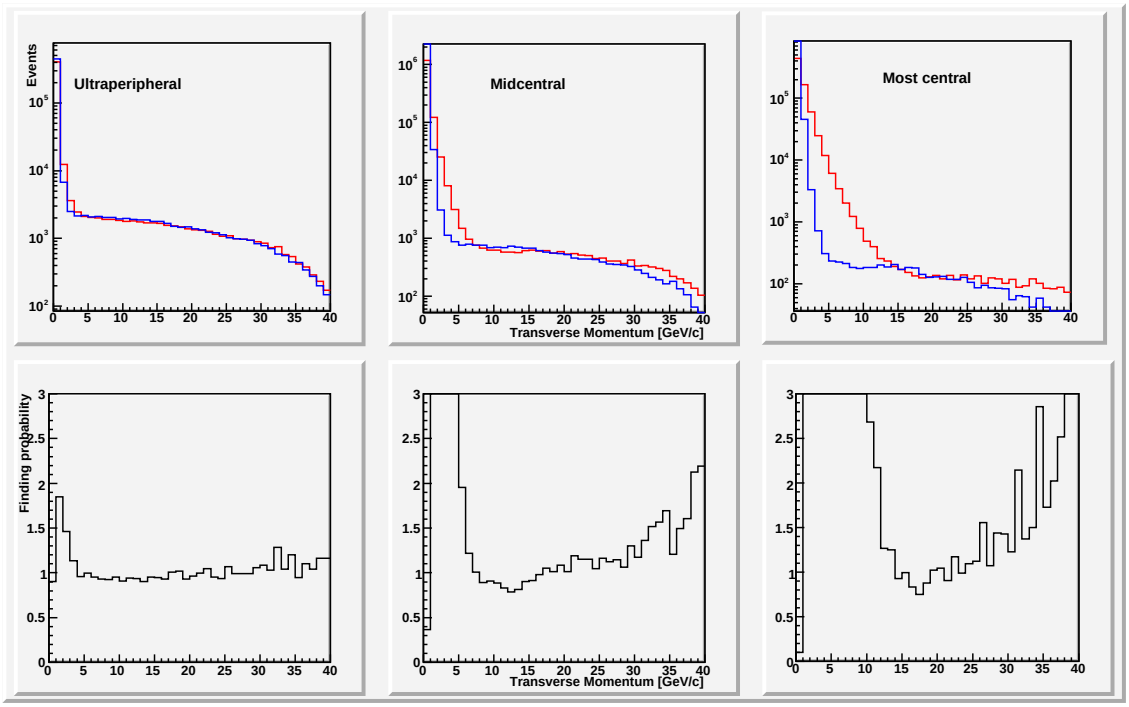

Figure 2.10: Comparison between simulated and reconstructed spectra of photons in NCC in events of different nature. Top panels - simulated photon spectra (blue) compared to reconstructed (red) spectra of electromagnetic tracks, bottom - ratio of the spectra.

on the rapidity. At $1.0 < |\eta| < 1.5$, p_T =3.5 GeV/c corresponds to π^0 energies of 6-9 GeV; for $1.5 < |\eta| < 2.0$, p_T =2 GeV/c corresponds to energies of 4-7 GeV. Since at an enegy of $\sim$ 5 GeV the two photons begin to merge, we plan to measure two-track π^0s only in the $1.0 < |\eta| < 2$ region for p+p and d+Au events and $1.0 < |\eta| < 1.5$ in Au+Au events.

2.10 Single-track π^0s

As discussed in the previous section, showers from π^0 decay photons begin to overlap above a π^0 energy of $\sim$ 5 GeV. In this case the π^0 appears as a single track and is no longer identifiable by traditional methods. We wanted to extend π^0 identification to much higher p_T, in part because of the inherent interest in high transverse momentum π^0s but also to reduce the background to the direct photon measurement. To achieve this the calorimeter is supplemented with two high resolution 2-dimensional (X and Y) position sensitive detector layers built of 0.5×60 mm^2 Si strips. If placed at appropriate depth, these detectors can measure whether the shower is produced by one or two photons. Typically such detectors are placed at $\sim$2 radiation lengths (X_0) and/or at the depth of the shower maximum. However, very extensive simulations have shown that in this configuration the picture in the second layer is totally dominated by fluctuations in the shower development and adds no information to the one extracted from the first layer. Further studies have shown that the best results

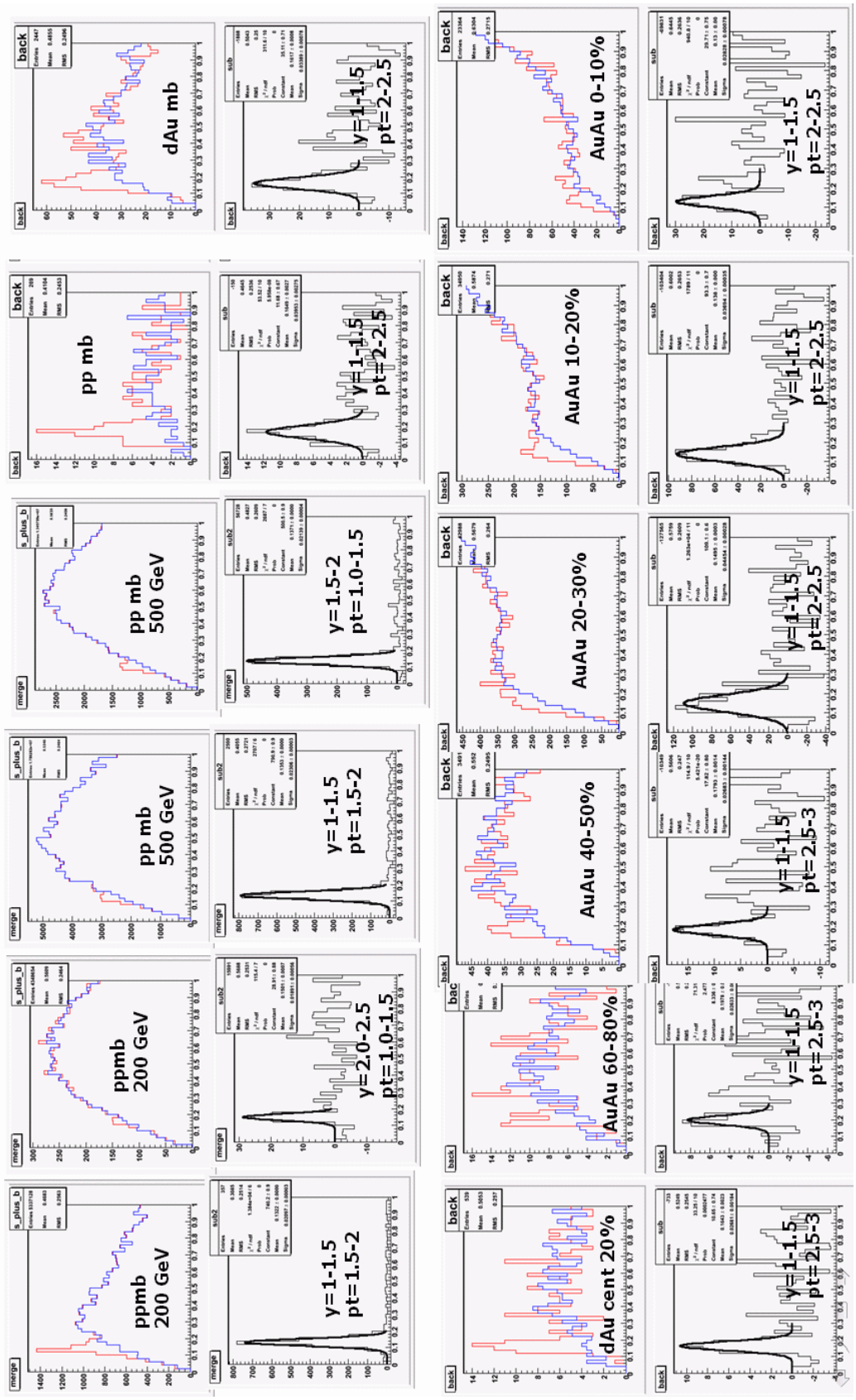

Figure 2.11: π^0 two-track invariant mass for various centrality bins. The first and third rows show the signal (red) and combinatorial background (blue), the second and fourth rows show the subtracted signal.

concerning the efficiency of photon identification and counting are achieved by positioning both layers at a depth range of 2-3 X_0.

In this analysis, each electromagnetic track with energy above 5 GeV is treated as a π^0 candidate. Strips which could be related to the track are identified and considered a "region of interest", within which we search for strip clusters separated by more than two strips. The two most energetic clusters are taken as candidate overlapping photons. Due to fluctuations, the probability of finding at least two such clusters in the region of interest is close to 100%, even in the case of tracks originating from a single electromagnetic particle. Cluster to cluster separation, independently measured in X and Y directions in both 2-D layers, is further used to compute the spatial separation and an opening angle for the candidate π^0. Since there is only one (total) energy measurement, one has to assume the decay asymmetry in order to calculate the invariant mass. One possibility (used to generate the results shown on Fig. 2.12) is to use the average of the ratio of ordered cluster amplitudes in both layers and both (X and Y) directions.

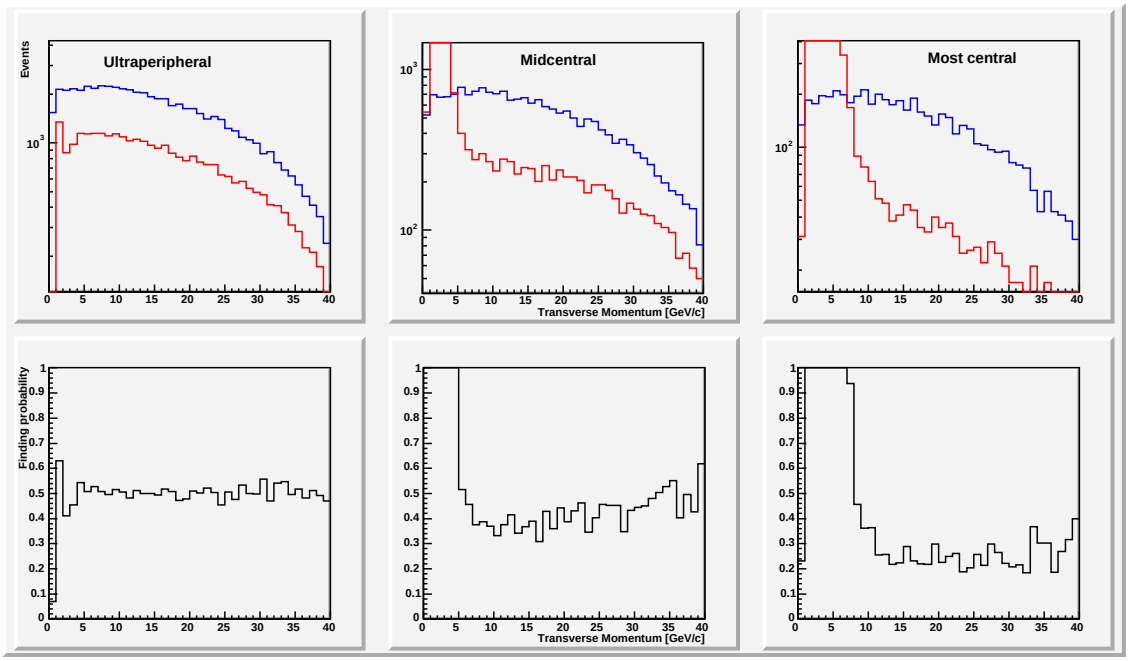

Figure 2.12: Comparison between spectra of π^0's merged into events of different centralities in the NCC and spectra of single-track π^0s reconstructed in those events. Top panels: simulated π^0 spectra (blue) compared to reconstructed spectra of single-track π^0s satisfying mass cut (red). Bottom panels: ratios of the spectra.

As expected, the π^0 finding efficiency in the peripheral events is close to that computed from GEANT single particle data. With increased centrality, at lower momenta (p_T of 5-10 GeV/c), the efficiency is affected by the overlap with the low p_T component of the underlying event (ghost π^0s). Above that range the data show gradual decrease in the efficiency almost independent of π^0 momenta. The efficiency at high momenta will be improved by optimizing pattern recognition in NCC segments for different event multiplicities.

Chapter 3

Physics measurements

3.1 Physics Signatures and Backgrounds

We have chosen to illustrate the capabilities of the NCC by doing a full simulation of the following physics signatures

- π^0's in their relations to suppression in the nuclear matter, direct photon extraction and gluon PDF measurements through γ-jet final states. Two-photon mixed background subtruction technique is used to extract π^0 sinal in p_T¡4GeV/crange. Single-track photon deconvolution and mass attribution technique is used at higher p_T's.
- R_{AA} for χ_C (χ_C nuclear suppression factor). The rapidity range for χ_C signal extraction in the most central Au+Au collisions is limited to $|\eta| < 1.5$ by occupancy considerations.

We begin by first describing some of the scientific questions which motivate these measurements:

3.1.1 π^0 Suppression and jet measurements

The energy loss of quarks and gluons in the sQGP is of critical importance in the identification of its characteristics. Based upon the suppression of high p_T π^0s at midrapidity, PHENIX has recently published the first quantitative constraints on the opacity parameters [**?**, **?**] of the sQGP - for instance the transport coefficient $\langle\hat{q}\rangle$ estimated within the framework of the Parton Quenching Model. However, the improved precision of the data raises new questions. The π^0 suppression at $y = 0$ is apparently constant up to p_T =20GeV/c (instead of exhibiting a slow, logarithmic rise predicted by ionization-type energy loss models), consistent with a Bremsstrahlung-type, constant fraction $\Delta p_T/p_T$ energy loss. Even more surprising, preliminary results on direct photon production in Au+Au indicate that at very high p_T (> 15GeV/c) photons may also be suppressed. Part of this effect ($\sim$15%) is expected from the so-called "isospin-effect" [**?**] but the preliminary data don't exclude the possibility that at some very high p_T photon suppression would be equal to that of hadrons, implying substantial in-medium changes to the structure functions. This would be of utmost

interest; unfortunately, it appears to happen at and above 15-20GeV/c, a region where the measurement in the central arm becomes technically difficult, but would be feasible with the NCC.

In order to improve the quantitative capacity for experiments to compare to various models, it also becomes necessary to have a calibrated probe that pinpoints the initial energy of the emitted parton. The energy loss of heavy quarks, initially predicted to be quite small, may in fact be rather large [**?**]. Again, as PHENIX seeks to make such measurements with the addition of vertex detectors (VTX, FVTX), it will be important in these instances as well to know the initial energy of the scattered parton implying both extracting the direct photons and doing some kind of jet measurements.

The NCC will make possible the following measurements in the area of parton energy loss:

- It will provide a precision measurement of π^0s in the forward rapidity region allowing for a quantitative determination of opacity parameters as a function of rapidity. In the forward region, there will be competing mechanisms of suppression - the suppression of parton energy loss coming from the sQGP, and the suppression due to the modification of the structure functions in the initial state. Careful measurements as a function of transverse momentum, rapidity, and centrality will allow us to separate such effects.

- It will allow a calibration of the outgoing parton, both for light and heavy quarks, by detecting an opposing direct photon, in photon-jet events. Such events are rare since they are suppressed by a factor of the electromagnetic coupling constant. In addition to giving a broader rapidity reach, the increased acceptance will greatly enhance the rate at which such events are collected.

- It will allow to extend measurements of the gluon impact on the spin of the proton. It is negligible in the region of x to which experiments have currently been sensitive - i.e. down to x$\sim 10^{-2}$. However the gluons may contribute strongly at lower x. One of the best probes for the gluons is the direct photon production via the gluon Compton scattering diagram, the latter can't be measured except if π^0 are measured and understood.

In order to make such measurements, one must first make measurements of the π^0 spectrum. Using this information, the direct photon spectrum can be extracted. Finally, correlations can be made on a statistical basis between the direct photon signal, and various high momentum particle signatures - for instance - high p_T charged pions measured in the central VTX detector.

3.1.2 χ_C Suppression Measurements

A second measurement we will present is the result of the simulation for the detection of χ_Cs, in which the χ_C decays to a J/ψ and a photon, with the photon measured in the NCC and the J/ψ measured in the muon spectrometers via its decay to 2 muons. Charmonium bound states were initially thought to be sensitive probes of deconfinement, due to screening

Table 3.1: Luminosity guidance from CAD for RHIC II. We assume a 50% duty cycle for RHIC to give a weekly integrated luminosity. We then assume a 12 week run and a 60% uptime for PHENIX to give a total integrated luminosity. The max rate is the interaction rate at peak luminosity.

Species CM Energy	p+p 200 GeV	p+p 500 GeV	p+Au 200 GeV	d+Au 200 GeV	Cu+Cu 200 GeV	Au+Au 200 GeV
lum ($s^{-1}cm^{-2}$)	1×10^{32}	5×10^{32}	2.5×10^{29}	1.9×10^{29}	8×10^{28}	7×10^{27}
interaction rate	4200	21000	320	585	248	47 kHz
lum/wk ($pb^{-1}wk^{-1}$)	33	166	0.083	0.062	0.025	0.0025
Int Lum (pb^{-1})	238	1195	0.6	0.45	0.18	0.018

effects in a gas of quarks and gluons. Recent measurements of J/ψ suppression (ref PHENIX) indicate that its suppression is very similar to what has been seen at CERN energy where the energy density is thought to be ??? times smaller. The discovery that the sQGP is strongly coupled also is a challenge to this idea since the correlation length is much larger than was originally thought. There are also other processes such as recombination which would tend to enhance the production of charmonium states. It becomes very important to measure states with various binding energies, which would be affected differently by screening effects. The χ_C is such a state, which has a binding energy of ??? compared to ??? for the J/ψ and thus weakly bound. We will describe the measurement of the suppression of the χ_C as a function of centrality. If screening effects were responsible for the suppression of charmonium, then the χ_C should be suppressed more strongly.

3.2 Luminosity and Rates

In order to estimate potential improvements to already existing measurements or kinematical reaches of the new measurements, we computed expected event rates based upon expected luminosities for RHIC-II provided by BNL Collider Accelerator Division (CAD). We then assume a 50% duty factor for the RHIC machine, and a 60% up time for the PHENIX detector during a 12 week run to obtain an integrated luminosity (see table 3.1). Similar values for RHIC-I are given in table 3.2) .

Our experience with RHIC/PHENIX running in the first 5 years of data taking shows that efficiency will further suffer from several typical losses which are listed in table 3.3. The first arises from a vertex cut, which we take to be ± 10 cm from the nominal collision point. We assume 55% efficiency from losses due to the spread of the beam. For RHIC I this will be a 35% efficency since the spread of the beam is larger. Secondly, the PHENIX minimum bias trigger uses the Beam-Beam Counters (BBC) located up- and downstream of the collision point. In the high multiplicity environment of heavy ion collisions, this trigger is almost 100% efficient. However in low multiplicity p+p and p+A collisions, the efficiency

Table 3.2: Luminosity assumptions for RHIC I. We assume a 50% duty cycle for RHIC to give a weekly integrated luminosity. We then assume a 12 week run and a 60% uptime for PHENIX to give a total integrated luminosity.

Species CM Energy	p+p 200 GeV	p+p 500 GeV	p+Au 200 GeV	d+Au 200 GeV	Cu+Cu 200 GeV	Au+Au 200 GeV
lum ($s^{-1}cm^{-2}$)	3×10^{31}	–	–	0.09×10^{29}		0.92×10^{27}
lum/wk ($pb^{-1}wk^{-1}$)	9.9	–	–	0.0028	–	0.000327
interaction rate	4200	21000	320	585	248	47 kHz
Int Lum (pb^{-1})	71.3	–	–	0.02	–	0.0024

Table 3.3: Efficiency factors added into the rate calculations. In the analysis we typically require that the vertex be within 10 cm of the nominal collision point (a requirement set by the barrel VTX detector), which results in an efficiency of 0.55 for RHIC II. For RHIC I, the beam spread is larger and results in an efficiency of 0.31. For A+A collisions the minimum bias trigger formed by the Beam-Beam counters are essentially 100% efficient, however in p+p and p+A collisions there is some loss.

Species	p+p 200 GeV	p+p 500 GeV	p+Au	d+Au	Cu+Cu	Au+Au
vertex cut RHIC II	0.55	0.55	0.55	0.55	0.55	0.55
vertex cut RHIC I	0.31	0.31	0.31	0.31	0.31	0.31
min bias trigger eff	0.75	0.75	0.90	0.90	1.0	1.0
reconstruction eff	0.80	0.80	0.80	0.80	0.80	0.80
total eff factor RHIC II	0.33	0.33	0.40	0.40	0.44	0.44
total eff factor RHIC I	0.19	0.19	0.23	0.23	0.25	0.25

drops since in some cases, no particles actually trigger the BBC. Finally we have taken 80% for the reconstruction efficiency, a reasonable number from our experience in the last several years.

Fig. 3.1 shows the raw p_T distributions for π^0's in pp (RHIC II integrated luminocity of 240 pb^{-1} compared to 0-10 % central AuAu events for integrated luminosity of 18 nb^{-1} (see table 3.1). The following data were used as an input to these calculations

- Inelastic cross section normalized to $p + p$ inelastic cross section at a similar collision energy, σ_{inel}^{norm}, see table 3.4;
- Average number of underlying binary nubleon-nucleon collisons, N_{coll}, see table 3.4;
- (a) NLO pQCD [**?**] to compute inclusive hard scattering cross section in $p + p$ in the

pseudorapidity acceptance of the detector σ^{pp}_{hard}, or (b) PYTHIA to compute the cross section for γ-jet production in $p+p$ ($\sigma^{pp}_{\gamma-jet}$);

	pAu200	dAu200	CuCu200	AuAu200
σ^{norm}_{inel}	30.	73.7	78.	148.
N_{coll}	6.	8.5	52.	258

Table 3.4: Inelastic cross section normalized to $p+p$ inelastic cross section, σ^{norm}_{inel}, and average number of underlying binary nubleon-nucleon collisons, N_{coll} for various collision systems and energies.

The single-particle rate, N_s was calculated as

$$N_s = \sigma^{pp}_{hard}\hat{L}2\pi p_T \sigma^{norm}_{inel} N_{coll} \tag{3.1}$$

and corrected for losses due to process dependent acceptance variations, an example is γ–jet rate, $N_{\gamma-jet}$, calculated as:

$$N_{\gamma--jet} = \sigma^{pp}_{\gamma--jet}\hat{L}\sigma^{norm}_{inel} C_{acc} N_{coll} \tag{3.2}$$

where C_{acc} are the γ–jet acceptance factors from table 3.5.

	5–10	10–15	20–100
C_{acc}	76e-5	423e-5	1394e-5
N_{pi^0}	500k	200k	40k

Table 3.5: γ–jet acceptance factors, C_{acc}, and number of π^0, N_{π^0}, measured in the NCC for γ in the Central Arm for various p_T ranges of the direct photon, in GeV/c, at $\sqrt{s} = 500$GeV.

We also include in this plot the rate estimates for direct photons and π^0's in the central AuAu events from the same source. The latter data also account for the high p_T suppresion of π^0 as measured in central arm.

Statistically PHENIX upgraded with NCC can extend its transverse momentum reach for π^0 and direct photon measurements towards $30\,\mathrm{GeV}/c$ limit set by expected yields in 12 weeks long running period of PHENIX in RHIC II era.

3.3 Physics with π^0's

A number of physics signals rely heavily on π^0 measurements be it through the mass peak in the two-photon effective mass distribution or via photon identification and mass attribution to single high p_T tracks consistent with being due to overlapping photons from π^0 decays. To name just a few: the nuclear modification factor, R_{AA}, of neutral pions at forward rapidity;

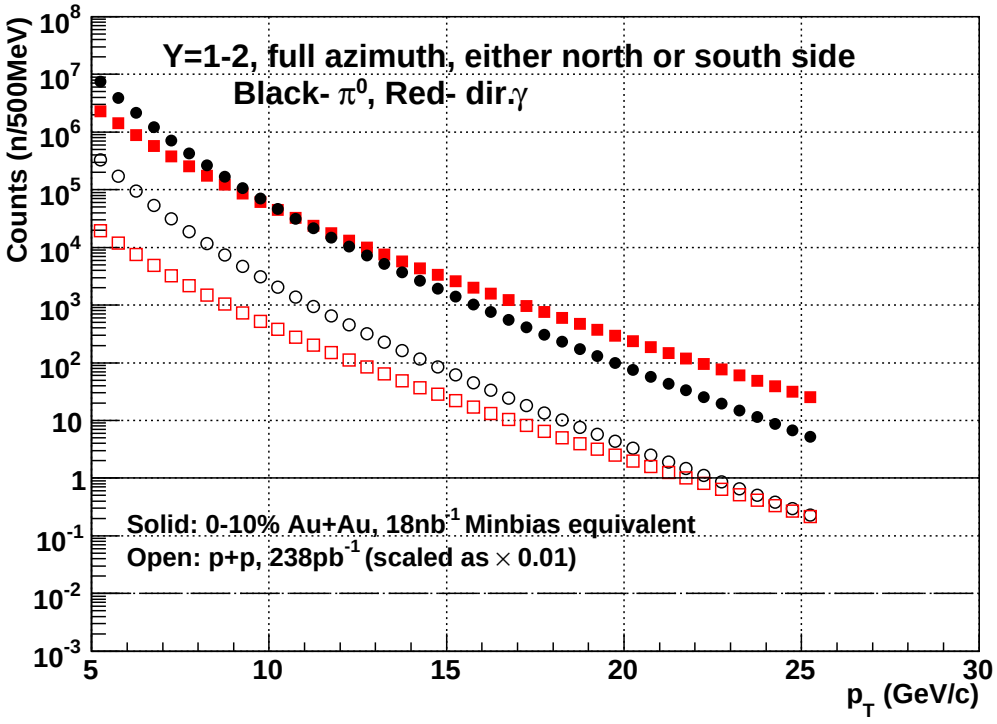

Figure 3.1: Rate estimate for π^0 and direct photons for pp and AuAu (0-10 % centrality) collisions at 200 GeV based upon expected RHIC-II integrated luminosity (12 weeks of running).

the PDF of gluons at low-x through the measurement of a jet related π^0 at forward rapidity in conjunction with direct photon in the central arm; the measurement of direct photons at forward rapidity, for which the single-track π^0's are a source of background.

The expected numbers of measured direct photons and π^0's in the NCC as well as of direct photon-jet events were estimated from NLO pQCD calculations of (ref to Werner) (see Fig. 3.1). Similar estimates accounting for the acceptance effects in correlated γ–jet production (3.5) were also used to study upgrade effectiveness for gluon PDF measurements in the low x limit (see below).

Corrections for losses due to reconstruction inefficiencies (largely overestimated due to deficiencies of reconstruction algorithms) as discussed in earlier chapters of this document were used to compute statistical and systematic errors apllicable to final physics observables presented in the next sections. The estimates were made for various collision systems (p+p, p+Au, d+Au, Cu+Cu, Au+Au) and range of centralities.

3.3.1 π^0 signal reconstruction in two-photon combinations

The details of the procedure used to reconstruct π^0 signal in effective mass spectra were described in Chapter 2 of this document. A beautiful signal easy to extract is present at all raidity values (impact angles) in pp and dAu data, efficiency drops down in high multiplicity

central AuAu events so the momentum threshold must be raized for π^0's to compete with backgrownd of soft showers due to non-electromagnetic component of secondary particles in the event. The efficiency of π^0 reconstruction counting residuall hits left inside π^0 mass range in the two-photon effective mass distribution after background subtraction is shown on Fig. 3.2 for minimum bias proton-proton events.

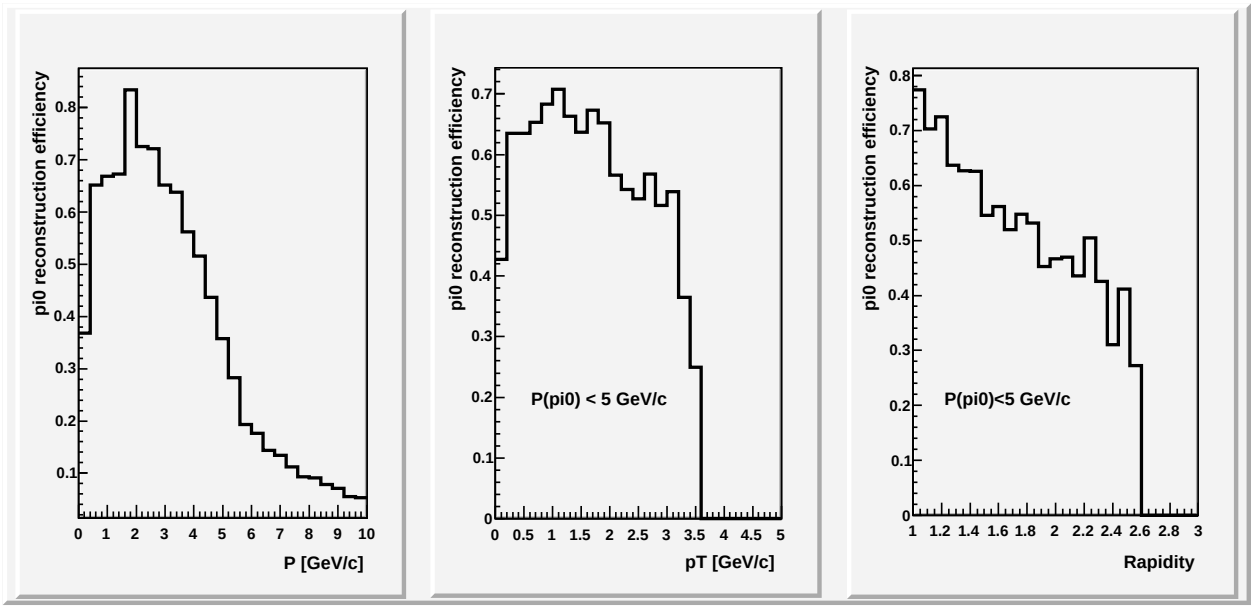

Figure 3.2: Efficiency of finding a π^0 using the two track invariant mass method vs π^0 momentum (left), transverse momentum (center) and rapidity (right).

The losses at low momenta (left panel) reflect acceptance and degraded resolution (low energy photons are strongly affected by underlying event). The efficiency also drops off rapidly at large momenta because the photons from π^0's with energies greater than about 5GeV begin to merge in the NCC. Forπ^0's with momenta below 5 GeV/c the efficiency varies little as function of transverse momenta which is now geometrically limited to $\sim 3.5 GeV/c$ and drops towards larger rapidity reflecting the change in the flight path of photons at different impact angles.

3.3.2 π^0 signal reconstruction in a single-track mode

The technique of reconstructing and identifying single-track π^0's has been described in some detail already, but we will repeat key features here. Fig. 3.3 shows the invariant mass distribution obtained in simulated events consisting of a single thrown π^0. In this case, 10000 π^0's with $12 < p_T < 13\,\mathrm{GeV/c}$ were thrown in the NCC acceptance. Over 90% of those particles were reconstructed as single-track π^0 candidates; that is, as a single set of calorimeter clusters in the NCC satisfying an electromagnetic χ^2 cut and with a separable pair of clusters in each of the strip layers. Of the thrown π^0's, roughly 55% then have an invariant mass that falls within $\pm 40\,\mathrm{MeV}$ of the nominal π^0 mass.

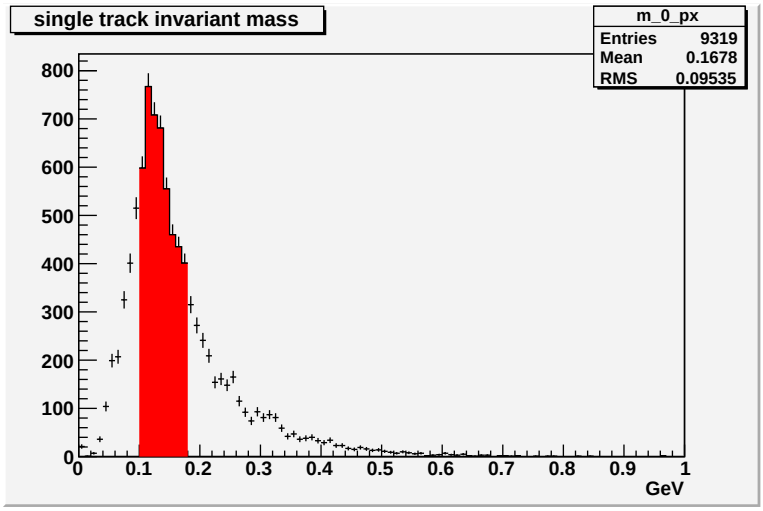

Figure 3.3: Invariant mass of all single-track π^0 candidates in single particle GEANT events.

The key question, however, is how well one can reconstruct these single-track π^0's in central Au+Au events. And, more to the point, one want to know how the extraction of physics quantities in central Au+Au depends on the reconstruction of the single-track π^0. There are several quantities needed for this estimate. One is the reconstruction efficiency, the next is the probability for misidentifying a particle as a single-track π^0 (primarily single photons) and the final bit is an estimate of the relative abundance of true single-track π^0's and single photons at the same (y, p_T).

We will use here a method of determining the reconstruction and identification efficiency for single-track π^0's that is very similar to that described by WA98 []. We throw a single π^0 and recontruct it. Then we throw a full central Au+Au HIJING event and reconstruct that. Finally, we mix the single π^0 into the HIJING event and reconstruct that. From this reconstructed mixed event we identify tracks that already appeared in the reconstruction of the plain HIJING event. We search through the remaining tracks to see if the originally thrown π^0 can be found. We obtain the efficiency by dividing the ditribution of π^0's in the final instance by the distribution of π^0's reconstructed from single track events. A two-dimensional plot of the reconstuction efficiency in central Au+Au as a function of (y, p_T) is shown in Fig. 3.4.

The efficiency peaks at a value around 20% and falls off with increasing p_T and rapidity. Again, this should be compared to an efficiency of about 55% for a single π^0, not embedded in an underlying event as shown in Fig. 3.5. The ratio of fragmentation photons to π^0 in p+p and d+Au is significantly less than one (O(10^{-3}) at low p_T and rises with increasing p_T (arXiv:nucl-th/0703069v1 and PLB 562, 1-2, 45 (2003)). Fig. 3.5 also shows the probability of single photons being misreconstructed as single-track π^0's.

In determining the uncertainity on R_{AA} we need to take into accound the relative uncertainties on the π^0 yield in Au+Au and in p+p, which depend on (y,p_T).

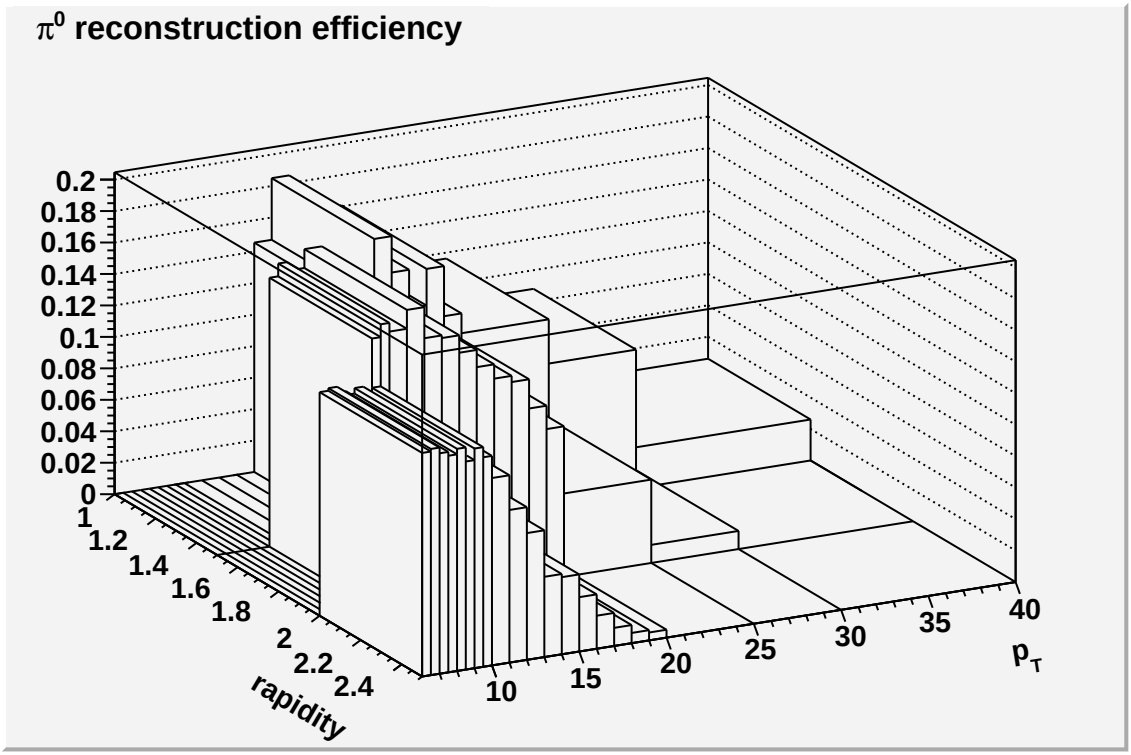

Figure 3.4: Efficiency for reconstructing π^0's in central Au+Au HIJING events as a function of (y, p_T).

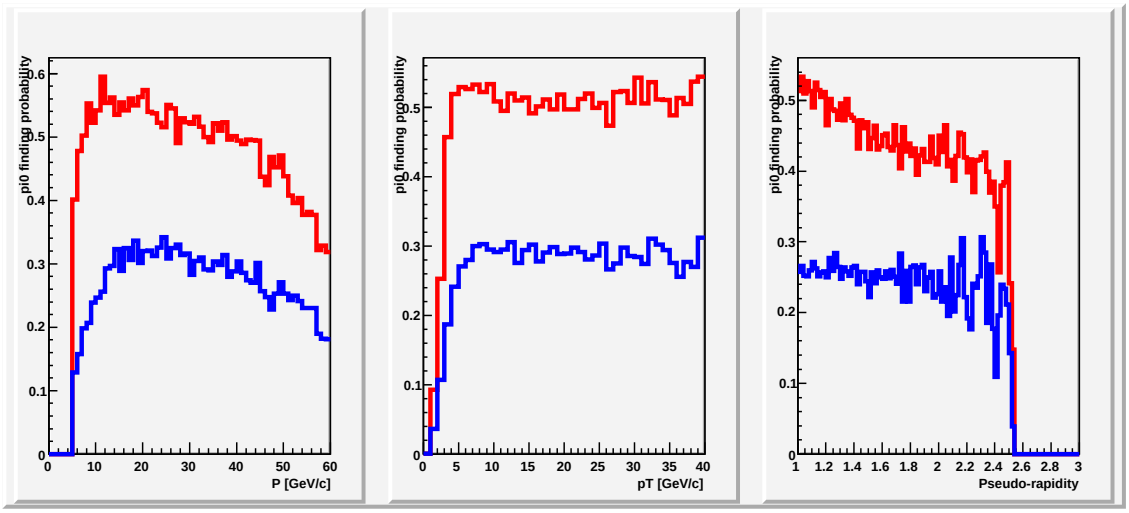

Figure 3.5: Probability of reconstructing a thrown single π^0 as a single-track π^0 (red lines) compared to the same probability for a thrown single photon (blue lines) vs momentum, transverse momentum and pseudorapidity.

3.3.3 π^0 R_{AA}

Low p_T π^0s will be measured with minimum bias trigger, and in our estimates we assume that both for p+p and Au+Au collisions we can record 10^9 events resulting in γ/π^0 yields close to those shown in Fig. 3.1. For triggered p+p events, the required rejection factor is $\sim 10K$ in order to make use of the entire bandwidth at RHIC II luminosities - for this the threshold must be set to ∼8 GeV. For Au+Au the required rejection factor is ∼30. While the estimates below are based upon central arm (midrapidity) rates, the rejection factors should be similar in the 1.0-1.5 rapidity range.

The signal extracted from the (necessarily limited) number of simulated events has been scaled to full luminosity as follows. For p_T <4 GeV/c HIJING was used directly, therefore, adjustments for cross-section were not needed: the data were simply scaled up to the appropriate luminosity. At higher momenta we "embedded" single π^0s into "real" events. In order to get the right statistics first we found the appropriate luminosity corresponding to the actual number of embedded particles, then we added the proper number of non-embedded (pure background) events, finally we scaled the resulting plot to RHIC-II luminosity (1B minimum bias events for p_T <8 GeV/c and the full RHIC-II luminosity above that).

Detector effects (resolution, overlaps, misidentification, *etc.*) distort the measured spectrum. The original π^0 spectrum has been restored as follows (the procedure is similar to the one used in the central arm). First we chose an approximate spectral shape - in this case a simple power law for the lower centralities and a exponential for the higher centralities, and generate an "input histogram" with it (in a specific slice of rapidity). Next (using the known kinematics) we let the π^0s decay. The resulting photons are smeared with the known resolution function of the detector, acceptance cuts are applied (opening angle, energy, asymmetry) to match the cuts used in the data analysis, and we fill a second, "output histogram" with the reconstructed p_T of the properly reconstructed π^0s. (Note that the rapidity doesn't change appreciably.) The detector response function DRF is then the ratio

$$DRF = \frac{output\ histogram}{input\ histogram}$$

The measured p_T spectrum is then divided by the DRF giving us a initial estimate of the real p_T spectrum. This is then used as input and the whole procedure is repeated until the input and output spectra agree. Fig. 3.6 illustrates the convergence of such unfolding using central arm data: already after the first iteration the differences between the unfolded measured and the true input spectrum are less than 5%.

We then scale the p+p spectrum by the number of binary collisions in Au+Au and divide by it the corresponding Au+Au spectrum to get the nuclear modification factor R_{AA} as shown in Fig. 3.7 for various centrality values. Note that the error bars are statistical only and are multiplied by a factor of 10 to make them visible.

3.3.4 π^0 measurements and direct photons

π^0's are the major background to direct photons which are defined as those not coming from final state hadron decays ($\pi^0 \to \gamma\gamma$, $\eta \to \gamma\gamma$, *etc.*). The signal/background is ∼10-20% at

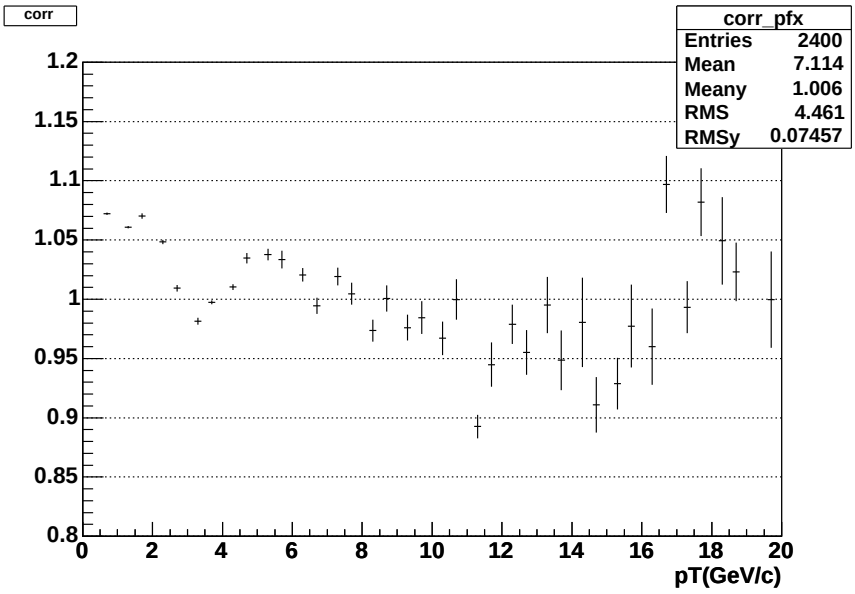

Figure 3.6: Ratio of the unfolded measured spectrum and the true input spectrum after the first iteration. Example (from a central arm analysis) how fast the procedure converges.

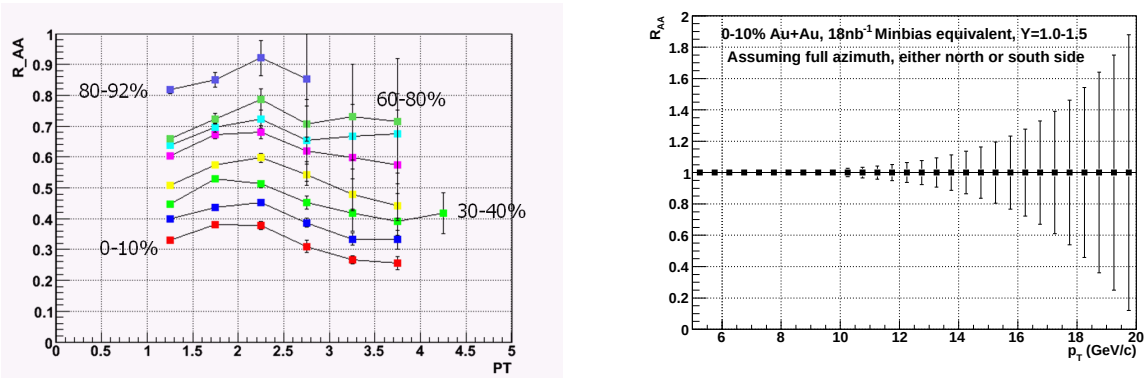

Figure 3.7: Left figure: R_{AA} for $\pi^0 \rightarrow \gamma + \gamma$ for various values of centrality. The error bars are multiplied by a factor of 10 to make them visible. The value of R_{AA} is assumed to be the same as that seen in the central arms, the error bars reflect the precision possible from a one run at RHIC II luminosities. The p_T reached is about 4 GeV. Above this p_T, the single track π^0 takes over. Right Figure: R_{AA} for "single track" π^0's. The error bars reflect the precision possible in one run at RHIC II luminosities. We assume a suppression pattern simillar to that seen in the central arms, hence statistics runs out at 15 GeV (Dave is this correct?)

p_T¡5GeV/c which makes the measurement very difficult. At higher p_T S/B rises quickly (as can be inferred from Fig. 3.1), particularly in central Au+Au collisions, where π^0 production above 5 GeV/c is suppressed by a factor of five [**?**]. Of course this gain comes at a price of increased occupancy and overlap probability from the underlying event.

The basic steps of the direct photon analysis as implememnted in PHENIX are:

- Measure inclusive photon yield;
- Reconstruct π^0 (and η) spectra;
- Calculate decay photon yield based on the reconstructed π^0;
- Calculate double ratio (R) of $(\gamma_{meas}/{\pi^0}_{meas})/(\gamma_{bkgd.}/{\pi^0}_{fit})$;

To simplify the calculation, R is defined as "$(N^{\gamma}_{inc.}/N^{\pi^0})_{meas.}/(N^{\gamma}_{bg.}/N^{\pi^0})_{MC}$".

In what follows we consider rapidity region of y=1.0-2.0, where single-track γ/π^0 component is better studied so the efficiency numbers could be obtained. The calculated reconstruction efficiency for the photons with p_T¿5GeV/c in NCC is ∼90 %, mass cut to remove obvious single-track π^0 candidates reduces it to ∼ 75 % in ultra peripheral, and ∼50 % in most central events. Uncertainty in the energy scale and fitting errors are treated as systematic errors.

We estimated ∼10 % systematic error on reconstructing, by taking the full difference of 100 % and 90 % above. We assume here that $\sim 15 \div 40\%$ (depending on centrality) of single photons misidentified as single track π^0 can be corrected for by a simulation study.

We estimated ∼10 % systematic error on reconstructing single inclusive photons due to residual mistreated single π^0's. Although the energy scale and smearing can be corrected for, we add ∼10% systematic error (this error is expected to calcell in γ/π^0 double ratio).

The estimated total errors from above listed contributions is ∼16 %.

The following errors which could contribute to the systematics in measured yields are currently ignored:

- Hadron contamination to single track π^0 or single photons (should be negligible for all hadrons except antyneutrons which are suppressed in the forward direction);
- Contributions of particles from off-vertex sources;
- Prompt electrons which we expect to be tagged by the FVTX.

The predicted ratios (calculated as $R - 1$, instead of R) are shown in Fig. 3.8. The shaded areas have too large ambiguities in efficiency determination of π^0 and single inclusive photons for the measurement to be practical.

The direct photon yield can be obtained as:

$$N^{\gamma}_{dir.} \;=\; N^{\gamma}_{inc.} \cdot \left(1 - \frac{1}{R}\right) \tag{3.3}$$

When the error components are factorized as "$N^{\gamma}_{inc.}$", "N^{π^0}", and "$(N^{\gamma}_{bg.}/N^{\pi^0})_{MC} = N^{MC}$", the error on direct photon can be propagated as following:

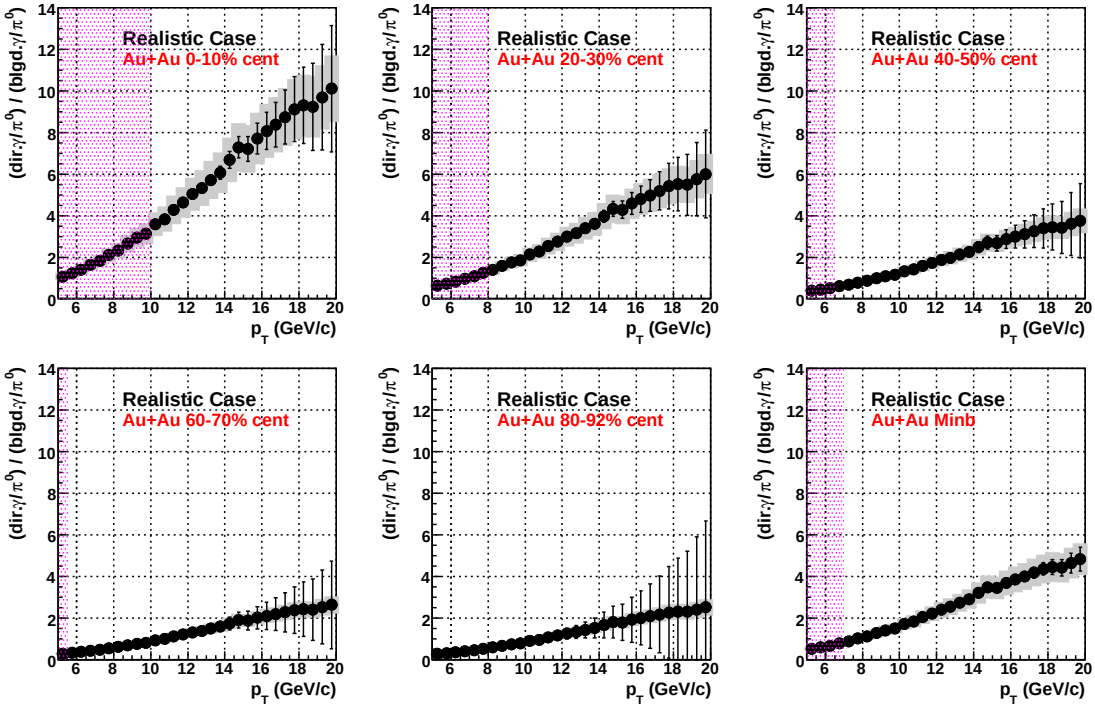

Figure 3.8: Double ratios for realistic case.

$$(\delta N^{\gamma}_{dir.})^2 = (\delta N^{\gamma}_{inc.})^2 \left(\frac{\delta N^{\gamma}_{dir.}}{\delta N^{\gamma}_{inc.}}\right)^2 + (\delta N^{\pi^0})^2 \left(\frac{\delta N^{\gamma}_{dir.}}{\delta N^{\pi^0}}\right)^2 + (\delta N^{MC})^2 \left(\frac{\delta N^{\gamma}_{dir.}}{\delta N^{MC}}\right)^2 \quad (3.4)$$

$$= (\delta N^{\gamma}_{inc.})^2 \left(\left(1 - \frac{1}{R}\right) + N^{\gamma}_{inc.} \cdot \frac{1}{R^2} \cdot \frac{\delta R}{\delta N^{\gamma}_{inc.}}\right)^2 \quad (3.5)$$

$$+ (\delta N^{\pi^0})^2 \left(N^{\gamma}_{inc.} \cdot \frac{1}{R^2} \cdot \frac{\delta R}{\delta N^{\pi^0}}\right)^2 + (\delta N^{MC})^2 \left(N^{\gamma}_{inc.} \cdot \frac{1}{R^2} \cdot \frac{\delta R}{\delta N^{MC}}\right)^2 \quad (3.6)$$

$$= (\delta N^{\gamma}_{inc.})^2 + (\delta N^{\pi^0})^2 (N^{MC})^2 + (\delta N^{MC})^2 (N^{\pi^0})^2 \quad (3.7)$$

$$= (\delta N^{\gamma}_{inc.})^2 + \left(\frac{\delta N^{\pi^0}}{N^{\pi^0}}\right)^2 \left(\frac{N^{\gamma}_{inc.}}{R}\right)^2 + \left(\frac{\delta N^{MC}}{N^{MC}}\right)^2 \left(\frac{N^{\gamma}_{inc.}}{R}\right)^2 . \quad (3.8)$$

Then,

$$\left(\frac{\delta N^{\gamma}_{dir.}}{N^{\gamma}_{dir.}}\right)^2 = \left(\frac{R}{R-1}\right)^2 \cdot \left(\frac{\delta N^{\gamma}_{inc.}}{N^{\gamma}_{inc.}}\right)^2 + \left(\frac{1}{R-1}\right)^2 \cdot \left(\left(\frac{\delta N^{\pi^0}}{N^{\pi^0}}\right)^2 + \left(\frac{\delta N^{MC}}{N^{MC}}\right)^2\right) . \quad (3.9)$$

In this case, systematic error on "MC" is zero, that on "gamma" is 10 %, and that on "pi0" is 12.2 %. The statistical error is propagated similarily.

Thus calculated direct photon spectra and direct photon R_{AA} are shown in Fig. 3.9 and Fig. 3.10, respectively.

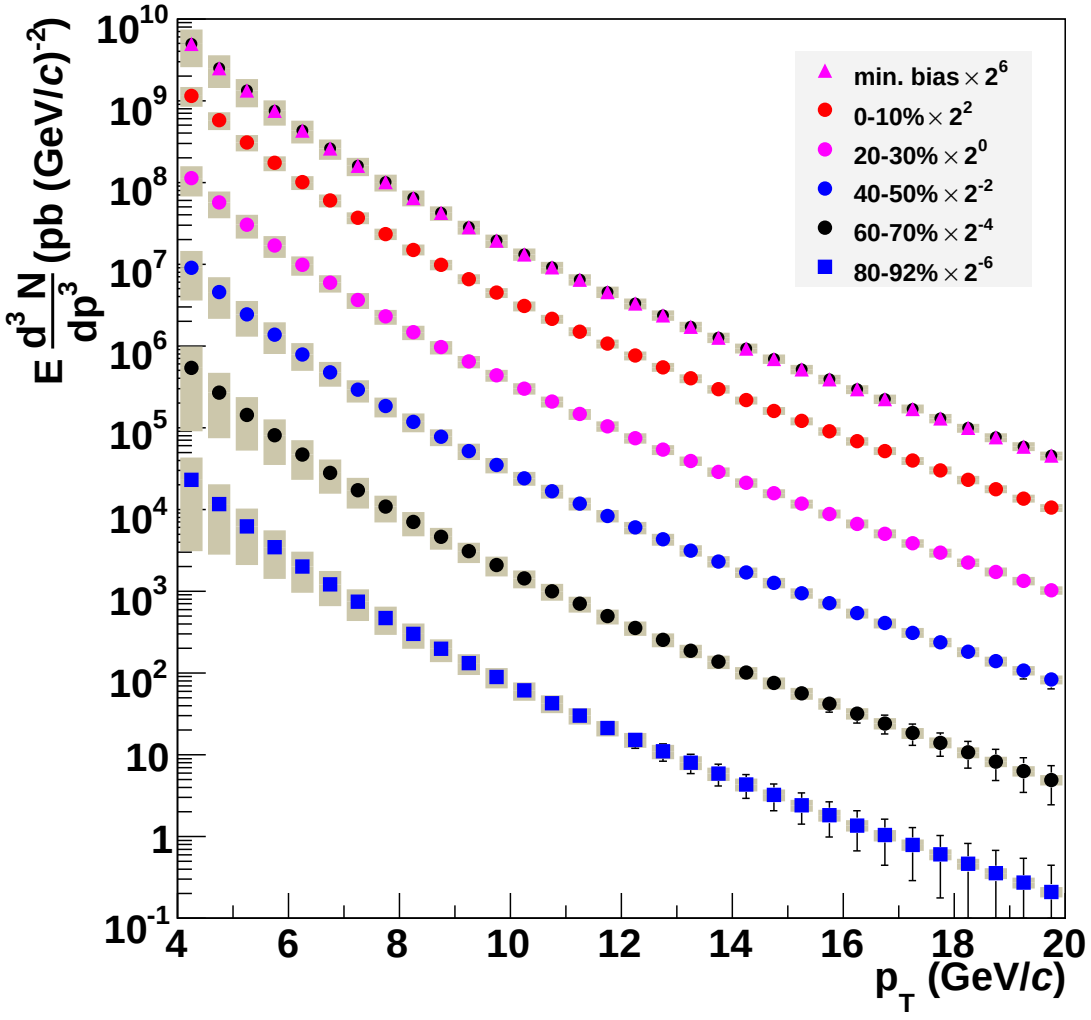

Figure 3.9: Direct photon spectra in Au+Au

3.3.5 π^0 measurements and Jets

The third segment of the NCC, the aptly named HAD segment, increases the calorimeter thickness to 1.4 absorbtion lengths L_{abs} to help with hadron rejection. As a byproduct it also improves hadronic energy measurement what is particularly crucial for PHENIX's jet reconstruction abilities, since the calorimeter is not fronted by a spectrometer which would allow one to measure the momentum of the charged hadronic fragments. In Fig. 3.11, a PYTHIA jet energy is compared to the total reconstructed and "electromagnetic" energies to show that the NCC will make relatively decent reconstructions of jets in both modes.

Use the following relations to get the kinematical variables, where y_3 refers to the photon and y_4 refers to the jet. M_T is taken as the p_T of the direct photon. Note that only the direction and not the energy of the jet is used.

$x_1^{meas} = \frac{m_T}{\sqrt{s}}(e^{y_3} + e^{y_4}) x_2^{meas} = \frac{m_T}{\sqrt{s}}(e^{-y_3} + e^{-y_4})$

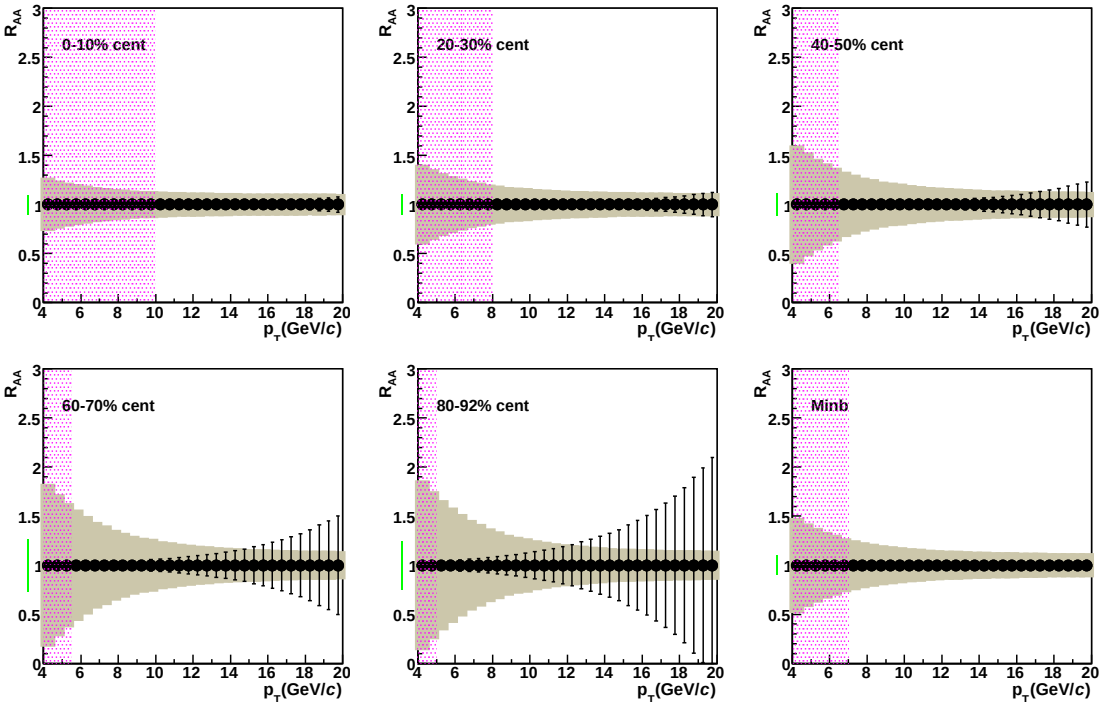

Figure 3.10: Direct photon RAA in Au+Au

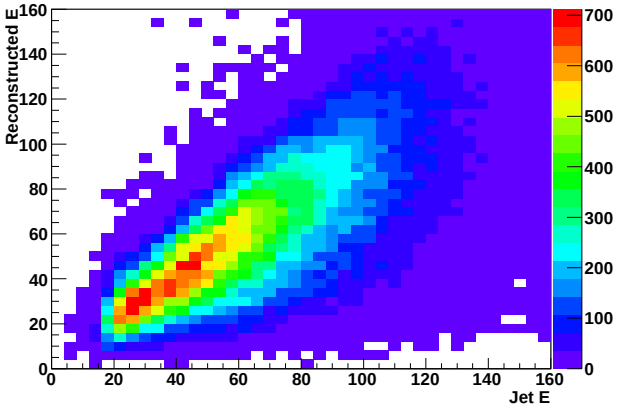

Figure 3.11: Reconstructed Jet Energy from a Cone within $\Delta\ R < 0.5$ in a full PISA simulation of the NCC, versus the PYTHIA Jet Energy in GeV

Since the error in the x-reconstruction for a LO analysis is $dx = \frac{x dp_T}{p_T} \oplus \frac{p_T e^{y_3} dy_3}{\sqrt{s}} \oplus \frac{p_T e^{y_4} dy_4}{\sqrt{s}}$, it is crucial to reconstruct the jet angle fairly well.[1] The angular resolution for jets in the NCC as deduced from simulation is $\sim 0.1\ rad'$ and contributes about 10% to the x resolution, which is below the amount expected from NLO radiative effects.

3.3.6 π^0 measurements and spin physics

Prompt photon production provides the most direct access to the gluon polarization, as it is dominated by the gluon-Compton process (85 percent of the cross section). Present measuarements indicate that ΔG is small in the kinematic range of the central region. However, these measurements are not sensitive to low-x and do not rule out even very large values of ΔG. For example, GS-C, a parameterization of the gluon structure that is consistent with all experimental data, has a very large value of ΔG, as illustrated in Fig. 3.12.

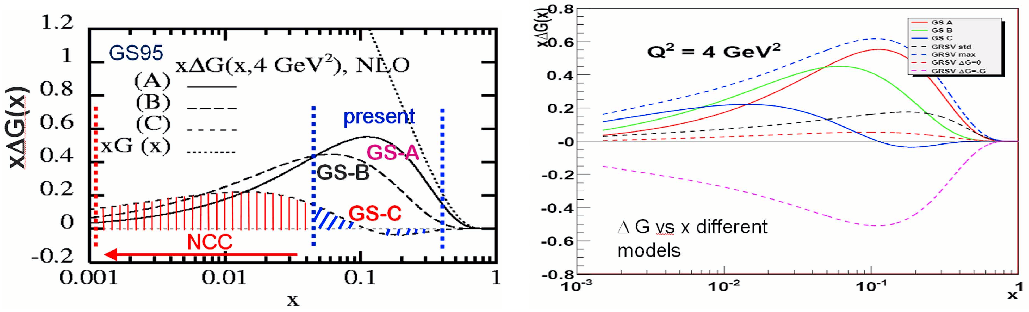

Figure 3.12: Variety of parameterizaiton for ΔG Q^2=4 GeV^2. Parameterizations with large contributions at low-x, such as GS-C cannot be distinguised without forward measurements.

It is thefore essential to extend our measurements to low-x. The additional geometric acceptance with the addition of the Nose Cone Calorimeter in the forward direction extends the measurement of the gluon polarization from $0.01 < x < 0.3$ down to about $x = 0.001$.

Δg is extracted from measurements of the double spin longitudinal asymmetry (A_{LL}):

$$A_{LL} = \frac{\sigma_{++} - \sigma_{+-}}{\sigma_{++} + \sigma_{+-}} = \frac{\Delta g(x_1, Q^2)}{g(x_1, Q^2)} \otimes \frac{\Delta q(x_2, Q^2)}{q(x_2, Q^2)} \otimes \hat{a}_{LL}(s, t, u)$$

for these various channels, where $++$ denotes same sign helicty and $+-$ denotes opposite sign helicity. A_{LL} is then connected to Δg in the context of pQCD.

As part of the work on this document we have completed a full simulation to estimate the sensitivity to A_{LL} for the prompt photon channel. The expected A_{LL} value for direct photons ($g + q \rightarrow \gamma + X$) in the NCC have been applied to to weight individual PYTHIA events. The technique of estimating A_{LL} consists of calculating a weighting factor for A_{LL} on an event-by-event basis in the simulation. The weighting factor w is expressed in the factorized form of A_{LL}:

[1] In a γ-jet analysis the p_T would be determined from the photon's p_T.

$$w = r_g(x_1, Q^2) \otimes r_q(x_2, Q^2) \otimes \hat{a}_{LL}(s, t, u)$$

Here r is the ratio of $\Delta g(\Delta q)$ polarized density functions to the $g(q)$ unpolarized density functions and $\hat{a}_{LL}$ is the partonic asymmetry which is calculable in pQCD.

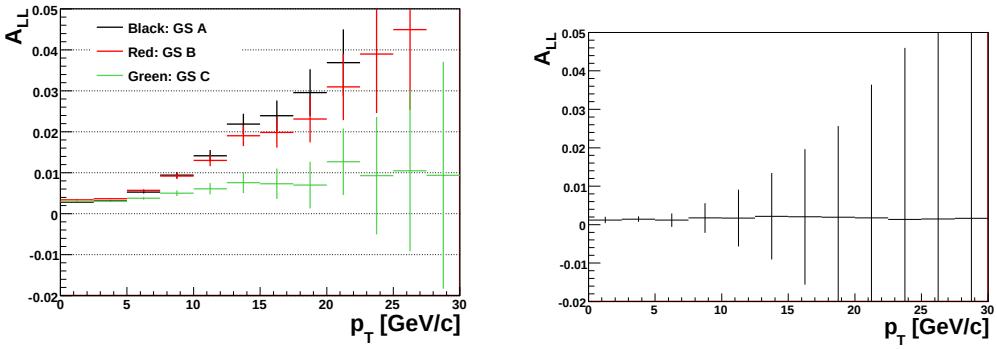

Figure 3.13: A_{LL} for prompt photons in the NCC for GS-A,B,C (left) and central arms for GS-C (right). Statistics are for running with one NCC for one year with 70% polarization.

The error bars in Fig. 3.13 reflect statistical errors only. Further studies are being conducted on the isolation cuts to optimize the signal to background ratio.

3.4 The χ_C

In this study we present an R_AA measurement for the χ_c given realistic backgrounds and detector response. The muon arms provide the measurement of the J/ψ via its decay to dimuons. For our purposes the Level 2 dimuon trigger in the muon arms is sufficient in determining whether there is a dimuon event in the rapidity of interest.

We began by generating HIJING background events for each collision type (p+p, d+Au, Au+Au) in varying centrality classes. The signal was generated using a combination of χ_c and J/ψ single particle generators to give us an appropriate 40:60 mixture of J/ψs from the feeddown of χ_c and directly produced J/ψ. To get large enough statistics at high p_T, we used a flat (p_T, y) distribution which was fed through PISA simulation and then rescaled to expected yields coming from RHIC II. The p_T and rapidity range studied are $0 < p_T <$ 10GeV/c and $1 < |\eta| < 3$. The transverse momentum range was split into 20 bins, and the rapidity into 6 bins, 3 bins each in the North and South arms. Since we were also concerned with looking at the *d*-going side and *Au*-going side separately in d+Au collisions, we generated and analyzed the signal in both North and South directions separately.

Once the signal and background files were generated, they were merged to produce simulated DST's. This merging is done at the raw event level. The merged files were then subjected to pattern recognition and reconstuction routines and output DST's were made for further analysis. The generated data samples are summarized in table 3.6

Table 3.6: Generated number of events for the χ_C study.

Interaction	Centrality	Number of Events
p+p	minbias	200,000
d+Au	minbias	245,000
d+Au	b=0-5, 0-40%	145,000
Au+Au	minbias	
Au+Au	b=0-3.2, 0-10%	

In order to make a measurement on the process $\chi_c \rightarrow J/\psi+\gamma$, it is necessary that both the dimuon pair and primary photon be within the acceptance of the detector. Once the J/ψ from a χ_C is accepted in the muon spectrometer there is about a 70% chance of the primary photon ending up in the acceptance of the NCC. We have a further photon reconstruction efficiency of around 80% for the low typically 1 GeV photons expected from a χ_C. We apply several cuts to the photons before constructing an invariant mass. To select electromagnetic showers a χ^2 <10 cut was applied where χ^2 is a sum of the longitudinal and transverse χ^2 as measured by the pads. No strip information was used. The photons were required to have an E_γ >500 MeV to suppress the background from low energy showers due to MIPS etc. An minimum angle cut between each muon and the photon was necessary due to the clustering algorithms used. Photons very nearly collinear with the muons are lost, because the muon track absorbed the photon in the clustering algorithm. This effect, which is not present in mixed events, leads to a dip in the distribution immediately below the χ_C after background subtraction. The combinatorial backgrounds shape is found by utilizing mixed event background subtraction in which we take a J/ψ's from the current event and pair it with NCC tracks from previous events. The mixed events were normalized to a region above 800 MeV, or about 3 σ above the χ_C peak.

In addition we account for a dimuon background under the J/ψ peak where we assume an improvement of 2.5 in S/B for the J/ψ as compared to previously measured PHENIX data by using the FVTX which allows us to reject hadron decays giving background muons, and improve the J/ψ mass resolution.

We follow the standard practice of looking at the difference between the $J/\psi+\gamma$ invariant mass and the J/ψ mass, since this eliminates much of the resolution smearing of from the muon measurement. The width of our signal is then dominated by the energy resolution of the photons. Fig. 3.14 shows the foreground and mixed background overlayed along with the resulting subtracted invariant mass distributions for pt=7,8,9 GeV, in pp, dAu-minbias, dAu-central 0-20%, and AuAu 40-50% central collisions.

3.4.1 χ_C R AA

These yields were then renormalized to a P_T and y spectrum from pythia assuming binary scaling, together with the suppression factors measured in the PHENIX detector for the J/ψ. The yields were then scaled to the luminosities of RHIC II.

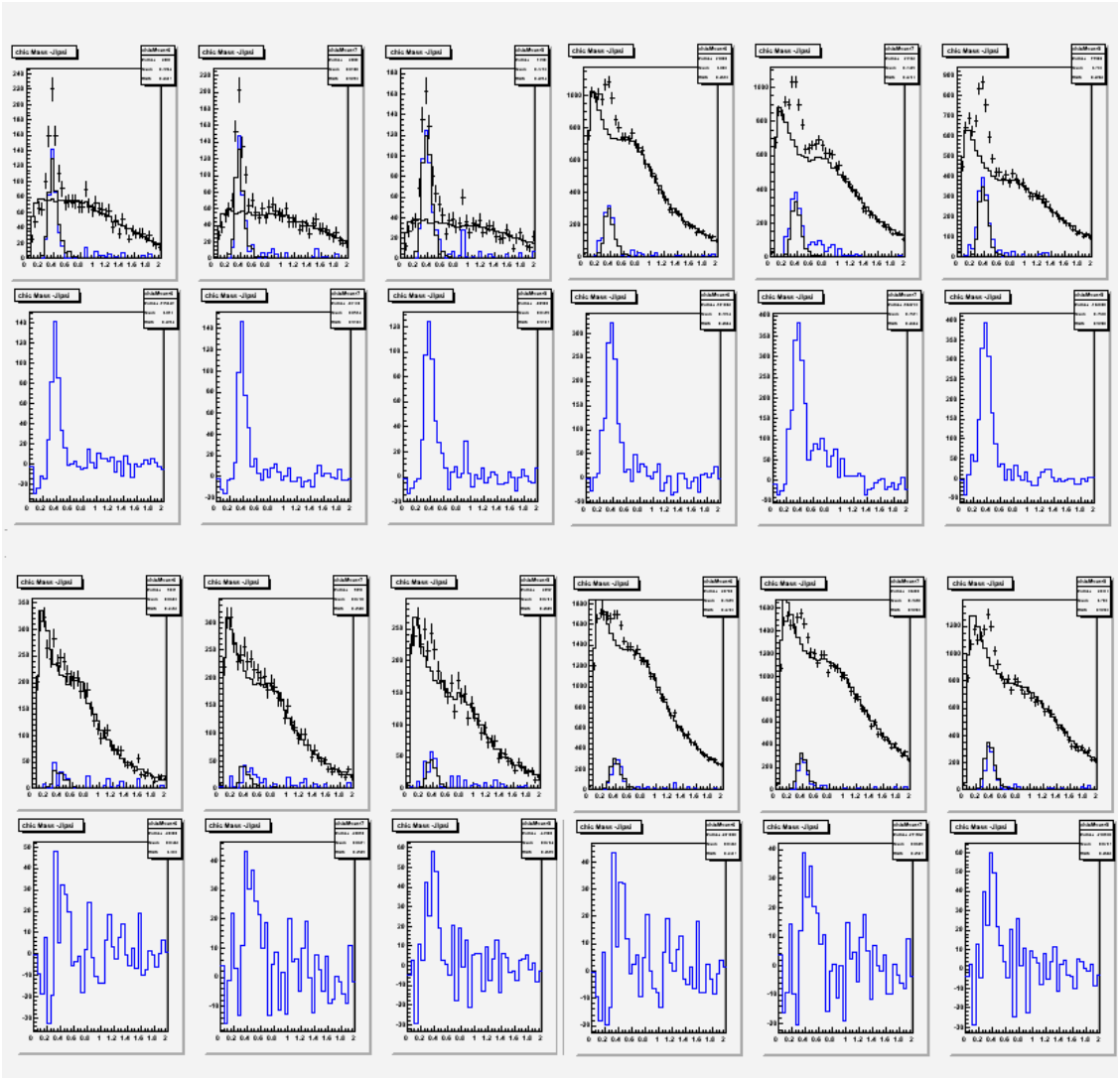

Figure 3.14: χ_C peaks

We have set to zero points, in which a measurement cannot be made because of overwhelming backgrounds, however we have set the statistical error bars from the level of the background.

Fig. 3.16 shows accuracy with which we can measure N_{part} dependence of R_{AA}. The suppression pattern assumed is identical to that of the current measurement of the suppression of the J/ψ as measured in the muons arms. Also shown is a comparison to a model explained later, which includes the additional suppression expected for the χ_C because of its lower binding energy and a factor for the regeneration of the χ_C from the coalecence of charmed quarks.

Fig. 3.15 shows R_{AA} as a function of p_T. The p_T dependence is important to discriminate between models since lower p_T states would tend to experience the medium differently and show a different magnitude from effects such as dissociation, screening, and coalescence.

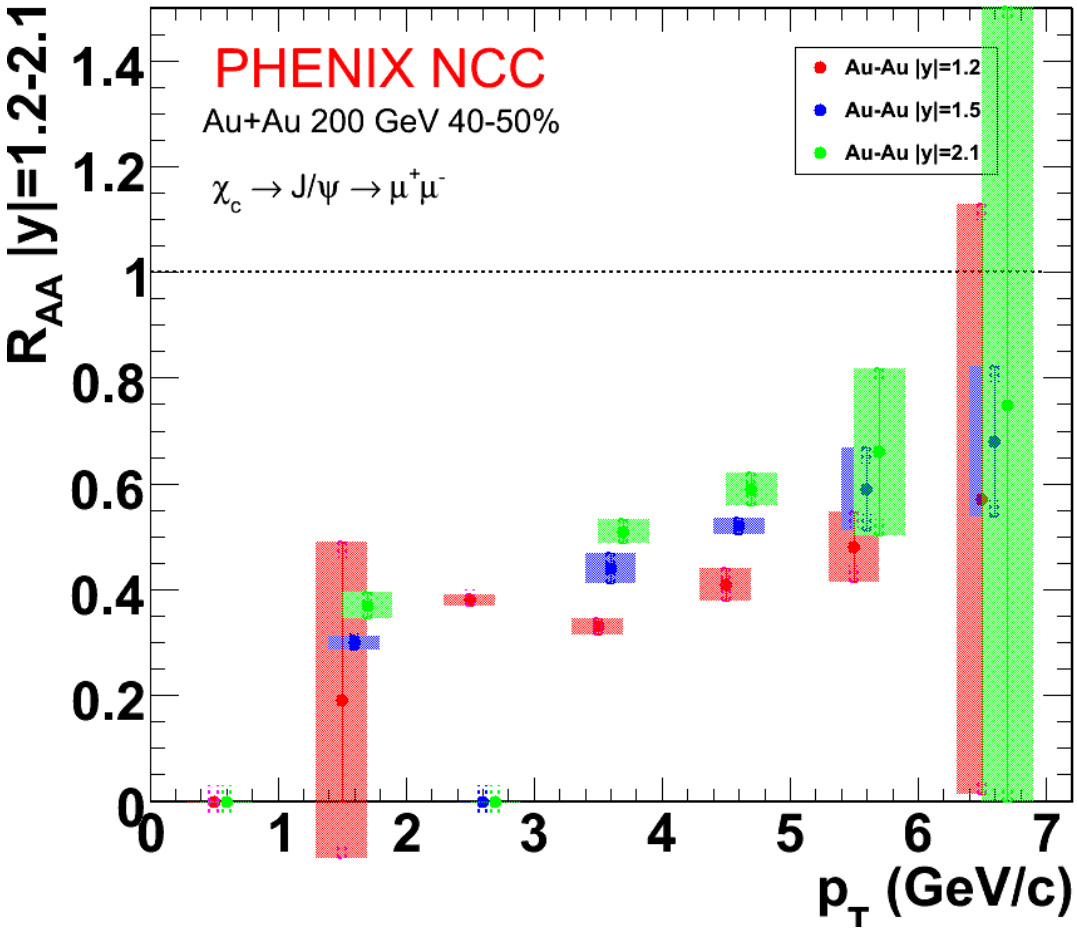

Figure 3.15: Raa χ_C

This accuracy with which we can measure R_{AA} can then be compared to models. As remarked earlier, about 40%

These models are somewhat generic in that the are all trying to put limits on 1) screening, 2) dissociation, and 3) coalesce. The suppression of charmonium, which originally was the supposed to be a clear indication of deconfinement, presents a puzzle to people within the heavy ion community. Prior to the publication of the data from PHENIX pne of the main expectaions what that the J/ψ would be completely suppressed in AuAu collisions at RHIC due to the higher energy densities available. However the suppression pattern seen at RHIC appears to be simillar to that as seen at CERN. The coalecence of charmed mesons was invokes as a mechanism to explain this seeming discrepancy.

Results in the last few years from the lattice community inidicate the Jψ remains intact above the critical temperature, while the χ_C and ψ' should dissociate at a temperature near T_C One simple explanation to explain the RHIC results would be that since some 60% (check this number) of J/ψ come from the decay of the χ_C, that all χ_c's are melted both at CERN and at RHIC, and that the melting point of the J/ψ is higher than is reached at

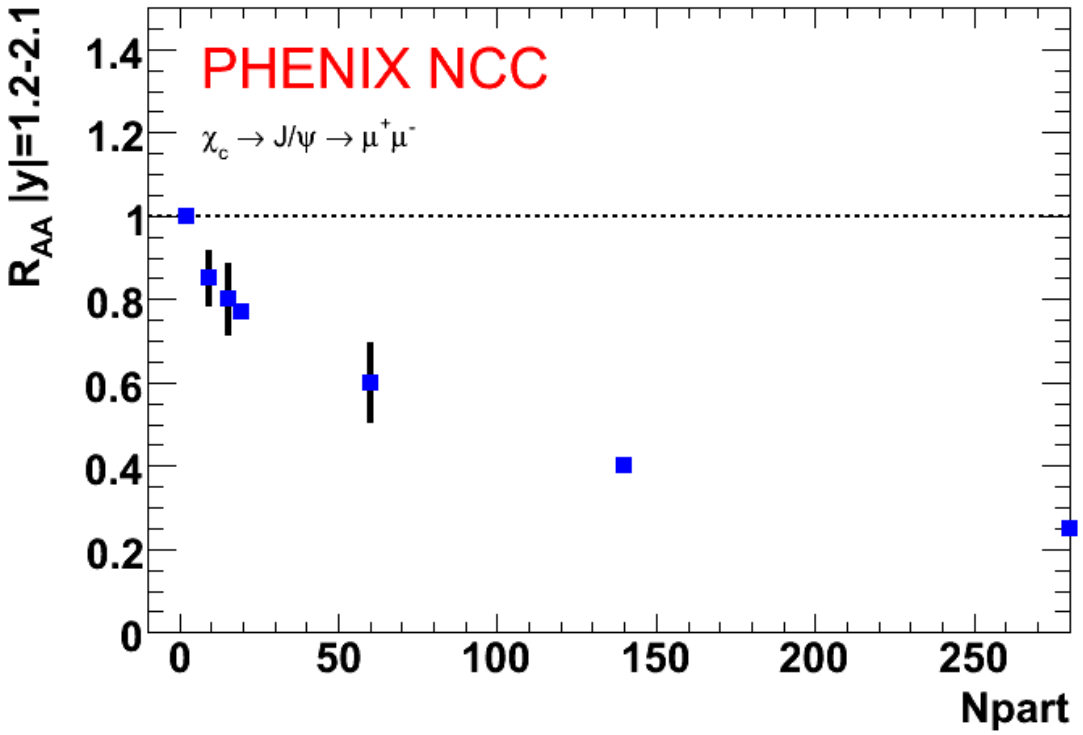

Figure 3.16: Raa χ_C vs npart

RHIC. The mechanism of breakup from hard gluons must be at some level active in heavy ion collisions (ref.) In addition regeneration also may come into effect, particularly if charm is significantly enhanced (ref Thews). It becomes critical then to actually measure, not only the J/ψ but also other particles with different screening lengths (aka melting temperatures) - in particular the χ_C since it is responsible for a large fraction of the J/ψ's seen.

The first question which one would immediately ask is whether J/*psi* suppression was entirely due to the suppression of the χ_C. In this case one would expect the χ_C to be seen at it normal level with respect the J/ψ in pp, dAu, and peripheral AuAu collisions, then to be rapidly suppressed as a function of N_{Part} until energy densities comparable to central PbPb collisions CERN were reached at RHIC.

The magnitude of χ_C suppression varies amongst models. We compare the measurements which the NCC can make vs one model from Rapp. See Fig. 3.17. The predictions of this model are shown compared to the error bars expected in the data if the suppression of the χ_C was identical to that of the Jψ in Fig. 3.16 . While we do not believe that the models are accurate enough for us discriminate between a coalescence or non-coalescence scenario by simply making a measurement of the suppression vs N_{part}, a measurement comparing the yield of χ_C vs J/ψ as a function of N_{part} and pt should allow us to make constrain the various possible scenarios.

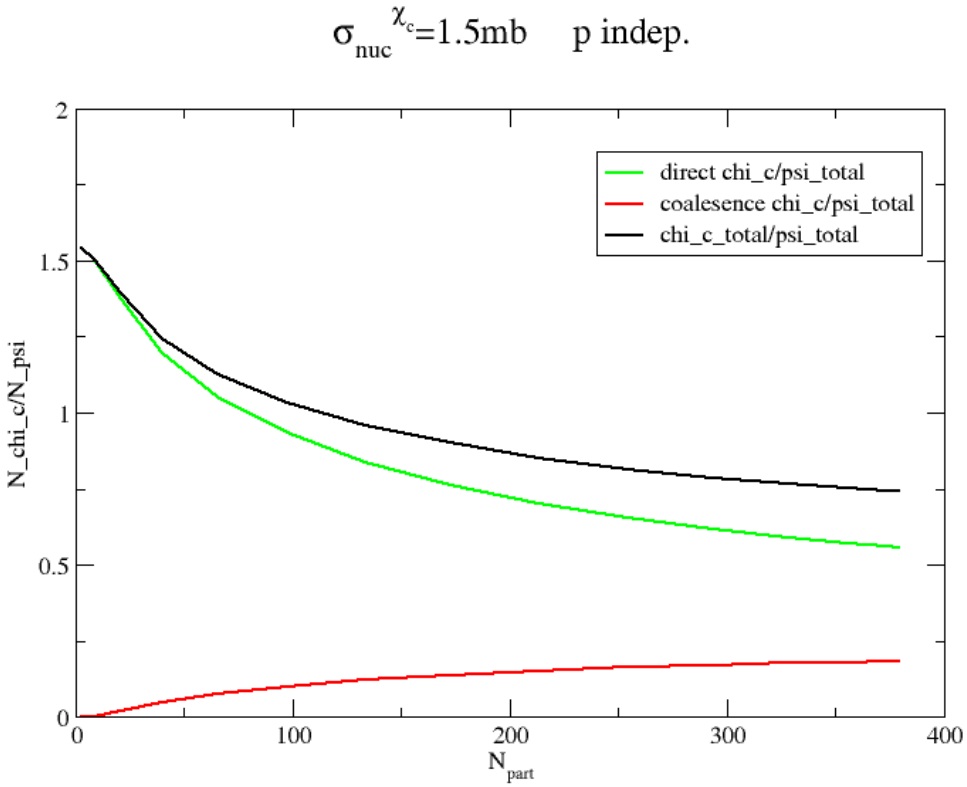

Figure 3.17: Rapp χ_C/Jpsi yield prediction

Chapter 4

Summary

We have presented in this report our simulated performance for the NCC. In particular we have shown the performance of the NCC as a non-projective tracking calorimeter. Efficiencies for finding and identifying electromagnetic showers, while not independent of angle, momentum, or multiplicity, is reasonably uniform, and well within the standard correction methods used in PHENIX. We have established that the detector performs well in p+p to Au+Au collisions and is capable of providing high quality photon measurements over a very broad range. In particular π^0 R_{AA} measurements will be possible at all centralities allowing us to distinguish between mechanisms of suppression and energy loss. From the measurements of the π^0 we are able to then make measurements of direct photons and hence this paves the way for photon-Jet measurements in conjunction with other detectors. The measurement of the χ_C is made possible for the study of charmonium suppression for the first time. We also note, that this is perhaps the only possibility for the measurement of the χ_C in heavy ion collisions and the critical new information it brings to questions of deconfinement at any machine for the foreseeable future. Finally the NCC will allow us to measure the proton spin contribution of the gluon at low-x thereby finalizing the question of whether the gluon contributes a significant amount to the gluons spin. The NCC will extend the capabilities of the PHENIX detector significantly, by extending the acceptance of electromagnetic calorimetry to higher rapidity, opening up the horizons of rare physics - such as direct photons, gamma jets, and the chic at reasonable event rates.

Appendix A

pQCD NLO Global Analysis at RHIC

To determine polarized parton distributions (PDFs), in particular, the gluon and anti-quark distributions, employing polarized proton collisions at high energy, is the most important goal of the RHIC spin program. The spin dependent inelastic p-p scattering cross sections factorize into products of polarized parton distribution functions of protons and hard scattering cross sections describing spin dependent interactions of partons. The latter are calculable in QCD perturbation theory at next-to-leading (NLO). Knowing higher order corrections in perturbative expansion of partonic cross sections is generally very important because in hadronic scattering they can be often sizable, and because they also reduce the dependence of cross section on the choice of various unknown scales in the theory such as factorization, renormalization (scales). For most reactions relevant to the RHIC spin program NLO corrections to the cross sections are available, as such the foundation for determination of the polarized parton distribution at NLO already exists.

A complication common to A_{LL} probes of parton distributions in hadronic scattering is how to extract information about polarized PDFs in general from experimental data. We measure double spin asymmetries as functions of transverse momentum p_T of the measured final state particle, while the PDFs relevant to solving the nucleon spin puzzle need these to be in terms of partonic momentum fractions, x. For any measured data point in p_T, the gluon polarization is probed in a wide range in x_g, due to the convolutions inherent to the theoretical description of hard scattering cross sections. Therefore measured A_{LL} point vs. p_T has significant overlap with its neighbors in x_g. It is straightforward to use a model for $\Delta g(x_g)$ to predict $A_{LL}(p_T)$. However one cannot directly go the other way, i.e. to map points in pT onto gluon polarization values vs. x_g. We emphasize two points here:

1. This is *not* unique to hadronic processes alone, semi-inclusive DIS measurements (high p_T di-hadron final state measurements in l-h scattering, for example) face the same issue.

2. It is often argued that measurement of final state correlations, (by going beyond inclusive measurements, such as p-p $\rightarrow \gamma$-Jet, Jet-Jet), to determine the kinematics event by event, will solve this problem. This is *only* true if the parton distributions are being extracted at *leading order*, which should only be a first step towards determining the parton distributions, *not the ultimate goal*.

The ultimate goal of the RHIC spin program is to determine the polarized PDFs at highest order possible (presently NLO) in perturbative QCD using all RHIC spin data. This can best be achieved by analyzing the RHIC spin data and the polarized fixed target DIS data in a framework of a *global analysis*, similar to one that already exists in the form of CTEQ parton distribution functions for the unpolarized PDFs. The important advantage of such a global analysis is that it takes the measured experimental variables directly, rather than attempting to use derived or unmeasured variables in hadronic scattering such as x. Secondly, the uncertainties in the PDFs can be evaluated systematically taking in to account theoretical as well as experimental systematic uncertainties and their correlations. In order to do this over the widest possible kinematic range in x_g, in particular for the polarized gluon distribution, RHIC will have to be operated at different center of masses, both higher and lower than 200 GeV at which most of the operations have occurred so far. While this discussion is (apparently) only focused on the polarized gluon distribution, that was only for brevity. The situation, apart from the aspect of different center of mass operations, is identical in the case of determination of quark-anti-quark distributions with W physics measurements at RHIC. An effort to realize such a global analysis is now underway. In the next few years when the data from high luminosity, polarization and the detector upgrades for RHIC and the experiments get ready, so will be the analysis framework for the polarized PDFs. These together will enable the best possible extraction of polarized parton distribution functions.

Appendix B

Details on Calibrations and Reconstruction Efficiency

Large phase space coverage of the NCC together with its lateral and longitudinal segmentation necessitates rapidity and energy dependent calibrations of sampling fractions, energy deposits and shower shapes used to reconstructs shower energies and to identify particles responsible for a shower. This section describes how these callibrations are performed.

The NCC is designed to measure electromagnetic showers, primarily photons, direct or a meson (mostly π^0) decay products. The calibrations described in this section correspond to electromagnetic showers. Calibration for hadrons and jets can be done following the same recipe.

B.0.2 Sampling fractions

Energy deposits in the tungsten radiator are sampled by pads comprising silicon sensors. Consecutive pads in an NCC segment are connected to form a tower. The energy collected by the silicon pads is only a fraction of the energy deposited in the corresponding calorimeter volume, since most of the energy is deposited in the passive radiator.

The sampling fraction, the ratio of the detected energy to the total energy, depends on the shower composition, which varies with the depth and the shower energy. Moreover from nearly perpendicular impact at high rapidity to a rapidity of about one, the length of the pad traversed by the shower increases by roughly 1.4, changing the sampling fraction. The sampling fraction therefore depends on the NCC segment, the shower energy and the incident angle of the shower on the detector. The sampling fraction was also depends on energies of tracking cutoffs in the GEANT simulation.

The sampling fractions for the three NCC segments are shown in Fig B.1a for the EM1, Fig B.1b for the EM2, and Fig B.1c for the HAD segment, as a function of η and energy of the shower.

The sampling fractions are used iteratively in the track reconstruction algorithm as a look-up table with fast bilinear interpolation.

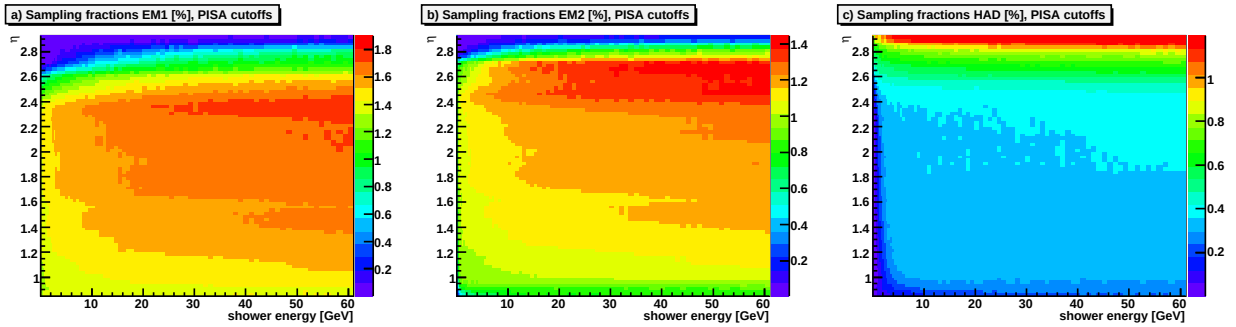

Figure B.1: Sampling fractions for a) EM1, b) EM2, c) HAD segment as a function of shower energy and angle

B.1 Energy calibration

After the tracks are formed, the final stage energy correction is applied. This accounts for leakage at the calorimeter edges, nonlinearity at low energies, and calibration of the reconstruction losses. The energy calibration factors are shown in Fig B.2 as a function of η and energy of the reconstructed track.

B.2 Identification of electromagnetic showers

High granularity in transversal dimension and longitudinal segmentation of the calorimeter allows for identification of electromagnetic showers using χ^2 fits to a shower shape.

Longitudinal χ^2 is calculated using the distribution of the energy deposited in each NCC segment, and the corresponding σ. These distributions are established using a single photon simulation and interpolated. The longitudinal electromagnetic χ^2 corresponding to a track is given by:

$$\chi^2_{EM,Long}(E^{meas},\eta) = \sum_{seg=EM1,EM2,HAD} \left(\frac{E^{pred}_{seg} - E^{meas}_{seg}}{\sigma^{E,pred}_{seg}} \right)^2 \tag{B.1}$$

where E^{meas} and η are the energy and rapidity of a track, seg is one of the three NCC segments, E^{meas}_{seg} is the measured energy in a segment, E^{pred}_{seg} is the predicted energy measured in the segment, and $\sigma^{E,pred}_{seg}$ is the corresponding variance. The predicted distributions are shown in Fig B.3.

Similarly a lateral χ^2 can be established using transversal widths W_{seg} of showers in the segments:

$$\chi^2_{EM,Trans}(E^{meas},\eta) = \sum_{seg=EM1,EM2,HAD} \left(\frac{W^{pred}_{seg} - W^{meas}_{seg}}{\sigma^{W,pred}_{seg}} \right)^2 \tag{B.2}$$

The stripixel layers contain information about the early stage of an electromagnetic shower development and therefore can be used as another cut to reduce single track π^0

contamination. It is calculated analogously to the one above:

$$\chi^2_{EM,TransSP}(E^{meas},\eta) = \sum_{SPlayer=1,2} \left(\frac{W^{pred}_{SPlayer} - W^{meas}_{SPlayer}}{\sigma^{W,pred}_{SPlayer}} \right)^2 \quad \text{(B.3)}$$

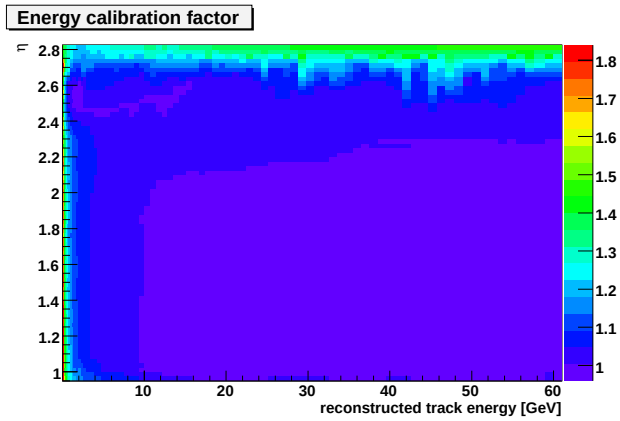

Figure B.2: Energy calibration for electromagnetic showers as a function of shower energy and angle

B.3 Reconstruction Efficiency

As mentioned previously, the NCC is designed to be a tracking detector, and hence projective geometry is not required. Whether showers enter the detector at right angles to the front face or at an angle, the NCC is capable of reconstructing the shower. Figure B.4 shows the efficiency of the calorimeter in reconstructing photons in p+p collisions with energy up to 40 GeV at various angles in the detector from a y=0.9, where the calorimeter begins, and where the shower is at a 45° angle, up to y=2.7. At a rapidity of about 2.5 the showers begin to hit the side of the NCC. At present our reconstruction software does not handle this case and while the shower is found, the energy is not measured correctly because of the shorter effective depth of the detector. One can see that between rapidities of 0.9 to about 2.5 the efficiency remains good. Figure **??** shows the efficiency in central Au+Au collisions and one sees that the the efficiency had dropped to ?????, however it remains relatively constant at all angles. The major effect in central Au+Au collisions is occupancy, and lower energy showers will be overwhelmed by the background at higher rapidities and hadrons will be misidentified as electromagnetic showers (Fig. **??**).

B.4 Occupancy of the NCC detector in p+p and Au+Au interactions

Hit tower occupancy in the NCC detector varies strongly with number of interacting hadrons. At lower multiplicities in p+p and d+Au collisions the occupancy is at a few percent level,

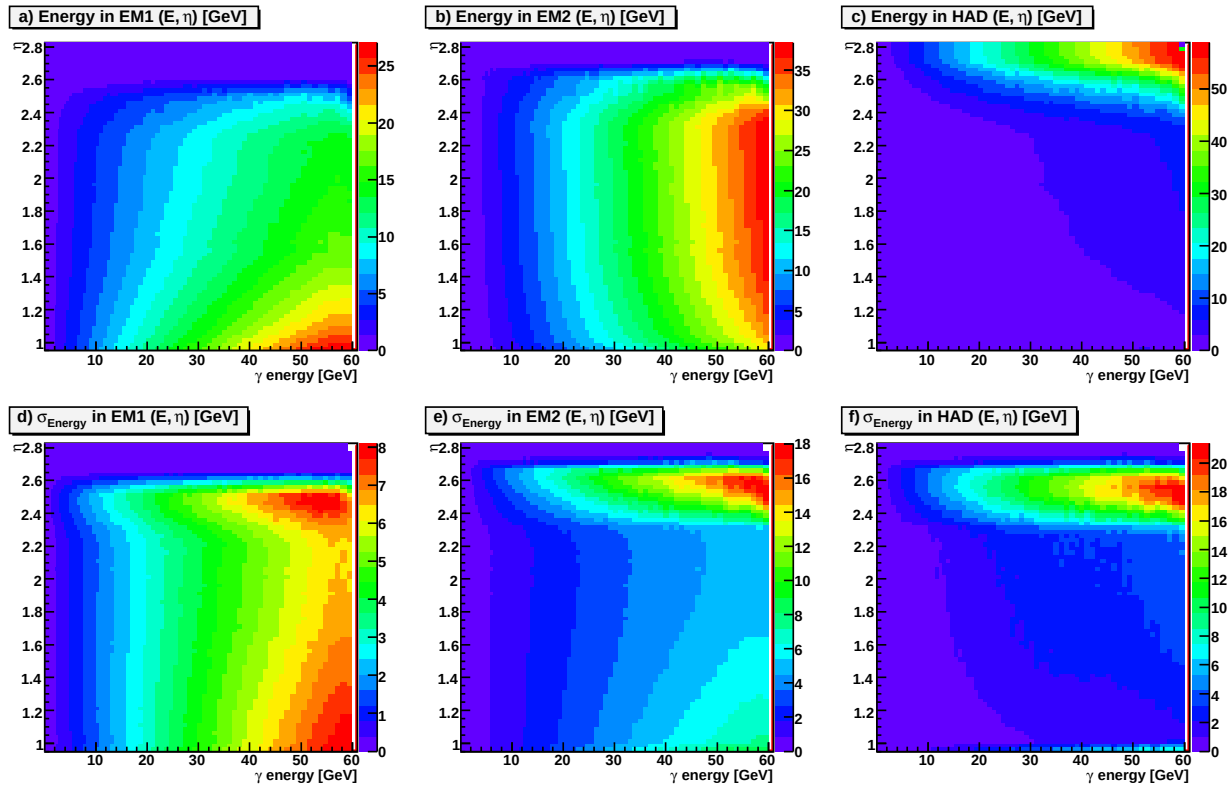

Figure B.3: Energy deposits in a) EM1, b) EM2, c) HAD segment and their respective variations as a function of gamma energy and angle. These distributions are used to parametrize $\chi^2_{EM,Long}$, see equation B.1

rising up to nearly full occupancy in the most central Au+Au interactions (see Fig. above). Typical occupancies in EM1 segment together with angular dependence of the occupancy are shown in the following figures.

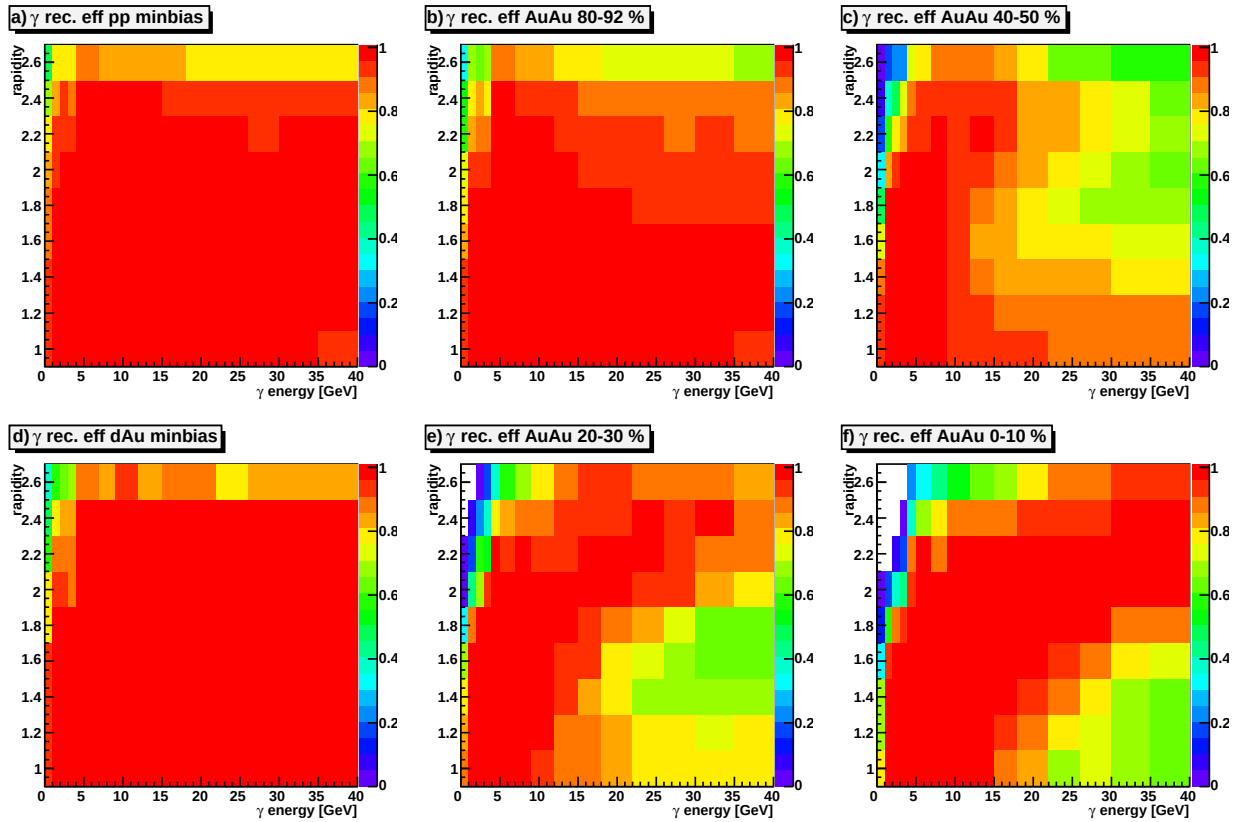

Figure B.4: Reconstruction efficiencies for single γ as a function of energy and η for a) p+p minimum bias, d) d+Au minimum bias, b) Au+Au centrality 80–92 %, c) Au+Au centrality 40–50 %, e) Au+Au centrality 20–30 %, f) Au+Au centrality 0–10 %, see the text.

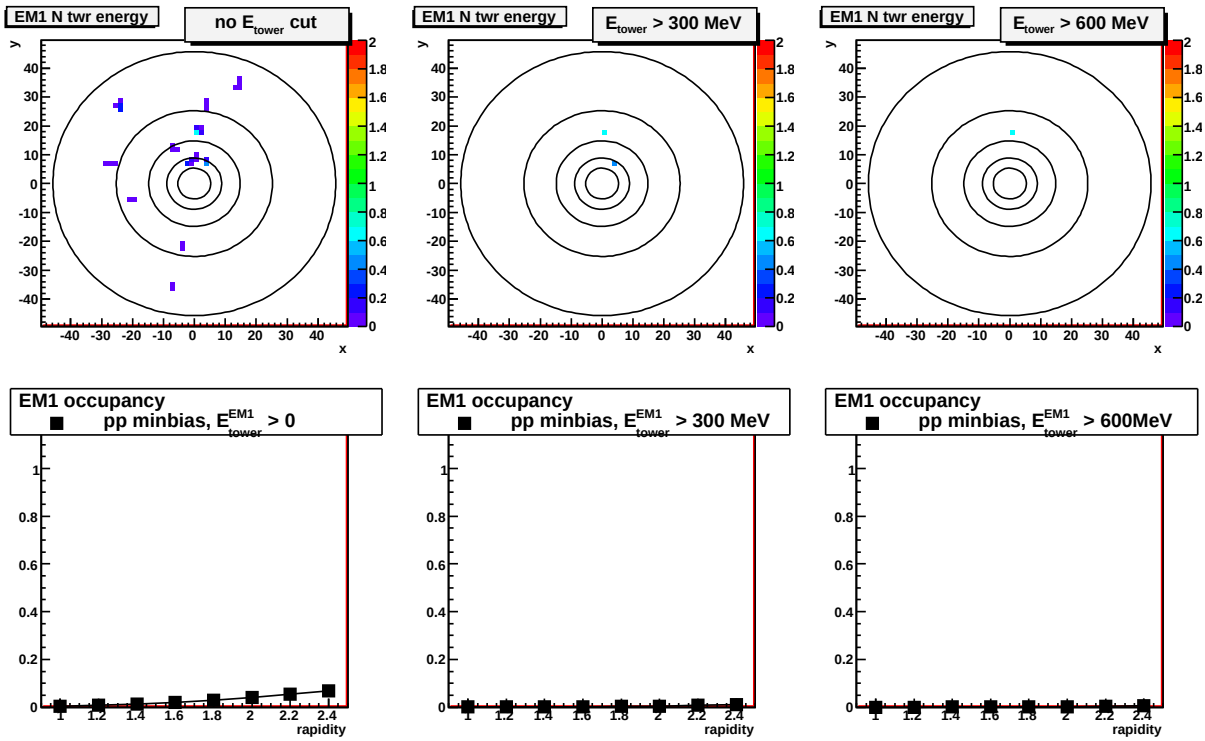

Figure B.5: Upper row: energy [GeV] deposited in the sub-towers of the NCC EM1 section for a p+p minimum bias event, with no threshold (left), 300 and 600 MeV thresholds (middle and right). Colors indicate the total energy deposited in each sub-tower. MIP energy is about 200 MeV. The circles on the plot indicate pseudorapidity in steps of 0.5 with the outermost solid circle showing $\eta = 1$, the next dotted line indicating $\eta = 1.5$ etc. to $\eta = 3$ for the smallest circle. The bottom plots show the occupancy as a function of pseudorapidity for no cut on tower energy (left) ,a 300 MeV cut on the tower energy (middle) and a 600 MeV cut (right).

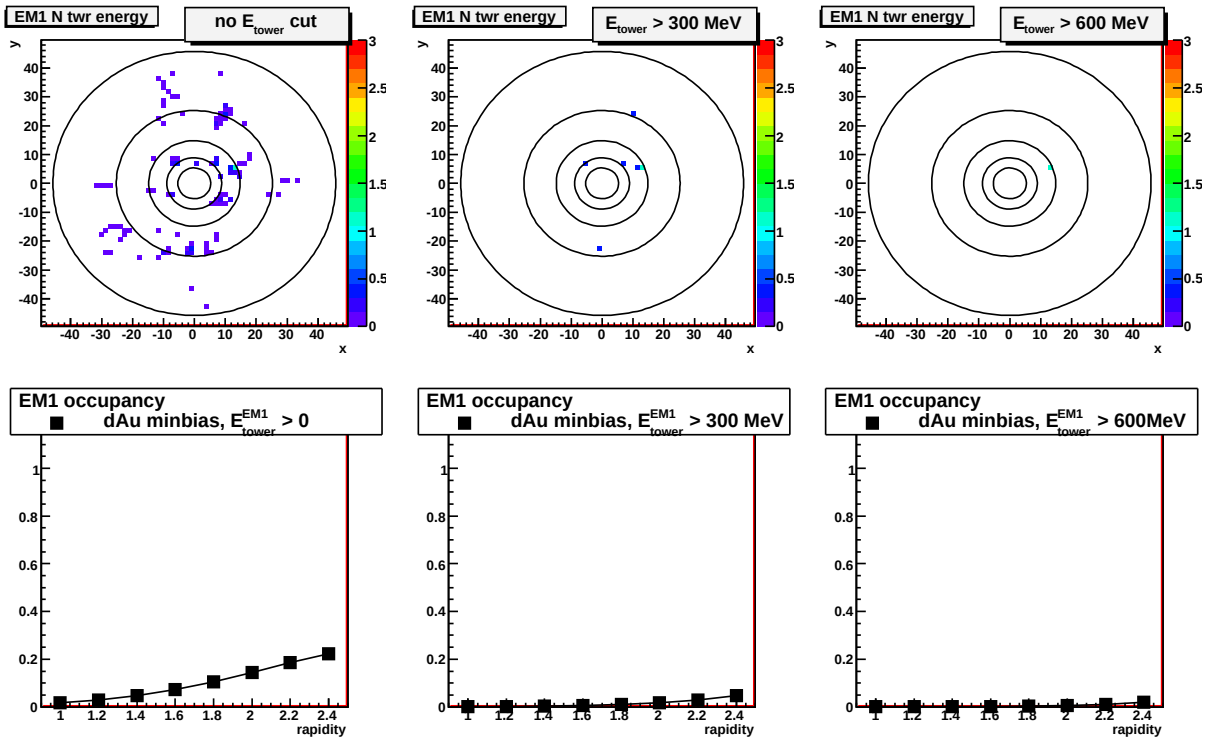

Figure B.6: Upper row: energy [GeV] deposited in the sub-towers of the NCC EM1 section for a d+Au minimum bias event, with no threshold (left), 300 and 600 MeV thresholds (middle and right). The bottom plots show the occupancy as a function of pseudorapidity for no cut on tower energy (left) ,a 300 MeV cut on the tower energy (middle) and a 600 MeV cut (right).

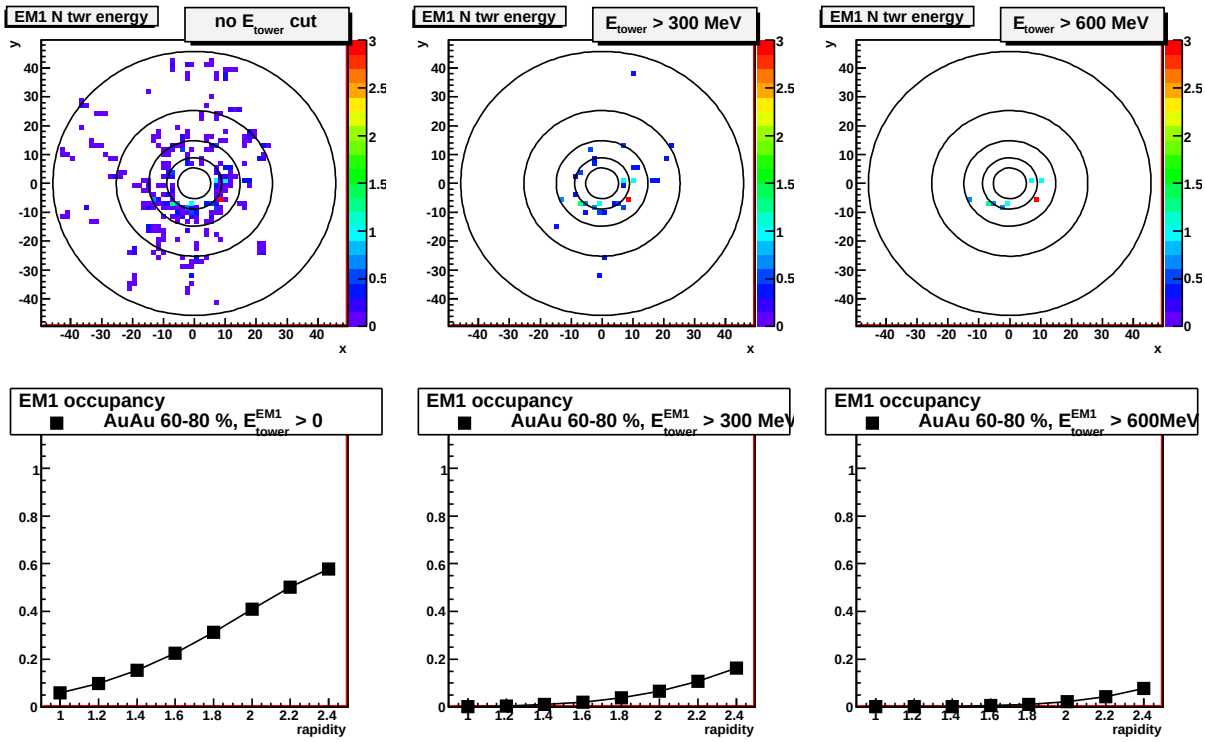

Figure B.7: Upper row: energy [GeV] deposited in the sub-towers of the NCC EM1 section for a Au+Au 60–80 % central event, with no threshold (left), 300 and 600 MeV thresholds (middle and right). The bottom plots show the occupancy as a function of pseudorapidity for no cut on tower energy (left) ,a 300 MeV cut on the tower energy (middle) and a 600 MeV cut (right).

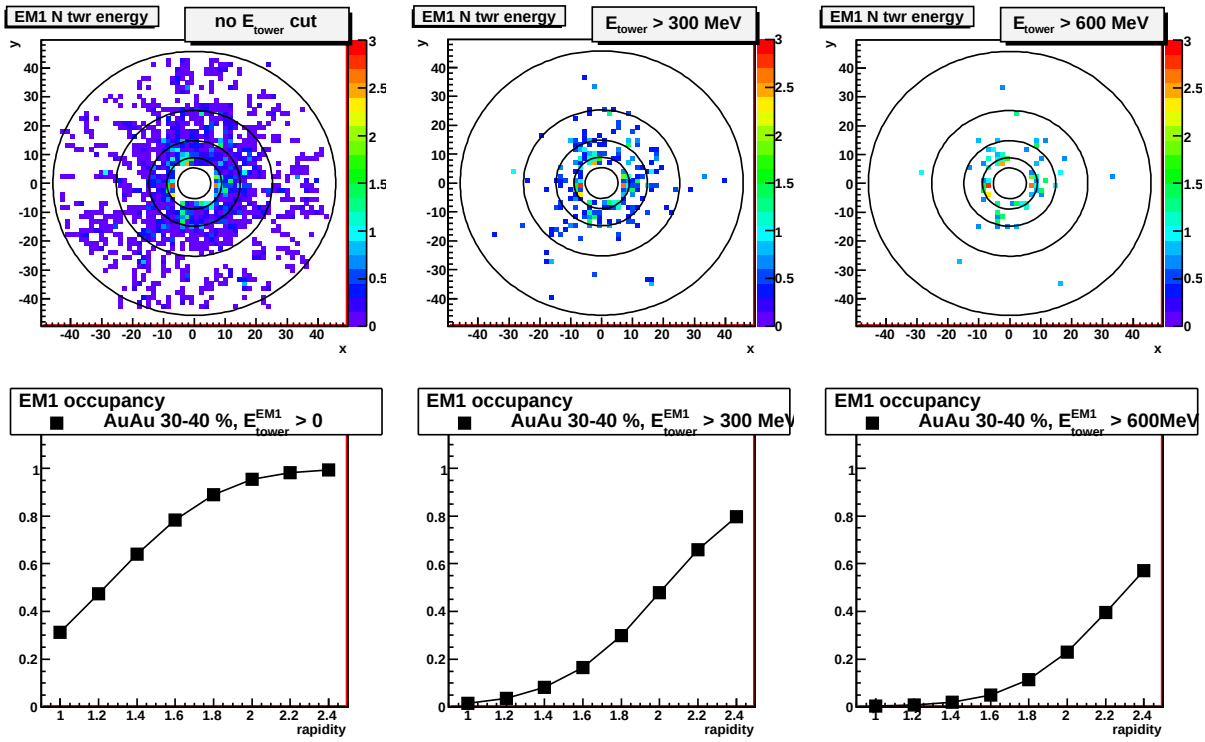

Figure B.8: Upper row: energy [GeV] deposited in the sub-towers of the NCC EM1 section for a Au+Au 30–40 % central event, with no threshold (left), 300 and 600 MeV thresholds (middle and right). The bottom plots show the occupancy as a function of pseudorapidity for no cut on tower energy (left) ,a 300 MeV cut on the tower energy (middle) and a 600 MeV cut (right).

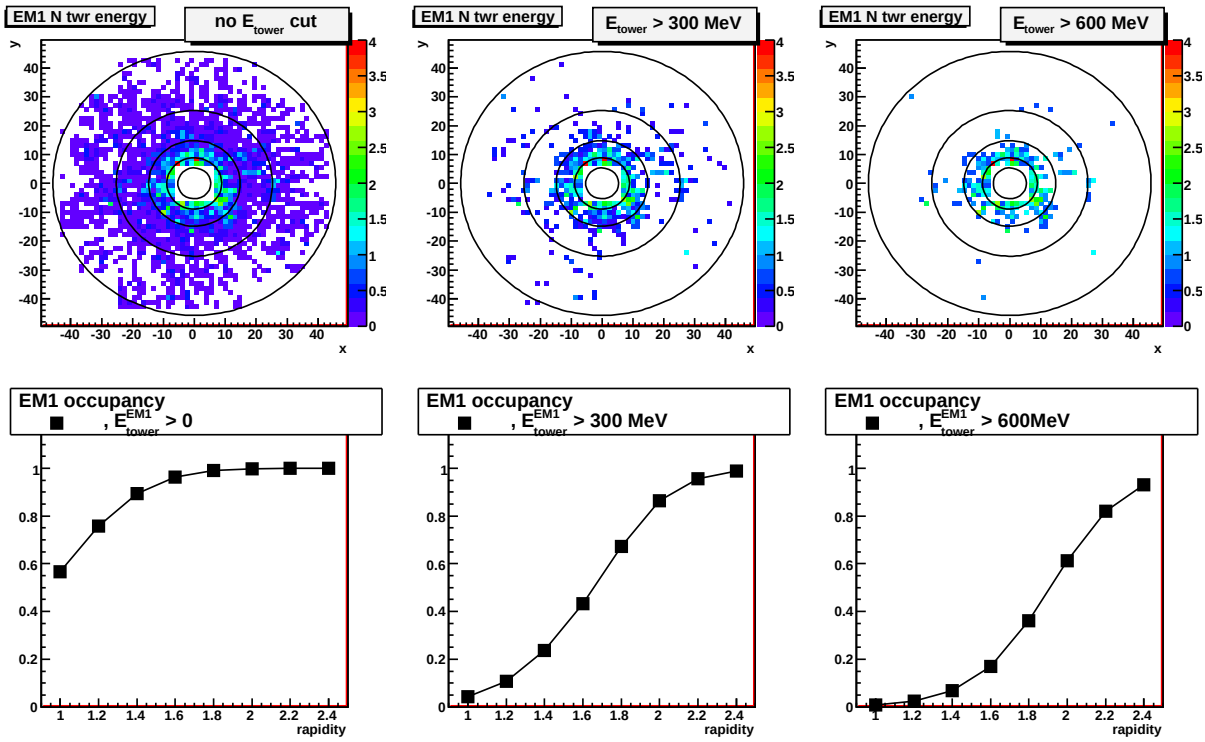

Figure B.9: Upper row: energy [GeV] deposited in the sub-towers of the NCC EM1 section for a Au+Au 10–20 % central event, with no threshold (left), 300 and 600 MeV thresholds (middle and right). The bottom plots show the occupancy as a function of pseudorapidity for no cut on tower energy (left) ,a 300 MeV cut on the tower energy (middle) and a 600 MeV cut (right).

Appendix C

Status of digitization tests

C.0.1 Energy measurements in the NCC operated in a fully digital mode

The NCC is longitudinally segmented into two fine and one coarse tower-structured segments. The total number of Si pads in the calorimeter is 60,000. A compact, economical readout design was proposed and recently tested in a test beam at CERN (Fig. C.1).

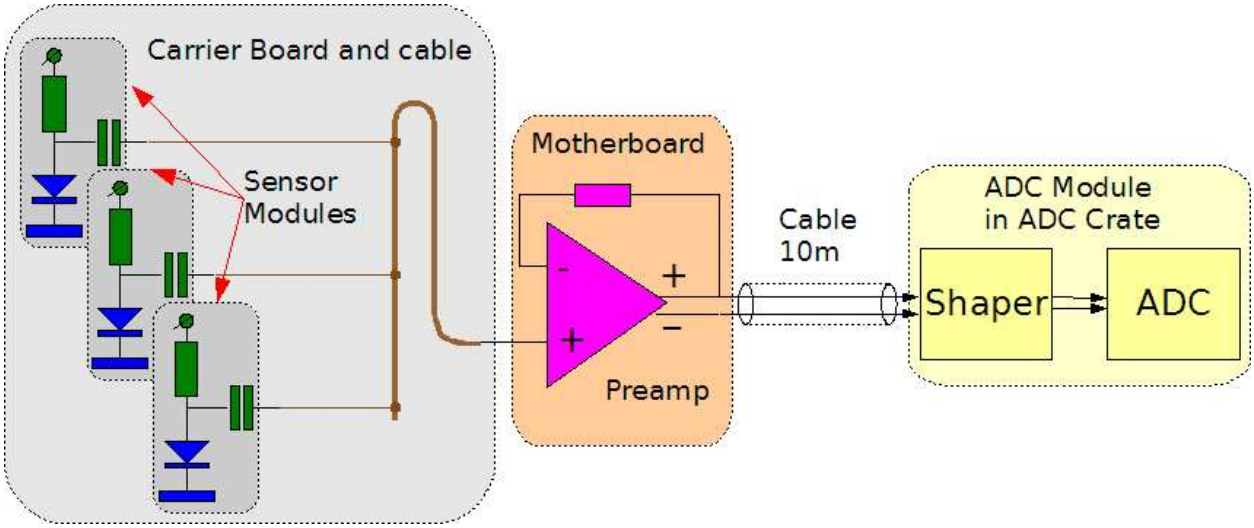

Figure C.1: Signal processing block-diagram for NCC towers

Signals from geometrically matching silicon pads were first grouped together to create calorimeter towers. Signals from geometrically matching sensor pads on individual carrier boards are carried over the traces to the outside edge of the detector (r ˜ 50 cm), summed using traces on a flexible backplane which is implemented as a stiffened part of the flexible cable further connected to mother board with preamplifiers. The maximum number of signals in analog sums is seven and each motherboard carries up to 112 channels of preamplifiers. A shielded differential cable (Hard Metrix) is used to deliver differential signals from detector to the shapers preceding fast ADC's.

The signal amplitude at the input of the shaper is proportional to the current pulse at the sensor. Since we measure the charge deposited in the sensor, the output signal of the channel should represent the integral of the current pulse.

Details of the signal processing chain for NCC towers were simulated using a full component model built within the LT SPICE electronics simulation framework. Shapes of the signal from NCC pads as seen on the input to preamplifier and to ADC (after 4_{th} order Bessel filter with cutoff frequency of 2.5 MHz) simulated with LT SPICE are shown in the next figure (Fig. C.2).

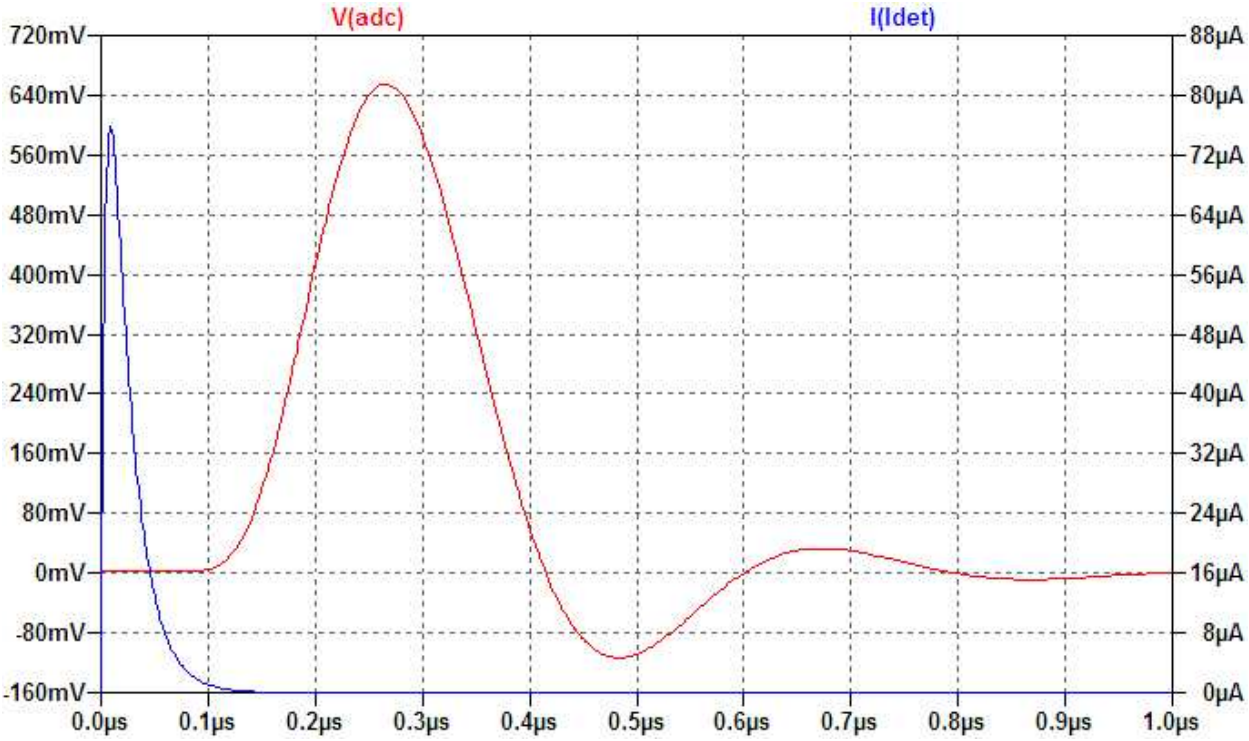

Figure C.2: LTSPICE simulation of the readout chain for NCC pad sensors. Detector signal (blue) and the output of the filter (red) are shown.

Simulation predictions and different digitization and processing algorithms were tested with NCC prototype in the Autumn of 2007 in the test beam at CERN (Fig. C.3).

In the test beam experiment where we had only limited control over the beam intensity. Therefore, we used modified preamplifiers with higher cutoff filter frequency of ˜10 MHz. Fast 12-bit ADC's with a sampling frequency of 60 MHz developed at NEVIS for the PHENIX HBD project (maximum of 28 stored samples per triggered event) were used to digitize the data. A superposition of multiple pulses (electrons in one of the NCC prototype segments) is shown in the Fig. C.4 below.

Events were selected with approximately matching amplitudes (that explains the grouping of signals in three bands seen in this figure). All events were time-adjusted subtracting trigger timing phase measured through one of the spare preamp-ADC channels (timing resolution from pulse shape measurements ˜50 ps). A typical pulse length was ˜100 ns followed

Figure C.3: Prototype 2x2 NCC calorimeter in the test beam at CERN (September 2007).

by slight overshoot and complete base restoration in ˜300 ns. For the purposes of this study all 28 samples from the buffer were recorded and later processed through different digital integration algorithms. Details of this study will be published elsewhere. As an illustration to this note we include below a picture (Fig. C.5) explaining the choice of the window size for the simple moving average algorithm. Sample 1 in this picture corresponds to the start of a signal. It takes 12 samples (˜200 ns integration window) to saturate the resolution which happens to be ˜30% better than for measurements limited to signal peak region (samples 4 and 5).

Using a slightly more complicated sliding window algorithm to integrate the input signal, further improves the signal/noise ratio by approximately a factor of 1.3 resulting in the value of ENOB (effective number of bits) being increased from 11.6 (typical value for commercial ADC's with full scale range of 12 bits or higher) to about 13 bits (for 80 Mhz sampling).

Based upon simulations, the NCC energy dynamic range (single tower in EM segments) is set to 50 GeV. With a noise free bit range of 13 bits it corresponds to the least count of 5 MeV. As we have seen in the earlier section, on average $\sim$ 30 towers will contribute energy to an individual track, resulting in a noise contribution of the order of 25 MeV which is still negligible when compared to the expected 1% constant term in energy resolution

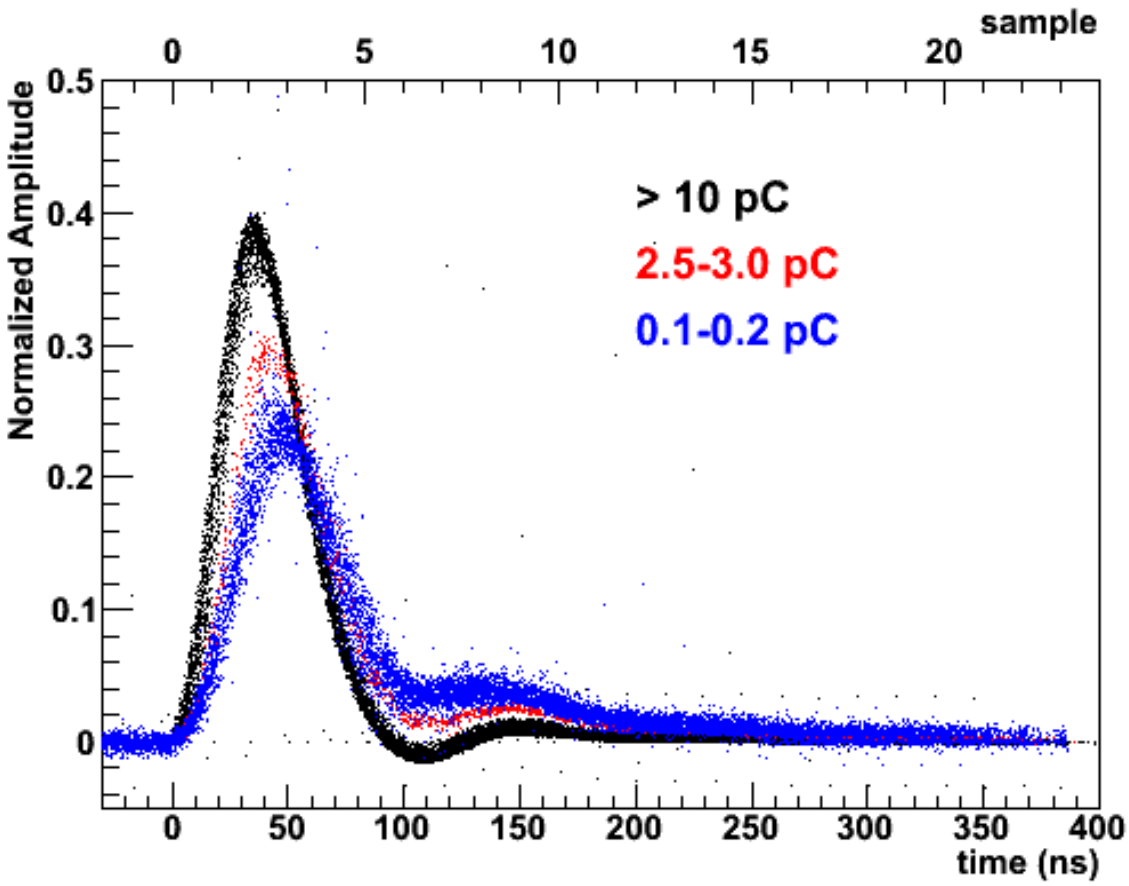

Figure C.4: Superposition of multiple NCC signals (electron test beam, CERN 2007).

of NCC. Another way to evaluate this number is to compare it to the signal of a MIP in a single segment (15 MeV compared to $\sim$ 200 MeV) or the whole calorimeter (25 MeV compared to $\sim$ 600 MeV). A clear MIP signal in the NCC is a very important aspect of the future PHENIX W identification program and we are confident that detector and readout as designed are perfectly matching the program requirements.

C.0.2 Shower shape measurements in NCC 2-D precision coordinate layers

Details of the position sensitive layer design were fully explained in the TDR. Here we will briefly review the progress made in further hardware and firmware development work aimed to test the functionality of that design and to build the test bench which would allow detailed studies of the different prototype position sensitive silicon detectors without building a full-fledged silicon detector laboratory.

In our original proposal we considered two different strip sensor designs: classical with parallel strips of $0.5 \times 62\,\mathrm{mm}^2$ on a 300 μm thick Si and stripixels with similar effective

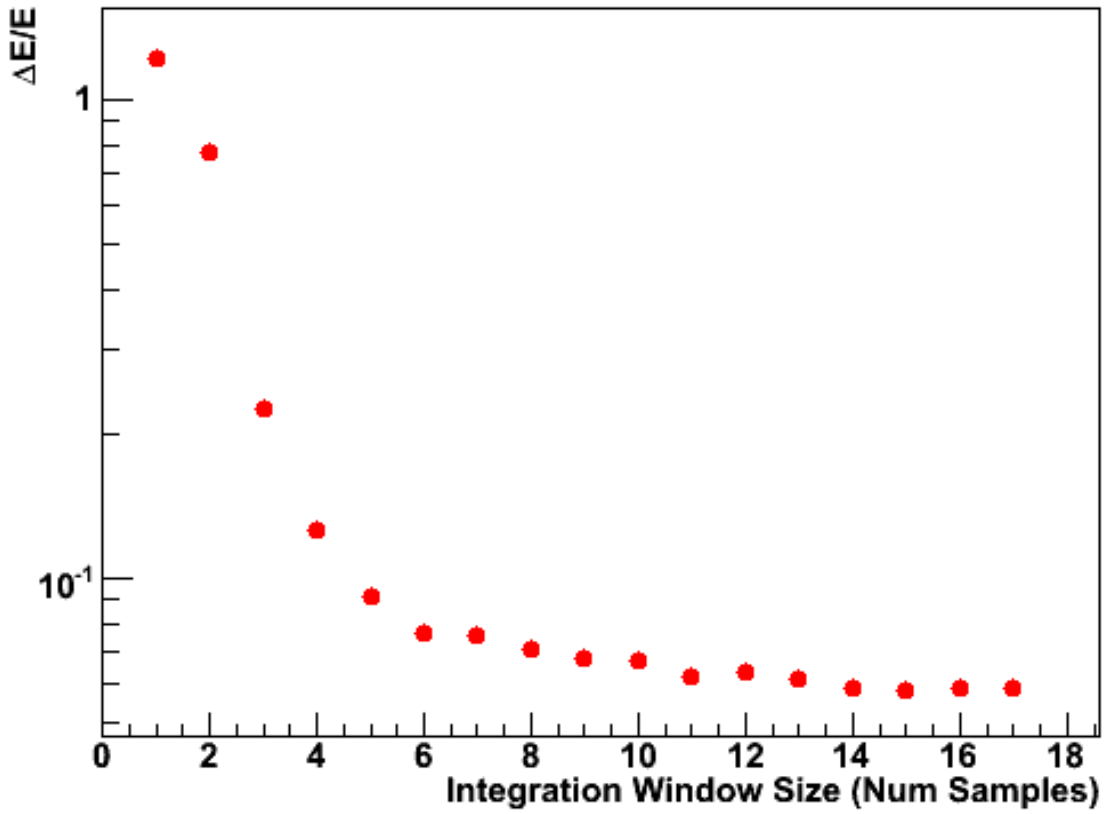

Figure C.5: Relative width of the energy (signal integral) measurements made with varying integration window size. First sample used for integration is the last one preceding the signal leading edge.

granularity on a 600 μm thick Si. Conceptually the latter design is similar to the one chosen by the central VTX group for the two external layers of the PHENIX central Si tracker so the intent was to benefit from already made studies of similar sensors.

Stripixel sensor design files were produced at BNL Instrumentation and submitted for implementation to ELMA in Russia and SENS in Korea. Test wafers from both sources were delivered to us in September 2007. Bulk testing revealed unexpectedly large strip capacitances on both products which otherwise demonstrated CV and IV characteristics normal for this kind of device. Further analysis indicated that both manufacturers probably had problems maintaining 5 μm separation gaps between implanted p+ regions resulting in ohmic contact between implanted strips.

To make a meaningful comparative study of the two kinds of sensors we built a manually controlled moving stage carrying the readout electronics with bonded sensors exposed to electrons from collimated Sr^{90} source (Fig. C.6).

Two PMT's coupled to 1 mm thick scintillator installed downstream of the sensor are

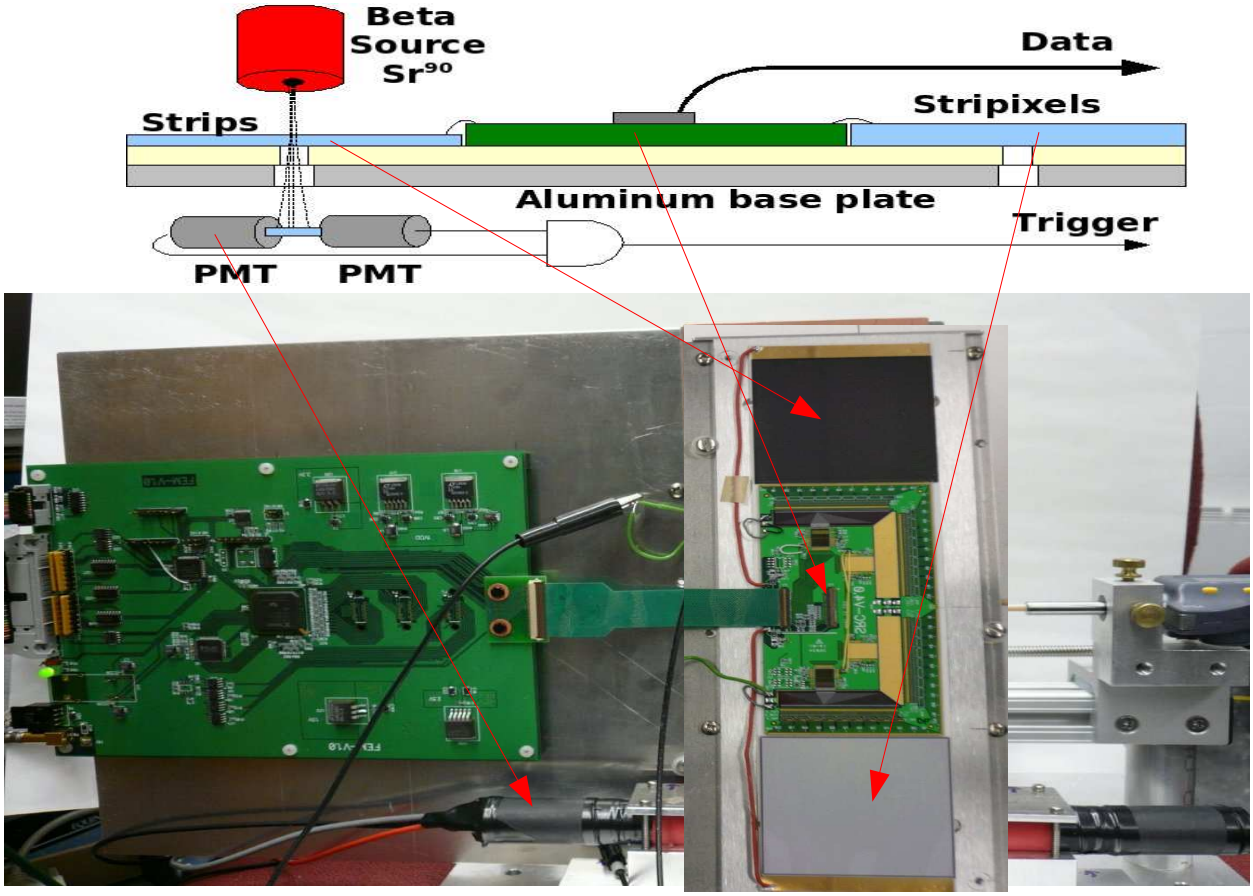

Figure C.6: Block diagram and photograph of the test stand built to study strip/stripixel sensor response to electrons from Sr^{90} radioactive source.

used to trigger on electrons. The sensor readout card (SRC) has bonding pads along three of the edges. Two different prototype Si sensors (strip and stripixel) and SRC are glued to the common substrate and bonded along two opposite edges. Bonding pads were connected to the input pads of SVX4 readout chips through Si pitch adapters. The timing and sequencing of SVX4's is provided by a FPGA based program, downloaded to the large FPGA (XSC2V1000: 10^6 gates, 110 KBytes of RAM) chip visible in the center of the readout FEM in the left part of the picture. The firmware for the FEM was developed in our lab at BNL. A small ColdWire interface processor is used to download the FPGA code to FEM and the serial data to SVX4's, as well as to perform control functions. The same ColdWire interface processor was used to record data to disk. To minimize signal distortions due to random nature of trigger signals only those events within 16 ns from a "RHIC clock" internally simulated by FPGA code are accepted. Similar logic is used to calibrate the system response with test charge injection into few or all SVX4 inputs.

The readout was calibrated by injecting a test charge of 20 fC into every 8^{th} channel in SVX4's. A typical signal pattern seen in the output data from both chips is shown in Fig. C.7. Two top and two bottom panels correspond to two different SVX4 chips bonded to stripixel

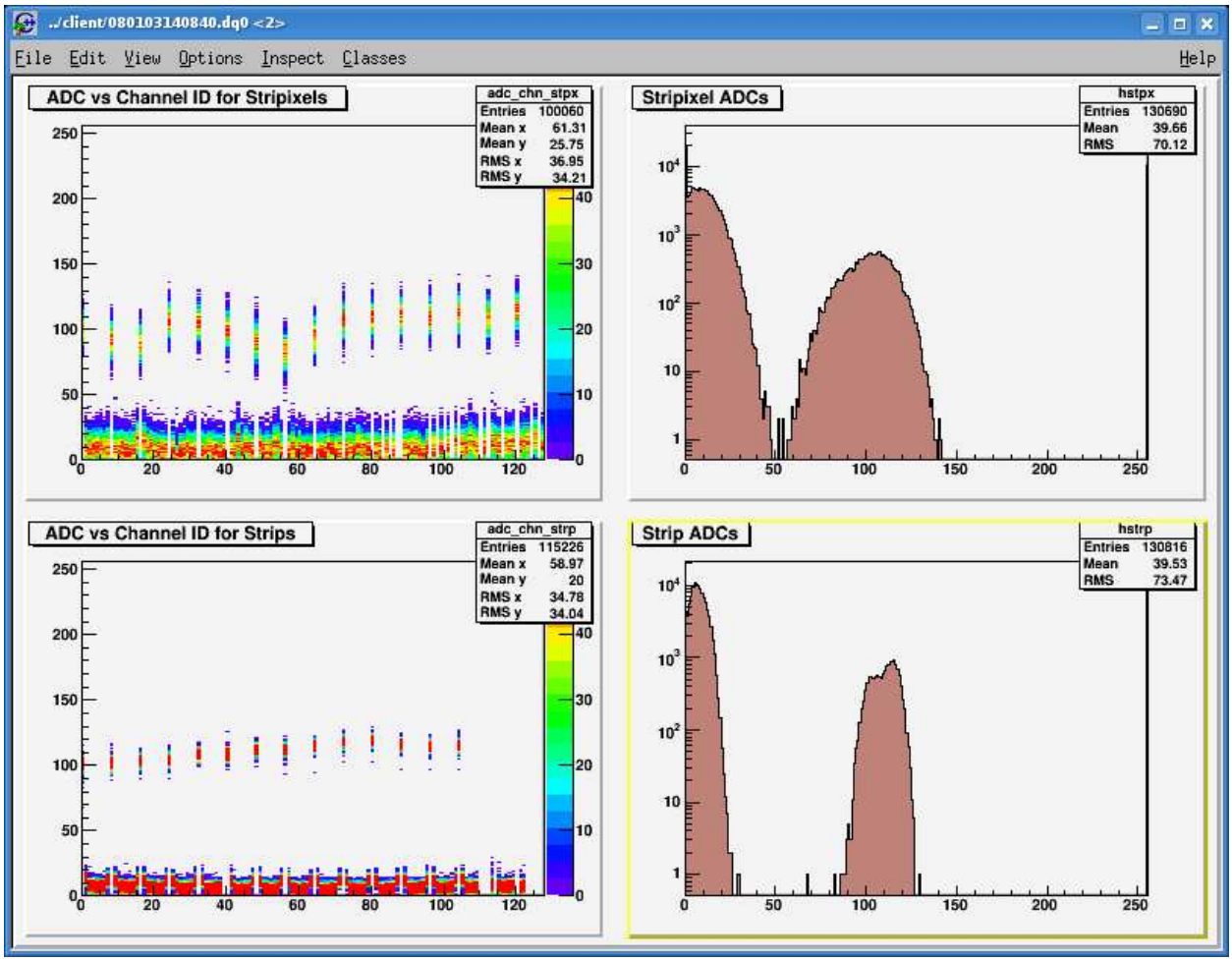

Figure C.7: Calibration run, both sensors are biased to 70V. The ADC gain for stripixel sensor is set to maximum, for strip sensor it is x2 lower. The calibration charge of 20fC injected in every 8^{th} channel of each sensor. Note the pedestal shift for strip channels adjacent to the hit channels – this is an effect of capacitive crosstalk between hit channel and its immediate neighbors. There is no such effect on stripixels, the capacitive crosstalk affects uniformly all neighbors.

(top) and strip (bottom) sensors. Gains of both SVX4's were adjusted to get the test pulse signal at approximately the same position (100 ADC counts). Dramatic differences in the pedestal widths (peak around zero) and test pulse widths as measured by two identical SVX4 chips are indicative of a problem we still face in our effort to complete R&D program aimed to develop new 2D-position sensitive Si sensor. A probable explanation is the possibility of shorts between implanted regions responsible for X and Y measurements leading to sensor being seen by readout as a single large capacitance photo-diode with noise driven by that capacitance. The strip sensor which is of a classic design of a similar granularity shows no problem in calibration.

Both sensors were further exposed to electrons from Sr^{90} decays. Amplitudes due to

electrons crossing the sensor (sum of the two adjacent strips) are shown in the Fig. C.8. Inefficiencies in the trigger result in the pedestal peak still present (dotted line shows pedestal peak measured in the absence of a signal), and the MIP peak is clearly well separated (by approximately 3 standard deviations).

Further work to improve the system resolution is certainly warranted but the main conclusion is obvious: we have successfully completed an R&D program aimed at developing and prototyping a full readout chain for position sensitive layers in NCC. We have also proven that our declared backup solution based upon conventional strip sensors is ready for the final implementation.

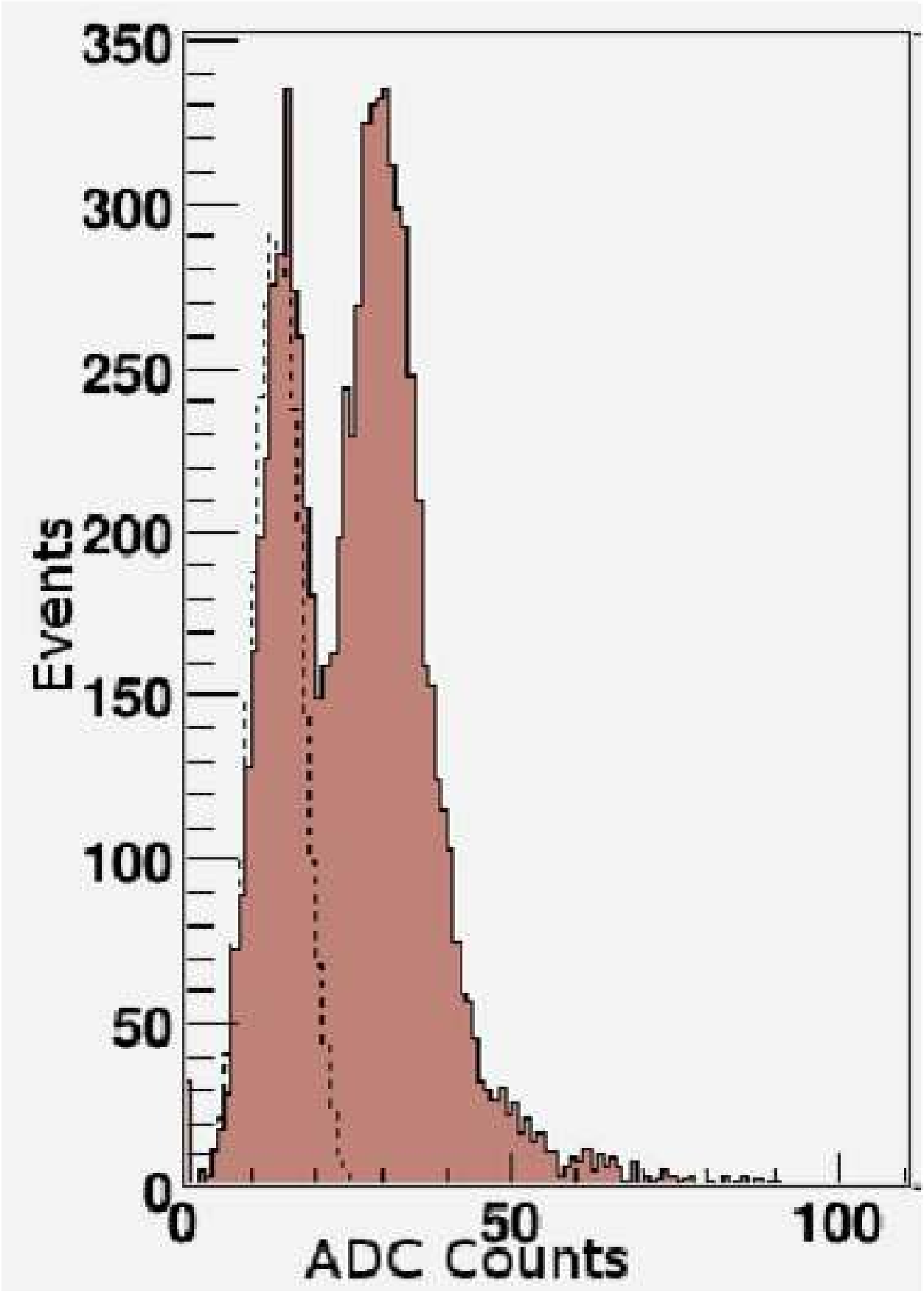

Figure C.8: Sum of amplitudes from two adjacent strips for events with selected trigger clock phases (2,3 and 4). The dashed line – from the pedestal run. The MIP peak is clearly seen.

List of Figures

List of Tables